Czech Technical University in Prague
Faculty of Transportation Sciences
Department of Security Technologies and Engineering

*Ing. Karina Šimonová*

# Miniaturized Acoustic Sensors for Monitoring Transportation Noise: Modelling, Measurement and Applications

PhD Thesis

Branch of study: Engineering Informatics
Specialization: Engineering Informatics of Transportation and Communication

Prague, August 2023

# Abstract

Wireless sensor networks have become popular in the domain of environmental noise monitoring in recent years. However, low-cost and high quality microphones are needed when there are numerous sensor nodes. Theoretical models of miniaturized low-cost electroacoustic transducers and experimental verification of their performance in noise sensors is, therefore, of interest.

This thesis deals with analytical and semi-analytical approaches describing the behaviour of the square clamped plate. The plate is used as a moving electrode of a miniaturized condenser microphone coupled with an acoustic pressure field inside a thin layer of thermo-viscous fluid trapped between the square plate and the backing electrode of the electrostatic transducer. The analytically calculated pressure sensitivity of the receiver is compared to the numerically (FEM) calculated value. The classical simple lumped-element model of an electret microphone, which is used in a previous version of the sensor network developed by the Laboratory of Special Projects UBTI FD CTU in Prague, is also described. Several experimental results measured on both prototype versions of the sensor, previous and recent, are presented including, the normalized transfer function of the electroacoustic path and the dynamic range of the present sensor, along with the temperature dependence of the new sensor.

**Keywords:**
Acoustics, MEMS transducer, analytical approach, numerical implementation.

# Acknowledgement

This thesis would not have been possible without support and encouragement of my colleagues, friends and family. I would like to express my sincerest thanks to all of these people for their friendship, support and love throughout all these years.

Foremost, I would like to express my sincere gratitude to my supervisors, doc. Ing. Václav Jirovský, CSc. and Ing. Petr Honzík, Ph.D. for their support, enthusiasm and enlightening guidance. Their profound knowledge has been a constant source of information for my research. Their patient and dedicated mentoring has been extraordinary and indispensable to the completion of this thesis.

I also want to extend my thanks to Mr. Stéphane Durand, and Mr. Nicolas Joly for their advice and support during my Ph.D. internship and studies. The collaboration with them has always been inspiring and delightful. I thank my co-authors prof. M. Bruneau and prof. P. Gatignol. It was a pleasure working with them.

I would like to express my gratitude to the whole Laboratory of Special Projects UBTI FD CTU in Prague that have welcomed me and doc. Ing. Václav Jirovský, CSc. in particular for giving me the opportunity to join the team.

Moreover, I would like to thank Ms. Elena Vjacheslavovna Abramova and Mr. Vladimir Borisovich Abramov, whose support and consistent encouragement kept me motivated and concentrated on my research throughout these years.

Ráda bych poděkovala Ing. Renátě Šimonové a Ing. arch. Hynkovi Šimonovi za přijetí do rodiny, za celkovou laskavost, trpělivost a bezmeznou podporu.

A big thank you to my friends Ing. Šárka Marešová and Ing. Michal Kluc. It is great to have a Master's buddies and to share how our life evolves since then.

Last but not the least, I would like to express my deepest gratitude to Ing. Jan Šimon to whom this thesis is dedicated, for his love and unwavering support during the best and worst of my times. Without his encouragement and full support, this Ph.D. would not have been possible.

# Čestné prohlášení

Prohlašuji, že jsem předloženou práci vypracovala samostatně a že jsem uvedla veškeré použité informační zdroje v souladu s Metodickým pokynem o etické přípravě vysokoškolských závěrečných prací.

Praha, Srpen, 2023

# Contents

# List of Figures

# List of Tables

# List of Common Abbreviations

### Abbreviations

| | |
|---|---|
| **FEM** | Finite Element Method |
| **HP** | High Pass |
| **LP** | Low Pass |
| **MEMS** | Micro-Electro-Mechanical Systems |
| **PIC** | Programmable Interface Controllers |
| **RMS** | Root Mean Square |
| **SPL** | Sound Pressure Level |
| **SPI** | Serial Peripheral Interface |
| **TDH** | Total Harmonic Distortion |

# Chapter 1

# Introduction

## 1.1 Motivation

Noise is major public health issue. It has negative impacts on human health and well-being, and is a growing concern. According to Environmental Noise Guidelines for the European Region (2018), the negative impact of acoustic pollution has been increasing significantly, especially in inhabited areas, and transport noise is now ranked among the most intensive sources of acoustic pollution.

As stated by the Environmental Noise Directive, it is necessary to monitor, understand and reduce the negative impact of acoustic pollution. To achieve this, a process of long-term acoustic measurements and analysis is required. The traditional method of environmental acoustic monitoring (noise mapping) utilizes short term measurement periods using expensive equipment and an expensive setup.

As new methods and approaches to noise monitoring evolved, sensor networks for continuous noise assessment became a trend. It is evident that long-term automated monitoring significantly improves the precision of the measurement results. In fact, a sensor network that densely covers a selected area provides location-specific data that can be used to create and verify propagation models of noise pollution for use in planning and in implementing traffic engineering solutions. Several developments and architectures for the application of acoustic sensor networks have been reported in the literature [1, 2, 3]. The networks vary from the application of expensive dedicated hardware to low-cost sensor nodes and even sensor networks based on smartphones. One category of such networks in particular offers custom-built sensor network solutions designed to be low-cost, low-power and autonomous, and therefore suitable for wide-ranging deployment. The potential of a network with low-cost hardware has been demonstrated in the Trafficsensnet project developed at the Department of Security Technologies and Engineering of the Czech Technical University in Prague, which works on measuring levels of air pollution, including noise related to road-based transport. Other categories are briefly discussed in Chapter 2.3 ("Noise sensors and wireless sensor networks").

Within the Trafficsensnet project, 20 master sensor units and 6 slave units were developed by the laboratory of the Department of Security Technologies and Engineering and

were deployed in Prague in 2015-2017. The master unit was developed as a gateway unit for the measurements. The slave unit, in its turn, was a small, stand-alone platform with the potential to be battery-powered. The slave unit contained a noise senor consisting of a small elecret microphone, an analog A-filter and digital signal processing in a tiny microcontroller.

A recent version of this noise sensor is based on the MEMS microphone with digital signal processing. Since these types of low-cost microphones are dedicated to the speech frequency range, a detailed experimental verification of the noise sensor along with the theoretical models of miniaturized low-cost transducers are needed.

This thesis presents a study of new types of electroacoustic transducers. Sensor prototypes designed and implemented for specific requirements are verified experimentally. Further miniaturization and greater precision of acoustic sensors are also investigated.

## 1.2 Structure of the thesis

The Introduction surveys the context of long-term acoustic measurements and analyses, addressing the growing interest in new methods and in custom built noise monitoring solutions.

Chapter 2 ("Current practices and developments in noise monitoring technology") sets the starting points for further analysis in modelling miniaturized devices and related acoustic measurements, raises some common methodological issues encountered by researchers, and introduces some of the challenges that will be faced.

Chapter 3 ("A theoretical investigation into the behaviour of miniaturized transducers") is divided into two main subsections. This chapter introduces transducers with a non-perforated plate and also with a perforated plate.

The first subsection ("A non perforated plate as a moving electrode of the MEMS transducer") is followed by a discussion about the displacement field of a non-perforated rectangular clamped plate, presents three different methods for finding the approximate form of the moving electrode eigenfunctions: first, through the use of a double cosine series; second, through the use of 1D beam eigenfunctions; and third, through the use of a linear approximation of the numerical solution together with an exact analytical form of the eigenfunction based on modal wave function of 1D beam normalized eigenfunctions as a solution to circumvent the difficulties encountered when previous methods are used.

The second subsection ("A perforated plate as a moving electrode of the MEMS transducer") investigates plates with perforation and introduces the complexity of the coupling effect between the perforated plate displacement and the acoustic pressure in the thin fluid layer, with refer to fundamental physical concepts.

Chapter 4 ("Measurements on the noise sensor prototypes, and an analysis") is dedicated to separated, consecutive measurements on two versions of a noise sensor developed at the Laboratory of Special Projects UBTI FD CTU in Prague. This chapter investigates detailed experimental case studies of a low-cost electret microphone, including an experimental estimate of some parameters of the equivalent circuit of an electret microphone that

cannot be measured directly. There are some measurements on the MEMS microphone A-filter system, and on MEMS itself. A raw data provided by the present version of the noise monitoring sensor giving an idea of the ability of the microphone to provide useful technical information.

The section on conclusions provides a summary of the central ideas, findings and aspects of the thesis, along with some suggestions for solving the problem of modelling more complex shapes than square membranes or plates. Finally, in the section on Perspectives suggestions are made for further research.

# Chapter 2

# Current practices and developments in noise monitoring technology

## 2.1 Noise control legislation

Chaotic disturbances of signals, classified as noise [4], pose a fundamental problem for information processing and affect all aspects of the function of the nervous system [5, 6]. The relationship between environmental noise and public health is perhaps the most significant reason why environmental noise has emerged as a major issue in environmental legislation and policy in recent years. Much research including The World Health Organization (WHO) investigation has emerged over the last two decades linking environmental noise with detrimental health impacts such as disturbed sleep, impaired work performance, impedes the learning process, hinders social activity and verbal communication, and many other issues.

Noise mapping is becoming a necessary tool for evaluating the noise exposure of citizens in inhabited areas, as reported in the European Directive 2002/49/EC and the 2018 WHO Environmental noise guidelines. Until recently, mean vehicle flows, averaged over a period of one year [4] were the input parameters required for noise mapping. Yet this simple approach can determine significant uncertainty when dealing with varying noise on a daily basis, and the trouble of manual operation becomes a difficulty, when it comes to the demand for long-term measurements. As a result noise maps had been evolving towards a promising direction of network predictive approach.

The Guidelines on Directive have had a direct and immediate impact on policy-making in a member states including Czech Republic and have prompted the adaptation of local and national strategic noise maps and new noise action plans aimed at mitigating environmental noise, as well to take a harmonized approach when estimating the health effects from environmental noise [7].

The overall problem is being tackled to a limited extent both by legislative measures and traffic engineering (road construction and building technology) as traffic noise emissions can and should be reduced at a source, by establishing limits for the noise of vehicle engines

or speed limits, promotion of quieter tyres and development of low-noise road surfaces.

As a consequence the support from automobile manufacturers and traffic engineering experts is also needed to maximise the potential of quiet vehicles in everyday road traffic, and to make the progress in traffic noise reduction. The European Automobile Manufacturers' Association (ACEA), the European Tyre and Rubber Manufacturers' Association (ETRMA) and the European Tyre and Rim Technical Organisation (ETRTO) join forces to make several key recommendations on noise reduction and environmental noise in [8].

Current vehicle noise legislation reflects both aspects: noise nuisance (single incidents) and noise pollution (latent noise exposure). Vehicles are measured for type approval in a way that the determined sound level is representative of the use of the vehicle in urban driving conditions. A particular sound emission of the vehicles should be taken into consideration by the noise legislation, which not only prescribes maximum levels for environmental protection, but (in the EU since July 2021) minimum levels for safety reasons in order to ensure that vehicles, like electric cars for example, can be adequately detected when in motion [8].

Road traffic noise is caused by a combination of elements: rolling noise (interactions between the tyre and road surface) and propulsion noise (originating from the engine and drive train). For road traffic noise, the type of road surface plays a major role. A low tyre-rolling sound can only be achieved when all technologies to minimise noise are applied to the road surface in the same manner as for tyre technologies.

While the acoustic properties of tyres are the subject of European regulation, low-noise road surfaces are the responsibility of local and national road administrations.

## 2.2 Technical issues

The key requirements specified in the standards are measurement methods and instrumentation. The measurements of traffic noise in Europe governs by the European Environmental Noise Directive is based on the ISO 9613-2 standard. While the most widely-used instruments used for measuring noise are sound level meters. They have an A-weighting filter to simulate the subjective response of the human ear. Upon comparison of different sound level meters, it can be observed that the devices have varying measurement ranges and accuracy rates, with some devices capable of measuring a broader range of noise levels than others. However despite of that, each of them need to meet a variety of performance requirements, such as frequency response, sensitivity, and dynamic range. IEC 61672-1:2013 is the current international standard that specifies the sound level meter functionality, performance and calibration criteria that instruments must meet in order to be considered fit for purpose.

## 2.3 Noise sensors and wireless sensor networks

Sensor networks for environmental noise monitoring can be divided into four categories, based on: hardware costs, scalability, flexibility, reliability, and accuracy, which all together determine the range of applications for which a network is suited [1].

Category 1 monitoring equipment uses high-end sensors and custom hardware components. Category 2 balances between expensive dedicated monitoring hardware and cheap sensors for general use. Category 3 is for networks based on the usage of smartphones. Category 4 is for low-cost acoustic sensor networks such as Trafficsensnet. These systems are generally based on low cost microphones and the signal processing chain required by the norms (Fig. 2.1), and they can be implemented on a single board computer [2]. Modelling on an acceptable level of approximation of such devices is of vital importance in developing innovative products and in reducing time-to-market at lower overall cost [1].

Further information about the implementation of such wireless sensor networks can be found in [2] and [3].

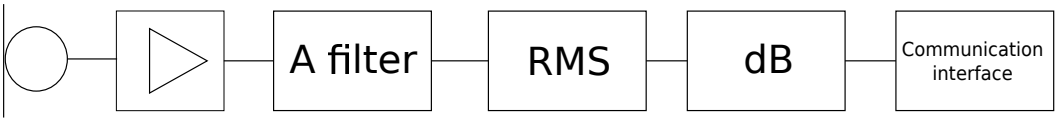


Figure 2.1: General block diagram of a noise sensor.

### 2.3.1 Miniaturized microphones

Many realizations of miniaturized electroacoustic transducers based on various transduction principles (condenser, piezoelectric and piezoresistive) are used as acoustic receivers. The first mention of a silicon condenser microphone, which became the post-electret generation of microphones, is summarized in [9], which provides a detailed review of such microphones. Since the mid 1990s, there have been numerous developments in design and fabrication methods [10] and [11] have summarized the academic research on micromachines in the past 30 years. An outstanding more recent paper, [12], covers various types of backplate configurations with the moving electrode surrounded by perforated back plates on both sides.

## 2.4 Modelling miniaturized devices

### 2.4.1 Introduction to the modelling of miniaturized devices

MEMS devices and transducers have been growing in use as the technology of fabrication becomes more sophisticated. Modelling these miniature elements helps developers to understand the devices and to optimize them by designing devices that are smaller, more sophisticated and cheaper to manufacture. There has been increasing interest in designing

miniaturized vibrating devices using MEMS processes, and in using them for consumer audio devices and also in the field of measurement applications such as noise monitoring using wireless sensor networks [3].

In recent years, extensive research and development work has been carried out on MEMS, and a large number of techniques (series methods, approximate analytical techniques, finite difference techniques, the Galerkin technique, the Rayleigh-Ritz method) have appeared in the literature to tackle this complicated modelling problem. Each development solution has its own advantages and limitations. The experimental studies include approximate theoretical models ([13], e.g., using the "porosity" approach and [14], which deals with the acoustic short circuit through the opening hole), and is mainly based on the lumped elements approach. More recent and more advanced approaches can be found in [15, 16]. These model are fully analytical and achieve high-precision results for sensitivity. Several other fully analytical models [17, 18, 19, 20, 21] have been developed aimed at meeting the requirements on the edge conditions that relate to both the solution for the displacement field of the diaphragm and its first spatial derivative (clamped plate). These studies are dedicated analytic investigations that enable a description of the strong coupling between a diaphragm and a thin fluid layer. MEMS can primarily be modelled in one of two ways, by, analytical modelling or by numerical modelling. Analytical modelling makes use of one or more theories to achieve results. The scientific examination presented in [22]is an example in which a model is developed that relies on the modal expansion for the displacement field (Dirichlet eigenmodes). These models are efficient for comparatively simple designs, and they address two particular problems: reasoning out analytically the modal behavior of the loaded clamped plate, and choosing an appropriate analytical approach for the acoustic field in the fluid gap. These models are therefore convenient for describing the coupling of the acoustic pressure in the thin fluid layer with the displacement field of the plate.

An unfortunate limitation in this way of expressing the acoustic field in the fluid gap is that there is not only a marked shortcoming in terms of coupling with the modal expansion of the displacement field of the diaphragm. It is also also not obvious how to match this expression with the boundary condition at the entrance of the reservoir, especially when dealing with the high frequency range.

Most of the attempts therefore rely on numerical [34] techniques rather than analytical techniques, due to the potential of numerical methods to model structures with complex geometrical shapes. Despite the advantages of numerical techniques researchers have been faced with a number of difficulties when trying to use commercial simulation packages and to adapt traditional numerical methods. The difficulties and challenges that face MEMS modelling and simulation experts are due to the very nature of MEMS and are related to the physical principle of operation, the geometrical structure, miniaturization, packaging, manufacturing and processing of MEMS. Environmental conditions also have to be taken into account. Moreover, numerical modelling requires a high-end computer to perform simulations on, and even then the modelling can be extremely time consuming.

### 2.4.2 Electrostatic transduction principles

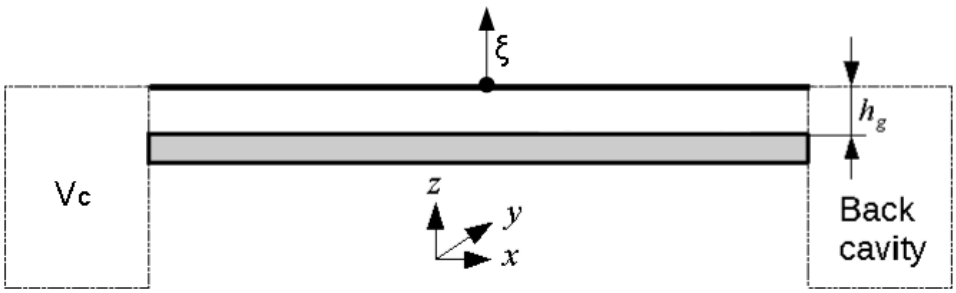


Figure 2.2: Simplified electrostatic transducer scheme.

Most miniaturized acoustic pressure sensors (MEMS microphones) use the electrostatic principle of transduction [23] (condenser microphones were first presented in [24]), though some of them are piezoelectric [25]. The electrostatic type of microphone (condenser microphone) is essentially a parallel-plate capacitor. A capacitor consists of a movable front plate (the capsule diaphragm/membrane) and a stationary backplate (Fig. 2.2). The operation of the capacitor depends on the interaction between its electric field and the change in its electrostatic capacitance when exposed to the pressure of a sound wave. The electrostatic principle behind the transducer is as follows: the charge in a capacitor can be expressed as $Q = CU$, where the total static capacitance $C$ is the sum of the active static capacitance and the parasitic capacitance. The total differential of the charge can then be expressed as $dQ = dCU + CdU$, where $U$ is the total voltage at the output of the condenser microphone consisting of the static component, the polarization voltage $U_0$, and the varying component $u$ caused by the change in the capacitance $dC$. Assuming the effect of the polarization resistor of huge value and assuming $dU \approx u$ along $U \approx U_0$, we get the output voltage of the microphone directly in the form [26]

$$u = U_0 \frac{dC}{C}, \tag{2.1}$$

where the total time-dependent capacitance is given by

$$C_t(t) = C_r + \frac{\varepsilon_0 S}{\bar{\xi}(t) + h_g} = C_r + C_0 \frac{1}{1 + \frac{\bar{\xi}(t)}{h_g}}, \tag{2.2}$$

with $\bar{\xi}(t) = \iint_{S_e} \xi(x, y, t) \mathrm{d}S_e$ being the mean value of the displacement $\xi(x, y, t)$ of the moving electrode over the surface of the fixed electrode $S_e$, $C_0$ is the static capacitance

of the transducer at rest and $C_r$ is the parasitic capacitance. Using the Taylor series $\frac{1}{1+x} = 1 - x + x^2 - x^3 + x^4 ...$ and assuming that $C_t(t) = C_r + C_0 + dC(t)$ we get

$$dC(t) = -C_0 \left[ \frac{\bar{\xi}(t)}{h_g} - \left( \frac{\bar{\xi}(t)}{h_g} \right)^2 + \left( \frac{\bar{\xi}(t)}{h_g} \right)^3 - ... \right]. \tag{2.3}$$

Substituting (2.3) into (2.1), the time-dependent output voltage of the condenser microphone is then given by

$$u(t) = U_0 \frac{C_0}{C_r + C_0} \left[ \frac{\bar{\xi}(t)}{h_g} - \left( \frac{\bar{\xi}(t)}{h_g} \right)^2 + \left( \frac{\bar{\xi}(t)}{h_g} \right)^3 - ... \right]. \tag{2.4}$$

In the case of a linear model of the microphone and negligible parasitic capacitance, this output voltage becomes

$$u(t) = U_0 \frac{\bar{\xi}(t)}{h_g}. \tag{2.5}$$

The acoustic pressure sensitivity of the transducer, calculated as the ratio of the output voltage $u$ and the incident acoustic pressure $p_{inc}$, can be expressed as follows

$$\sigma = \frac{u}{p_{inc}} = U_0 \frac{\bar{\xi}(t)}{p_{inc} h_g}. \tag{2.6}$$

This shows the importance of a precise model giving the displacement of the moving electrode. This displacement is strongly influenced by the acoustic field in the system behind the moving electrode. Therefore, any model has to take into account the acoustic behaviour of the system, including the thermoviscous losses originating in the narrow regions in the system (air gap, holes, etc.).

### 2.4.3 General governing equations

The acoustic field propagation in the gap can be described [27, 28, 29] using the Navier-Stokes equation

$$\frac{1}{c_0} \frac{\partial v}{\partial t} + \frac{1}{\rho_0 c_0} \overrightarrow{\text{grad}}\, p = l_v \overrightarrow{\text{grad}}\, \text{div}\, \vec{v} - l'_v \overrightarrow{\text{rot}}\, \overrightarrow{\text{rot}}\, \vec{v}, \tag{2.7}$$

the law of the conservation of mass

$$\rho_0 c_0\, \text{div}\, v + \frac{\gamma}{c_0} \frac{\partial}{\partial t} (p - \beta\tau) = 0, \tag{2.8}$$

and the Fourier equation for heat conduction

$$\left( \frac{1}{c_0} \frac{\partial}{\partial t} - l_h \Delta \right) \tau = \frac{\gamma - 1}{\beta\gamma} \frac{1}{c_0} \frac{\partial}{\partial t} p, \tag{2.9}$$

where the viscous characteristic lengths are $l'_v = \frac{\mu}{\rho_0 c_0}$, $l_v = \frac{1}{\rho_0 c_0}(\frac{4}{3}\mu + \nu)$ and the thermal characteristic length is $l_h = \frac{\lambda_h}{\rho_0 c_0 C_p}$, the properties of the fluid being the density $\rho_0$, the adiabatic speed of sound $c_0$, the specific heat ratio $\gamma$, the shear viscosity coefficient $\mu$, the bulk viscosity $\nu$, the thermal conductivity coefficient $\lambda_h$, the heat capacity at constant pressure per unit of mass $C_p$, and the increase in pressure per unit increase in temperature at constant density $\beta$.

Assuming that $w$ designates one of the inplane coordinates $x$ or $y$ (or radial coordinate $r$ for circular geometries), and taking into account the simplifications $v_w \gg v_z$, $\partial_z v_w \gg \partial_w v_w$, $\partial_z \tau \gg \partial_w \tau$, $p(w,z) \cong p(w)$ valid for the thin fluid layer in the gap, eq. (2.7) to (2.9) becomes

$$\left(\frac{1}{c_0}\frac{\partial}{\partial t} - l_v\frac{\partial^2}{\partial z^2}\right) v_w(w,z) = -\frac{1}{\rho_0 c_0}\frac{\partial}{\partial w}p\left(w\right), \tag{2.10}$$

$$\left(\frac{1}{c_0}\frac{\partial}{\partial t} - l_h\frac{\partial^2}{\partial z^2}\right) \tau(w,z) = \frac{\gamma-1}{\beta\gamma c_0}\frac{\partial p\left(w\right)}{\partial t}, \tag{2.11}$$

Since the time dependence is assumed to be $e^{j\omega t}$, $\omega$ being the angular frequency, (2.10) and (2.11) can be rewritten in the frequency domain

$$\left(\frac{\partial^2}{\partial z^2} + k_v^2\right) v_w(w,z) = \frac{1}{\mu}\frac{\partial p\left(w\right)}{\partial w}, \tag{2.12}$$

$$\left(\frac{\partial^2}{\partial z^2} + k_h^2\right) \tau(w,z) = \frac{\gamma-1}{\beta\gamma}k_h^2 p\left(w\right), \tag{2.13}$$

where

$$k_v = \frac{1-j}{\sqrt{2}}\sqrt{\frac{\rho_0\omega}{\mu}}, \tag{2.14}$$

$$k_h = \frac{1-j}{\sqrt{2}}\sqrt{\frac{\rho_0\omega C_p}{\lambda_h}}, \tag{2.15}$$

are the wave numbers respectively associated with the vertical movement due to viscosity effects and with the entropic movement due to heat conductivity effects.

To solve the equations (2.12) and (2.13) above, we need to specify boundary conditions for the particle velocity and the temperature variation on the backplate ($z = 0$) and on the moving electrode ($z = h_g$)

$$v_w\left(w, z=0\right) = v_w\left(w, z=h_g\right) = 0, \tag{2.16}$$

$$\tau\left(w, z=0\right) = v_w\left(w, z=h_g\right) = 0. \tag{2.17}$$

The solutions of the equations (2.12), (2.13) are thus given respectively by

$$v_w\left(w,z\right)=-\frac{1}{j\omega\rho_0}\frac{\partial p\left(w\right)}{\partial w}\left[\frac{\cos\left(k_v h_g\right)-1}{\sin\left(k_v h_g\right)}\sin(k_v z)-\cos\left(k_v z\right)+1\right], \tag{2.18}$$

$$\tau\left(w,z\right)=\frac{\gamma-1}{\gamma\beta}p\left(w\right)\left[\frac{\cos\left(k_h h_g\right)-1}{\sin\left(k_h h_g\right)}\sin(k_h z)-\cos\left(k_h z\right)+1\right]. \tag{2.19}$$

The mean values of the particle velocity and the temperature variation across the thickness of the gap take the form of

$$<v_w\left(w,z\right)>_z=-\frac{1}{j\omega\rho_0}\frac{\partial p(w)}{\partial w}F_{vg}, \tag{2.20}$$

where

$$F_{vg}=\frac{1}{h_g}\int_0^{h_g}\left[\frac{\cos\left(k_v h_g\right)-1}{\sin\left(k_v h_g\right)}\sin(k_v z)-\cos\left(k_v z\right)+1\right]\mathrm{d}z=1-\frac{\tan\left(k_v h_g/2\right)}{k_v h_g/2}, \tag{2.21}$$

and

$$<\tau_w\left(w,z\right)>_z=\frac{\gamma-1}{\beta\gamma}p(w)F_{hg}, \tag{2.22}$$

where

$$F_{hg}=\frac{1}{h_g}\int_0^{h_g}\left[\frac{\cos\left(k_h h_g\right)-1}{\sin\left(k_h h_g\right)}\sin(k_h z)-\cos\left(k_h z\right)+1\right]\mathrm{d}z=1-\frac{\tan\left(k_h h_g/2\right)}{k_h h_g/2}. \tag{2.23}$$

For rectangular geometries, the law of conservation of mass (in Cartesian coordinates $x, y$), taking into account the velocity of the moving electrode $v_m(x,y)=j\omega\xi(x,y)$, $\xi(x,y)$ being the displacement field of the moving electrode (positive when outwardly directed), can be expressed as follows

$$-\rho_0\frac{\partial v_x}{\partial x}h_g\,dx\,dy-\rho_0\frac{\partial v_y}{\partial y}h_g\,dx\,dy-\rho_0 v_m\left(x,y\right)\,dx\,dy=\frac{\partial\rho_a}{\partial t}h_g\,dx\,dy, \tag{2.24}$$

where the acoustic density variation $\rho_a=(p-\beta\tau)\gamma/c_0^2$ becomes, after applying (2.22),

$$\rho_a=\frac{p_g\left(x,y\right)}{c_0^2}\left[\gamma-\left(\gamma-1\right)F_{hg}\right]. \tag{2.25}$$

Substituting (2.20) and (2.25) into (2.24) gives the wave equation for the acoustic pressure in the air gap $p_g(x,y)$

$$\left(\partial_{xx}^2+\partial_{yy}^2+\chi^2\right)p_g\left(x,y\right)=-U\left(x,y\right), \tag{2.26}$$

where $\partial_{xx}^2$ and $\partial_{yy}^2$ are second spatial derivatives,

$$\chi^2=\frac{\omega^2}{c_0^2}\left[\frac{1+\left(\gamma-1\right)\left(1-F_{hg}\right)}{F_{vg}}\right], \tag{2.27}$$

is the complex wavenumber and

$$U\left(x,y\right)=\frac{\rho_0\omega^2}{h_gF_{vg}}\xi(x,y), \tag{2.28}$$

is the source term.

The behaviour of the moving electrode, here the thin membrane, is described by the wave equation for its displacement field

$$T\left(\frac{\partial^2}{\partial x^2}+\frac{\partial^2}{\partial y^2}+k^2\right)\xi\left(x,y\right)=p_{inc}-p_g\left(x,y\right), \tag{2.29}$$

where $k=\omega\sqrt{m_s/T}$ is the membrane wavenumber, $T$ is the tension of the membrane, $m_s=h_m\rho_m$ is the membrane mass per unit area, $h_m$, $\rho_m$ are the membrane thickness and density, respectively. The Dirichlet boundary condition is applied at the periphery of the square membranes

$$\begin{aligned}\xi(a,y)=\xi(-a,y)=0,\\ \xi(x,a)=\xi(x,-a)=0,\end{aligned} \tag{2.30}$$

where $2a$ is the dimension of the side of the membrane. The general solution of 2.29 can be written as an expansion over the orthonormal eigenfunctions $\psi_{mn}(x,y)$

$$\xi\left(x,y\right)=\sum_{mn}\xi_{mn}\psi_{mn}\left(x,y\right). \tag{2.31}$$

These eigenfunctions are the solution of the homogeneous equation associated with (2.29)

$$\left(\partial_{xx}^2+\partial_{yy}^2+k_{mn}^2\right)\psi_{mn}(x,y)=0 \tag{2.32}$$

and are given in the case of the square membrane by

$$\psi_{mn}\left(x,y\right)=\frac{1}{a}\cos\left(k_{xm}x\right)\cos\left(k_{yn}y\right), \tag{2.33}$$

where the eigennumbers are given by $k_{xm}=\frac{m\pi}{2a}$, $k_{yn}=\frac{n\pi}{2a}$. Using the orthogonality property of the eigenfunctions, the modal coefficients $\xi_{mn}$ can be expressed as follows

$$\xi_{mn}=\frac{1}{T\left(k_{mn}^2-k^2\right)}\cdot\int_{-a}^{a}\int_{-a}^{a}\psi_{mn}(x,y)[p_g(x,y)-p_{inc}]\,\mathrm{d}x\mathrm{d}y, \tag{2.34}$$

where $k_{mn}^2=k_{xm}^2+k_{yn}^2$.

The wave equations (2.26) and (2.29) form a coupled system, which can be solved using multimodal methods [27, 28, 32] or using the integral formulation for the acoustic pressure in the gap, which is the main method used in this thesis.

### 2.4.4 Integral formulation for acoustic pressure

A method using the integral formulation for describing the acoustic pressure field inside the air gap of an electrostatic transducer consisting of a square membrane, a square backplate and a peripheral cavity (Fig. 2.3) has been published recently [15].

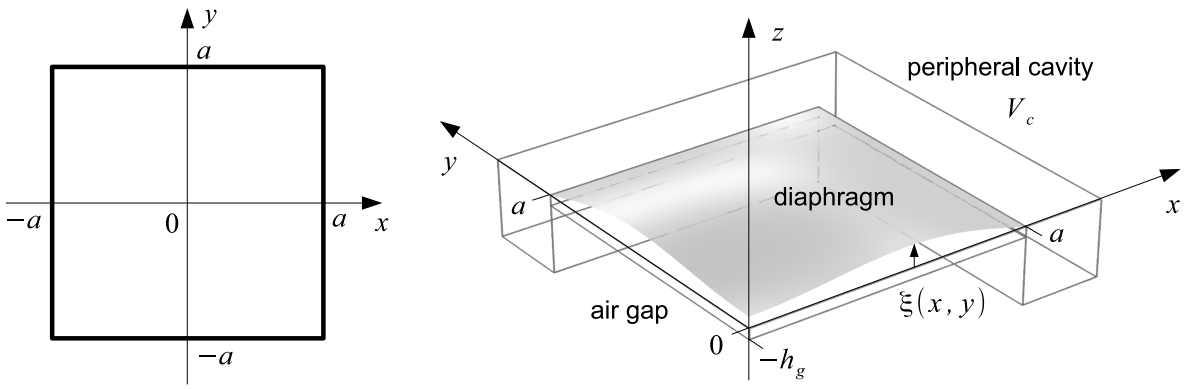


Figure 2.3: Geometry of the system: a) dimensions of the square diaphragm, and b) geometry of the transducer in the $1^{st}$ quadrant [15].

The analytical solution for the acoustic field in the fluid-gap presented in [15] can be used to avoid the procedural difficulties, namely the coupling between Dirichlet and Neumann eigenfunctions. This does not make use of modal expansion for the acoustic pressure, but uses an integral formulation with the appropriate two-dimensional Green's function, which is not expressed as the sum over the eigenfunctions.

This solution is also assumed to have the same symmetry as the diaphragm, which enables the problem to be expressed for the acoustic pressure in the first quadrant only. The acoustic field in the small reservoir is assumed to be uniform. The integral equation for the pressure variation in the fluid gap $x, y \in (0, a)$ therefore takes the following form [15]:

$$p_g(x,y) = \int_0^a \int_0^a G(x, x_0; y, y_0)\, U(x_0, y_0)\, \mathrm{d}x_0 \mathrm{d}y_0 + p_c I_G(x,y) \tag{2.35}$$

where

$$\begin{aligned} I_G(x,y) = &\int_0^a \left[\Lambda_c G(x, x_0; y, a) - \partial_{y_0} G(x, x_0; y, a)\right] \mathrm{d}x_0 \\ &+ \int_0^a \left[\Lambda_c G(x, a; y, y_0) - \partial_{x_0} G(x, a; y, y_0)\right] \mathrm{d}y_0 \end{aligned} \tag{2.36}$$

$$\text{with} \quad \Lambda_c = (-j\omega\rho_0) / (8 a h_g F_v Z_c) \tag{2.37}$$

using the relation for the first derivative at the air-gap boundary $\partial_n p_g = -j\omega\rho_0 p_c / 8 F_v Z_c h_g a$ with the input impedance of the peripheral cavity being [37]

$$Z_c = \rho_0 c_0^2 / \left(j\omega V_c\right). \tag{2.38}$$

Thanks to the symmetry mentioned above, the Green's function associated with the problem 2.26 can be taken as

$$G(x, x_0; y, y_0) = g(x, x_0; y, y_0) + g(x, -x_0; y, y_0) + g(x, x_0; y, -y_0) + g(x, -x_0; y, -y_0), \tag{2.39}$$

$$\text{with} \quad g(x, x_0; y, y_0) = \frac{-jH_0^-}{4}\left(\chi\sqrt{(x-x_0)^2 + (y-y_0)^2}\right), \tag{2.40}$$

where $H_0^-$ denotes the Hankel function of the second kind of order "0".

Note that on the boundaries in equation (2.36), the functions $p\left(x_0, a\right)$ and $p\left(a, y_0\right)$ have been replaced by their mean values $p_g$ along the $x$-axis and $y$-axis, and are given approximately by the mean value of the pressure $p_g\left(x, y\right)$ over the length of any external edge of the quadrant, namely, $p_c = \left\langle p_g \right\rangle_x = (1/a)\int_0^a p_g\left(x, a\right) \mathrm{d}x$ or equivalently $p_g = \left\langle p_g \right\rangle_y = (1/a)\int_0^a p_g\left(a, y\right) \mathrm{d}y$, calculated from eq. (2.35).

### 2.4.5 Coupling between the membrane displacement and the acoustic pressure inside the transducer

Substituting eq. (2.35) into eq. (2.34) and taking into account eq. (2.31) and eq. (2.36 - 2.38) leads to the relation for modal coefficients $\xi_{mn}$, which can be expressed in matrix form

$$\left[-\mathbb{A} + \mathbb{B}\right](\Xi) = (C), \tag{2.41}$$

where $(\Xi)$ and $(C)$ are the column vectors of elements $\xi_{mn}$ and $c_{mn} = -p_{inc}\int_{-a}^{a}\int_{-a}^{a}\psi_{mn}(x,y)\mathrm{d}x\mathrm{d}y$ respectively, $\mathbb{B}$ is a diagonal matrix of elements $T\left[k_{xm}^2 + k_{yn}^2 - k^2\right]$ and the elements of matrix $\mathbb{A}$ are given by [15]

$$\begin{aligned} A_{(mn),(qr)} =& \frac{\rho_0\omega^2}{h_g F_v}\int_{-a}^{a}\int_{-a}^{a}\Bigg[\psi_{mn}(x,y)\int_0^a\int_0^a G(x,x_0;y,y_0)\psi_{qr}(x_0,y_0)\mathrm{d}x_0\mathrm{d}y_0 \\ & - \frac{1}{1+\left\langle I_G(x,a)\right\rangle_x}\int_0^a\int_0^a \left\langle G(x,x_0;a,y_0)\right\rangle_x \psi_{qr}(x_0,y_0)\mathrm{d}x_0\mathrm{d}y_0 \\ & \left\{\left[\frac{j\omega\rho_0}{8F_v Z_c h_g a}\psi_{mn}(x,y) + \partial_y\psi_{mn}(x,y)\right]\int_0^a G(x,x_0;y,a)\mathrm{d}x_0\right. \\ & \left. + \left[\frac{j\omega\rho_0}{8F_v Z_c h_g a}\psi_{mn}(x,y) + \partial_x\psi_{mn}(x,y)\right]\int_0^a G(x,a;y,y_0)\mathrm{d}y_0\right\}\Bigg]\mathrm{d}x\mathrm{d}y. \end{aligned} \tag{2.42}$$

As a result, we have two coupled equations which relate respectively the acoustic pressure inside the fluid behind the moving electrode to the displacement field of it and, conversely, the equation which relates the displacement field of the moving electrode to the acoustic pressure behind it.

### 2.4.6 Numerical methods

Numerical analysis is branch of mathematics responsible for designing effective ways to find numerical solutions to complex mathematical problems, which sometimes cannot be solved directly. Due to the great advances in computational technology, numeracy has become very popular and is a modern tool for scientists and engineers. Numerical analysis methods (such as the Finite Element Method) (the main idea of which can be wrapped up as "replacing a given problem by an approximated problem that can be easily solved") are also used in the area of acoustic devices filled with a thermoviscous fluid, where the accurate representation of boundary layer effects requires a very large number of mesh modes. This highlights the importance of precise analytical modelling. In many theoretical works [15, 16], and also in this thesis, the numerical methods (namely FEM) are used as a reference for validating analytical methods. The design of experiments or optimization techniques can be used along with FEM to design an optimal product with specific requirements.

In this problem-solving process, we can distinguish several more or less distinct phases. The first phase is formulation. Two main FEM formulations for the acoustic field in a thermovicous fluid are used in this thesis. The first formulation is based on the calculation of the acoustic particle velocity $\vec{v}$ and temperature variation $\tau$, the acoustic pressure then being expressed from these two variables. The equations (2.7) - (2.9) are rewritten in the form of two bonded equations in the frequency domain, as follows [30]

$$\omega^2 v + B \overrightarrow{\text{grad}}\,\text{div}\,\vec{v} + C \overrightarrow{\text{rot}}\,\overrightarrow{\text{rot}}\,\vec{v} - D \overrightarrow{\text{grad}}\ \tau = 0, \tag{2.43}$$

$$j\omega\tau + Q\ \text{div}\,\overrightarrow{\text{grad}}\ \tau - R\ \text{div}\,v = 0, \tag{2.44}$$

where $B = \frac{c_0^2}{\gamma} + j\omega c_0 l_v$, $C = -j\omega c_0 l_v'$, $D = \frac{j\omega\beta}{\rho_0}$, $Q = -\gamma l_h c_0$, $R = \frac{-(\gamma-1)\rho_0 c_0^2}{\gamma\beta}$. The corresponding weak forms, which can be implemented in FEM software, e.g. in Comsol Multiphysics, can be found in [31]. The acoustic pressure is then obtained from (2.8)

$$p = \beta\tau - \frac{\rho_0 c_0^2}{j\omega\gamma}\text{div}\,v. \tag{2.45}$$

The boundary conditions on the rigid isothermal wall are $v_x = v_y = v_z = 0$, $\tau = 0$. On the moving electrode (membrane) the corresponding velocity component is coupled with the wall displacement, for example $v_z = j\omega\xi$. An example of such coupling for a 2D axisymmetrical transducer is shown in [32]. If the problem is solved in 3D, the 2D weak form for the membrane displacement derived from eq. (2.29) takes the following form [32]

$$\iint_{\Gamma_M} \left[-\partial_x\xi\,\partial_x w_\xi - \partial_y\xi\,\partial_y w_\xi + k^2\xi w_\xi + \frac{p(x,y) - p_{inc}}{T} w_\xi\right] \text{d}\Gamma_M = 0, \tag{2.46}$$

where $\Gamma_M$ is the membrane part of the domain boundary and $w_\xi$ is the test functions related to the membrane displacement $\xi$. Note that this approach is used as the reference FEM model in section 4.2.3 ("The lumped element model").

Another approach is used in the Acoustic Module of Comsol Multiphysics software. The main difference is that the particle velocity $\vec{v}$, the temperature variation $\tau$ and the acoustic pressure $p$ are calculated simultaneously [33, 34, 35]. The fundamental laws are expressed as follows [35]

$$\begin{aligned} i\omega\rho_0\mathbf{v} - \nabla\cdot\left[-p\mathbb{I} + \mu(\nabla\mathbf{v} + \nabla\mathbf{v}^{\mathrm{T}}) - \left(\frac{2}{3}\mu - \mu_B\right)(\nabla\cdot\mathbf{v})\,\mathbb{I}\right] &= \mathbf{0}, \\ i\omega\rho + \rho_0\nabla\cdot\mathbf{v} &= 0, \\ i\omega\left(\rho_0 C_P\tau - pT_0\alpha_0\right) + \nabla\cdot(-\lambda_h\nabla\tau) &= 0, \end{aligned} \tag{2.47}$$

where

$$\begin{aligned} \rho &= \rho_0\left(\beta_T p - \alpha_0\tau\right), \\ \alpha_0 &= -\frac{1}{\rho_0}\left.\frac{\partial\rho_0}{\partial T_0}\right|_{P_0}, \\ \beta_T &= \frac{1}{\rho_0}\left.\frac{\partial\rho_0}{\partial P_0}\right|_{T_0}, \end{aligned} \tag{2.48}$$

the dependence of the equilibrium density $\rho_0$ on the static pressure $P_0$ and the static temperature $T_0$ being given by $\rho_0(P_0, T_0) = 0.02897P_0/(8.314\,T_0)$ [35].

The numerical modelling of the vibrating electrodes in the form of a flexible clamped plate (both perforated and unperforated) is based on the classical linear formulation [36]

$$\begin{aligned} -\omega^2\mathbf{u} &= \nabla\sigma_m, \\ \sigma_m &= \mathsf{C} : \varepsilon, \\ \varepsilon &= \frac{1}{2}\left([\nabla\mathbf{u}]^T + \nabla\mathbf{u}\right), \end{aligned} \tag{2.49}$$

where $\mathbf{u}$ is the displacement vector, $\sigma_m$ and $\varepsilon$ are the stress and strain tensor respectively, ':' stands for a double contraction over two indices ($\sigma_{ij} = \mathsf{C}_{ijkl}\,\varepsilon_{kl}$), $\mathsf{C}$ being the elasticity tensor whose elements depend on the Young's modulus $E$ and Poisson's ratio $\nu$ [36] (linear elastic isotropic material). Note that this approach is used in Chapter 3 ("A theoretical investigation into the behaviour of miniaturized transducers").

# Chapter 3

# A theoretical investigation into the behaviour of miniaturized transducers

This section is dedicated to a theoretical investigation into the behaviour of miniaturized transducers. Exploring and describing the behaviour of the MEMS microphone requires theoretical modelling, which should be chosen at the appropriate level of accuracy. The modelling methods described in several classical textbooks can be generally classified into three categories: equivalent circuit methods [37, 40], fully analytical approaches, which take into consideration the coupling effect between the moving plate and the fluid gap, and various numerical techniques section 2.4.6 ("Numerical methods"). The simple lumped-element model (discussed in 4.2.3 ("The lumped element model") seems to be sufficient to provide a good estimate of the behaviour of the microphone in the frequency range up to the frequency of the first resonance with low computational complexity. However, we want to explore the two other approaches, which can achieve greater precision. The author makes the following assumption: if the proposed methods work on a non-perforated plate, they are more likely to work on plates with perforation as the moving electrode of a MEMS transducer.

## 3.1 A non perforated plate as a moving electrode of the MEMS transducer

The transducer considered here (Fig. 3.1) consists of a square elastic clamped plate (moving electrode) with dimensions given in Table 3.1, set at the coordinate $z = 0$ and fixed at its periphery to a rigid frame whose coordinates $x$ and $y$ are equal to $\pm a$ in both directions. A thin fluid layer (an air gap herein) of thickness $h_g$ is trapped between the plate and a back rigid electrode having the same shape as the elastic plate. This fluid layer is loaded at its periphery by a small cavity of volume $V_c$.

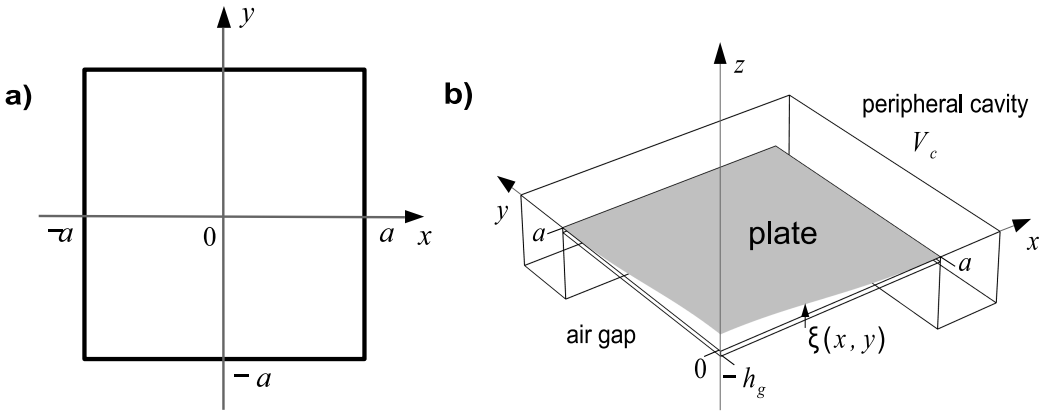


Figure 3.1: Geometry of the system: a) dimensions of the square plate, and b) geometry of the transducer in the $1^{st}$ quadrant.

| **Parameter** | **Value** | **Unit** |
|---|---|---|
| Plate half-side $a$ | $0.5 \cdot 10^{-3}$ | $m$ |
| Plate thickness $h_p$ | $10^{-6}$ | $m$ |
| Air-gap thickness $h_g$ | $10^{-6}$ | $m$ |
| Cavity volume | $10^{-10}$ | $m^3$ |

Table 3.1: Common dimensions of the system.

| **Parameter** | **Value** | **Unit** |
|---|---|---|
| Silicon diaphragm density $\rho_d$ | 2330 | $kg/m^3$ |
| Plate Poisson's ratio $\nu$ | 0.27 | – |
| Plate Young's modulus $E$ | $160 \cdot 10^9$ | $Pa$ |
| Adiabatic sound speed $c$ | 343.2 | $m \cdot s^{-1}$ |
| Air density $\rho_0$ | 1.20 | $kg \cdot m^{-3}$ |
| Shear dynamic viscosity $\mu$ | $1.81 \cdot 10^{-5}$ | $Pa \cdot s$ |
| Permittivity $\varepsilon_0$ | $8.8542 \cdot 10^{-12}$ | $F \cdot m^{-1}$ |
| Thermal conductivity $\lambda_h$ | $25.7 \cdot 10^{-3}$ | $W/(m \cdot K)$ |
| Specific heat coefficient at constant pressure per unit of mass $C_p$ | 1005 | $J/(kg \cdot K)$ |
| Ratio of specific heats $\gamma$ | 1.4 | – |

Table 3.2: Plate material and air properties.

### 3.1.1 The displacement field of a rectangular clamped plate

A monochromatic incident acoustic wave of angular frequency $\omega$ excites the plate; the incident pressure on the plate denoted below $p_{inc}$, is assumed to be uniform over the entire surface of the plate and the time factor is given by $e^{j\omega t}$. Then, the symmetrical movement with respect to the axes passing through the centre of the plate and parallel to its edges is the only movement considered here.

The equation which governs the complex amplitude of the displacement field of the plate loaded by acoustic fields on both sides $p_{inc}$ and $p$ can be written classically as [39]

$$\left[\frac{\partial^4}{\partial x^4} + 2\frac{\partial^4}{\partial x^2 \partial y^2} + \frac{\partial^4}{\partial y^4} - k_p^4\right] \xi(x,y) = \frac{1}{D}\left[-p_{inc} + p(x,y)\right], \tag{3.1}$$

The boundary conditions are

$$\xi(x,y) = \frac{\partial}{\partial x}\xi(x,y) = 0, x = \pm a, \forall y \in (-a,a), \tag{3.2}$$

$$\xi(x,y) = \frac{\partial}{\partial y}\xi(x,y) = 0, y = \pm a, \forall x \in (-a,a), \tag{3.3}$$

with $D = \frac{Eh_p}{12(1-\nu^2)}$ being the flexural rigidity, $\nu$ being the Poisson's ratio, $E$ is the Young's modulus, $h_p$ is the thickness of the plate, $k_p^4 = \frac{M_s}{D}\omega^2$ is the plate wave number, $M_s = h_p\rho_p$ is the mass per unit area, and $\rho_p$ is the density of the plate.

The general solution can be written as an expansion over the orthonormal eigenfunctions:

$$\xi(x,y) = \sum_{mn} \xi_{mn}\psi_{mn}(x,y), \tag{3.4}$$

where $\psi_{mn}$ (with $m,n = 1,2\ldots$) are the solutions of the homogeneous equation associated with eq.(3.1):

$$\left(\Delta\Delta - k_{mn}^4\right)\psi_{mn} = 0, \tag{3.5}$$

with $k_{mn}^4 = \left(k_{xm}^2 + k_{yn}^2\right)^2$. The modal coefficients $\xi_{mn}$ are then given by [19]

$$\xi_{mn} = \frac{1}{D\left[\left(k_{xm}^2 + k_{yn}^2\right)^2 - k_p^2\right]} \cdot \int_{-a}^{a}\int_{-a}^{a} \psi_{mn}(x,y)[p(x,y) - p_{inc}]\,\mathrm{d}x\mathrm{d}y. \tag{3.6}$$

#### 3.1.1.1 An approximate analytical expression of eigenfunctions [A.6]

A thorough search of the relevant literature did not yield any result, indicating there is an exact analytical expression for the eigenfunctions that describe the modal behavior of the square clamped plate. Nevertheless, the right eigenfunctions can be obtained for a plate with particular parameters. They can be reconstructed using various approaches, and the

coefficients can subsequently be fitted in order to make this method applicable for any plate dimensions.

The homogeneous equation associated with (3.1) has been solved numerically by the finite element method using Comsol Multiphysics software, and these numerically calculated eigenfunctions ${}^{n}\psi_{mn}$ of the clamped plate are then approximated using double cosine series

$$\psi_{mn}(x,y) = \sum_{q,r=1}^{N} c_{(qr),(mn)} \cos\left(\frac{\pi q x}{2a}\right) \cos\left(\frac{\pi r y}{2a}\right), \tag{3.7}$$

with $q, r = 1, 3, 5, \ldots N$. The coefficients of the series have been calculated from the numerically calculated eigenfunctions ${}^{n}\psi_{mn}$, using the relation

$$c_{(qr),(mn)} = \frac{4}{a^2} \int_{-a}^{a} \int_{-a}^{a} {}^{n}\psi_{mn}(x,y) \cdot \cos\left(\frac{\pi q x}{2a}\right) \cos\left(\frac{\pi r y}{2a}\right) \mathrm{d}x\mathrm{d}y, \tag{3.8}$$

where all integration has been performed numerically. The eigenvalues $k_{xm}$, $k_{yn}$ are expressed from the numerically calculated eigenfrequencies ${}^{num}f_{mm}$, as follows

$$k_{xm} = \sqrt{\frac{2\pi\ {}^{num}f_{mm}}{2c_p}}, \tag{3.9}$$

where $c_p = \sqrt{D/M_s}$ is the wave speed on the plate and $k_{yn}$ has the same values as $k_{xm}$ in the case of a square plate.

These coefficients are calculated for several different parameters (plate side $a$, thickness $h_p$ and flexural rigidity $D$). Finally it is concluded that the coefficients $c_{(qr),(mn)}$ depend only on the plate side $a$, and this dependence is found to be linear. Each coefficient $c_{(qr),(mn)}$ can then be fitted using the following relation, which provides an opportunity to get regression coefficients for any plate dimensions

$$c_{(qr),(mn)} = s_{1(qr),(mn)} a + s_{2(qr),(mn)}. \tag{3.10}$$

The coefficients $s_{1(qr),(mn)}$, $s_{2(qr),(mn)}$ are given in Appendix A.1. The eigenvalues $k_{xm}$ and $k_{yn}$ have been fitted by the same way.

The analytical approach relies on the integral formulation of the acoustic pressure in the thin fluid layer (section 2.4 "Modelling miniaturized devices") coupled with the plate displacement, in other words, using the approximated eigenfunction discussed above and inserting (2.35) into the equation (3.6) we get $\xi_{mn}$. This equation can be rewritten in matrix form

$$[-\mathbb{A} + \mathbb{B}](\Xi) = (C), \tag{3.11}$$

where $(\Xi)$ and $(C)$ are the column vectors of elements $\xi_{mn}$ and $c_{mn} = -p_{inc} \int_{-a}^{a} \int_{-a}^{a} \psi_{mn}(x,y) \mathrm{d}x\mathrm{d}y$, respectively, $\mathbb{B}$ is a diagonal matrix of elements $D\left[\left(k_{xm}^2 + k_{yn}^2\right)^2 - k_p^2\right]$ and the elements of the matrix $\mathbb{A}$ are given by [15]

$$
\begin{aligned}
A_{(mn),(qr)} =& \frac{\rho_0\omega^2}{h_g F_v}\int_{-a}^{a}\int_{-a}^{a}\Bigg[\psi_{mn}(x,y) \\
& \cdot \int_0^a\int_0^a G(x,x_0;y,y_0)\psi_{qr}(x_0,y_0)\mathrm{d}x_0\mathrm{d}y_0 \\
& - \frac{1}{1+\langle I_G(x,a)\rangle_x} \\
& \cdot \int_0^a\int_0^a \langle G(x,x_0;a,y_0)\rangle_x \\
& \cdot \psi_{qr}(x_0,y_0)\mathrm{d}x_0\mathrm{d}y_0 \\
& \Bigg\{\left[\frac{j\omega\rho_0}{8F_v Z_c h_g a}\psi_{mn}(x,y) + \partial_y\psi_{mn}(x,y)\right] \\
& \cdot \int_0^a G(x,x_0;y,a)\mathrm{d}x_0 \\
& + \left[\frac{j\omega\rho_0}{8F_v Z_c h_g a}\psi_{mn}(x,y) + \partial_x\psi_{mn}(x,y)\right] \\
& \cdot \int_0^a G(x,a;y,y_0)\mathrm{d}y_0\Bigg\}\Bigg]\mathrm{d}x\mathrm{d}y.
\end{aligned}
\tag{3.12}
$$

All the notation used here is the same as in section 2 ("Current practices and developments in noise monitoring technology"), including the Green's function given by equations (2.39) and (2.40). As for the terms with the spatial derivatives of $\partial_x\psi_{mn}(x,y)$, $\partial_y\psi_{mn}(x,y)$ in the eq. (3.12), they are odd functions in the direction of the derivative and their integrals over the surface are zero. The functions $\int_0^a G(x,x_0;y,a)\mathrm{d}x_0$, $\int_0^a G(x,a;y,y_0)\mathrm{d}y_0$ are even functions with the same shape. The multiplication of such an even function with an odd function results in an odd function, so it is clear that the spatial derivatives vanish.

Finally, a comparison between the obtained result and the numerical result is critical for assessing the proposed method and any differences must be carefully interpreted. Figure 3.2 displays the eigenfunction reconstructed using 2D cosine series (the test result) versus the numerically calculated eigenfunction.

While the difference and comparison graphs provide visual impressions of the error between the test result and comparative result, the estimates of these errors accounting for varying number of members of the series can be calculated as follows

$$
Err = \sqrt{\frac{\sum_{i=1}^{M}(\psi_{mni} - {}^{n}\psi_{mni})^2}{\sum_{i=1}^{M}{}^{n}\psi_{mni}{}^2}}\cdot 100\%, \tag{3.13}
$$

where $\psi_{mni}$ is the value of the approximate $\psi_{mn}$ at the i-th node of the mesh used for calculating the numerical result (similarly for the reference numerically calculated eigenfunction ${}^{n}\psi_{mn}$), and $M$ is the number of mesh nodes. It is clear from Fig. 3.3, that an approximate expression in the form of the two-dimensional cosine series proposed here unfortunately

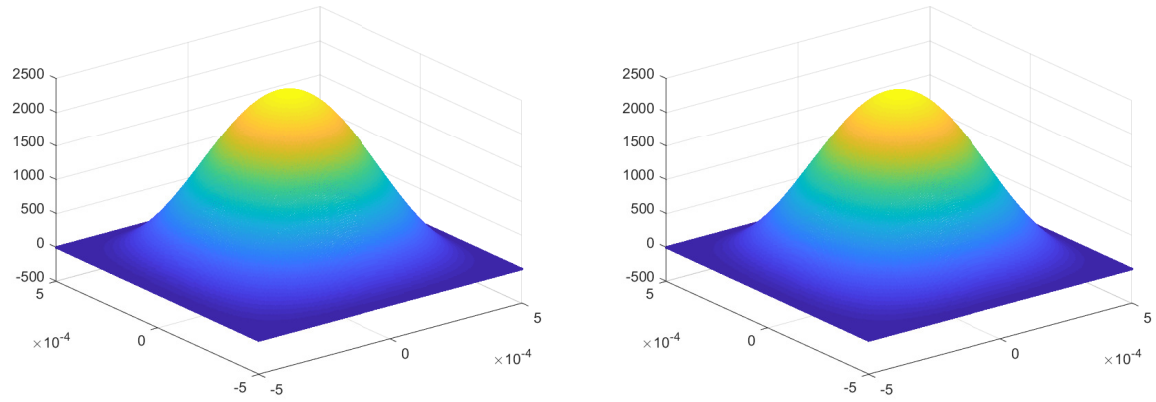


Figure 3.2: The numerically calculated eigenfunction (left) and the reconstructed eigenfunction (right) using 2D cosines series (m,n=1,1 here).

suffers from relatively slow convergence.

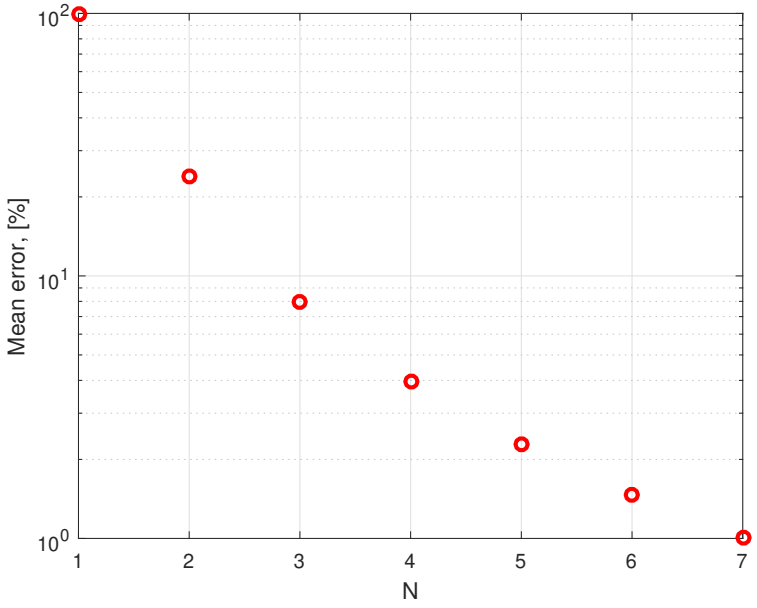


Figure 3.3: Error estimate versus the summation limit N in eq. (3.7).

The frequency dependence of the pressure sensitivity given by $\sigma = -U_0 \frac{\bar{\xi}}{p_{inc} h_g}$ (with polarization voltage $U_0 = 30V$ and mean displacement of the plate $\bar{\xi} = [\int_0^a \int_0^a \xi(x,y)\mathrm{d}x\mathrm{d}y]/a^2$) (sec. 2.4.2) obtained by using this form of eigenfunctions to describe the behavior of the transducer with the rectangular clamped plate has been verified by the numerical FEM model using the Comsol Multiphysics, version 5.3 software. The complete linear 3D model

of the transducer has been developed, taking into account the thermoviscous losses and the strong coupling between the displacement field of the clamped plate and the acoustic field in the thin fluid layer in the fluid without any further approximation. The results (Fig. 3.4) show good agreement between the approximate solution presented in this section and the exact numerical (FEM) solution against which the analytical results are tested. The detail of the flat part of the frequency response presented in Fig. 3.5 shows that the difference between the approximate analytical result and the reference numerical result does not exceed 0.2 dB in this frequency range that is of interest for audio applications.

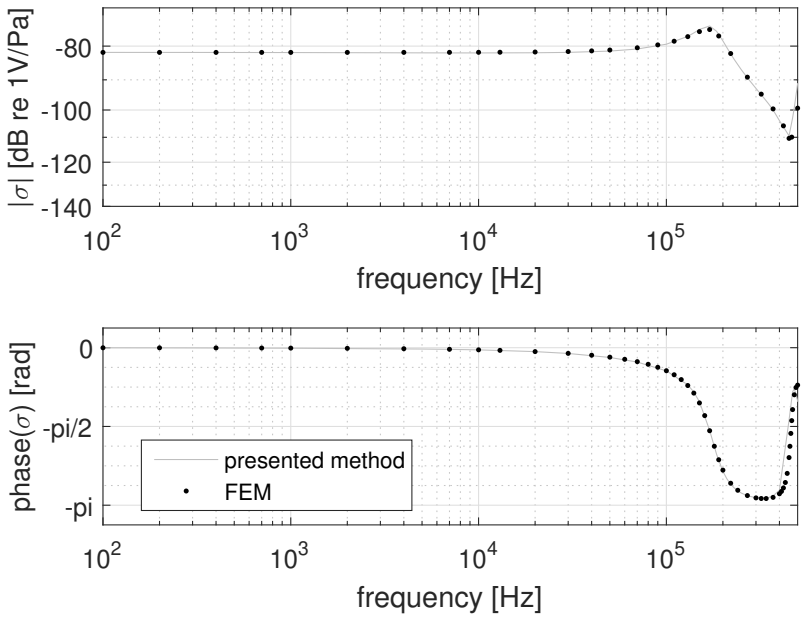


Figure 3.4: A comparison between the acoustic pressure sensitivity obtained using 2D cosine series coefficients (full line) and FEM simulations (circules).

#### 3.1.1.2 Eigenfunctions of a 1D beam

In this section, the construction of the solutions of equations (3.1) to (3.3) presented above relies on the known modal wave functions of the 1D beam that are solutions of the homogeneous equations

$$\left[\frac{\mathrm{d}^4}{\mathrm{d}x^4} - \alpha_m^4\right]\phi_m(x) = 0 \quad \text{and} \quad \left[\frac{\mathrm{d}^4}{\mathrm{d}y^4} - \alpha_n^4\right]\phi_n(y) = 0. \tag{3.14}$$

The solutions of the equation (3.14) for the coordinate $x$ and $y$, eigenfunctions and eigenvalues, take the symmetric form and the antisymmetric form. However, the symmetric solution is the only solution that is useful in our problem

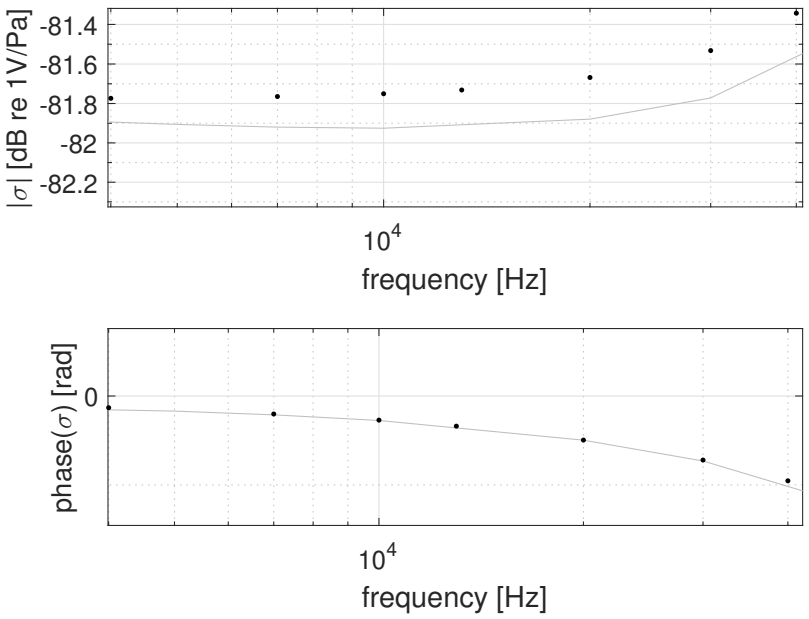


Figure 3.5: Detailed view of the sensitivity module.

$$\phi_m^s(x) = \frac{1}{\sqrt{2}a}\left[\frac{\cos(\alpha_m^s x)}{\cos(\alpha_m^s a)} - \frac{\cosh(\alpha_m^s x)}{\cosh(\alpha_m^s a)}\right], \quad \text{where} \quad \tan(\alpha_m^s a) = -\tanh(\alpha_m^s a), \tag{3.15}$$

and similarly for $\phi_n^s(y)$. These eigenfunctions have been used for example in [19] to construct the approximated eigenfunctions for the clamped plate in the form of $\psi_{mn}(x,y) = \phi_m^s(x) \cdot \phi_n^s(y)$. Such an eigenfunction does not verify the equation (3.5), but verifies the boundary conditions (3.2), (3.3), unlike the cosine functions used in section 3.1.1.1 ("An approximate analytical expression of eigenfunctions").

#### 3.1.1.3 1D beam eigenfunctions as the basis of the series [A.5]

As an improvement to the model described in 3.1.1.1, the eigenfunctions $\psi_{mn}(x,y)$ can be approximated, similarly to (3.7), using the eigenfunctions of a 1D beam (3.15) instead of the cosine functions, as follows

$$\psi_{mn}(x,y) = \sum_{q,r=1}^{N} c_{(qr),(mn)}\ \phi_q^s(x) \cdot \phi_r^s(y), \tag{3.16}$$

the coefficients $c_{(qr),(mn)}$ are obtained as in the previous case

$$c_{(qr),(mn)} = \frac{4}{a^2}\int_{-a}^{a}\int_{-a}^{a} {}^n\psi_{mn}(x,y) \cdot \phi_q^s(x) \cdot \phi_r^s(y)\,\mathrm{d}x\mathrm{d}y. \tag{3.17}$$

In this case, the approximate eigenfunctions verify the boundary conditions, as mentioned above. Fig. 3.6 shows significantly smaller differences between the approximate eigenfunctions and the reference numericall eigenfunctions (here for the first mode ${}^{n}\psi_{11}$) for different numbers of the elements $N$ of the series (3.16), in comparison with the previous approximation using the cosine functions.

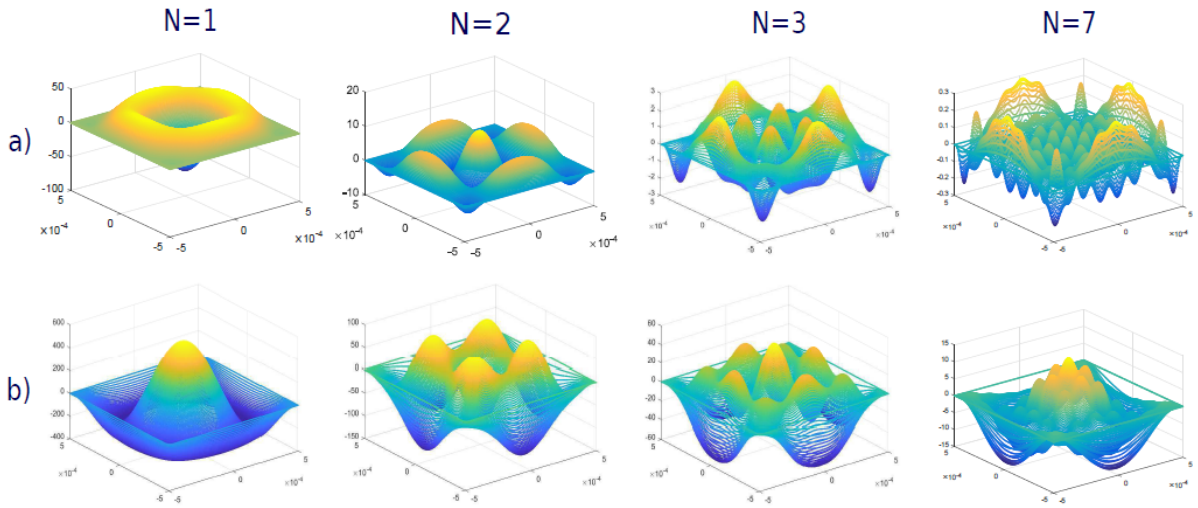


Figure 3.6: Difference between the numerical solution ${}^{n}\psi_{(}11)$ and a) an analytical approximation using the eigenfunctions of a 1D beam eq.(3.15) and b) an approximation from 3.1.1.1.

The mean error, calculated using (3.13) depicted in Fig. 3.7, presents much faster convergence with increasing numbers of elements $N$ of the series (3.16) than in the previous case.

Fig. 3.8 shows the frequency dependence of the acoustic pressure sensitivity of the transducer calculated using the approximation described in this section, in contrast with the numerically calculated approximation. Good agreement is obtained. The difference in the flat part of the curve does not exceed 0.2 dB, but the damping of the resonances seems to be slightly underestimated.

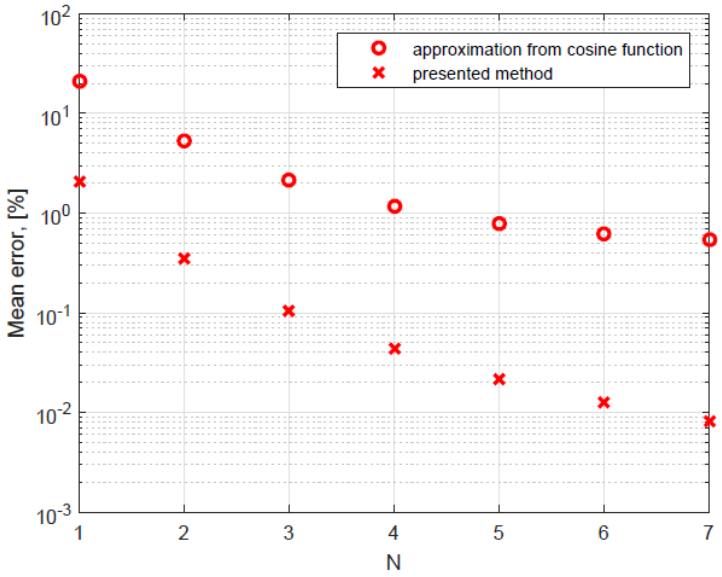


Figure 3.7: Mean error of the approximation for $m, n = 1, 1$ using cosine functions (circles) and 1D beam eigenfunctions (crosses).

#### 3.1.1.4 Analytical solution [A.2]

In order to express the modal behavior of the square clamped plate, it is also possible to construct the solution using the analytically given modal function (3.15)

$$ {}^{a}\psi_{mn}(x,y) = \phi_m^s(x) \cdot \phi_n^s(y), \tag{3.18} $$

and the solution for the plate displacement is searched for in the form

$$ \xi(x,y) = \sum_{mn} \xi_{mn} {}^{a}\psi_{mn}(x,y). \tag{3.19} $$

Even though ${}^{a}\psi mn(x,y)$ does not satisfy the eigen-problem of the plate but satisfies only the boundary conditions (3.2) and (3.3), because here the coefficients $\xi_{mn}$ are assumed to reflect an elastic coupling mechanism between the 1-D modal solutions along the two axes $x$ and $y$. When the expression (3.19) is substituted into the equation for the displacement field of the plate (3.1) it is found that

$$ \sum_{m,n} \xi_{mn} \left(\alpha_m^4 + \alpha_n^4 - k_p^4\right) {}^{a}\psi mn(x,y) + 2 \sum_{m,n} \xi_{mn} \phi_m''(x) \phi_n''(y) = \frac{1}{D} \left[-p_{inc} + p(x,y)\right], \tag{3.20} $$

where $(''$) means the second spatial derivative.

Accounting for the orthogonality of the normalized modal functions ${}^{a}\psi_{mn}(x,y)$, the inner product defined as $\left[\int_{-a}^{a}\int_{-b}^{b} f_1(x,y)\, f_2(x,y)\, \mathrm{d}x\mathrm{d}y\right]$ of equation (3.20) and ${}^{a}\psi_{m'n'}(x,y)$

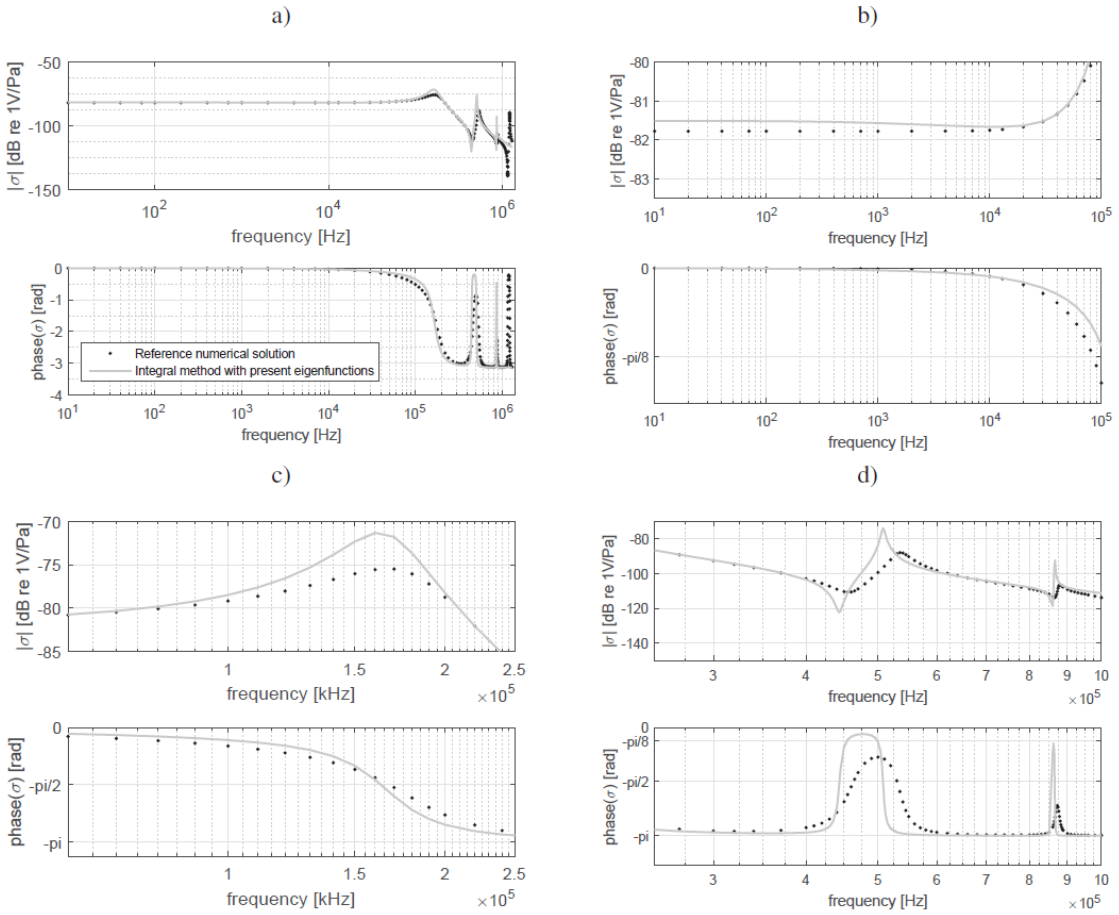


Figure 3.8: A comparison between the acoustic pressure sensitivity obtained using 1D beam normalized eigenfunction (full line) and the eigenfunction obtained from FEM simulations (black points), module and phase of the sensitivity, a) in the whole frequency range (20 Hz - 1 MHz) b) a detail on the flat part of the frequency response (10 Hz - 100 kHz), c) a detail on the first resonance, and d) a detail on the frequency range of higher modes of the plate.

leads readily to

$$\left(K_{mn}^4 - k_p^4\right)\xi_{m'n'} + 2\sum_{mn}\sigma_{mm'}\tau_{nn'}\xi_{mn} = Q_{m'n'}, \tag{3.21}$$

where

$$\sigma_{mm'} = \int_{-a}^{a}\phi_m''(x)\phi_{m'}(x)\mathrm{d}x \tag{3.22}$$

and

$$\tau_{nn'} = \int_{-a}^{a}\phi_n''(y)\phi_{n'}(y)\mathrm{d}y. \tag{3.23}$$

Considering the requirement on vectors to be orthonormal, we get

$$\sigma_{mm'}(x) = \frac{4\alpha_m^2\alpha_{m'}^2}{a\left(\alpha_m^4 - \alpha_{m'}^4\right)}\left[\alpha_m \tan\left(\alpha_m a\right) - \alpha_{m'}\tan\left(\alpha_{m'}a\right)\right] \tag{3.24}$$

if $m = m'$, otherwise

$$\sigma_{mm'}(x) = -\frac{\alpha_m}{a}\tan\left(\alpha_m a\right)\left[1 + \alpha_m a \tan\left(\alpha_m a\right)\right], \tag{3.25}$$

the same applies for $\tau_{nn'}$. Going back to the eq.(3.21), we have

$$Q_{m'n'} = \int_{-a}^{a}\int_{-a}^{a}\frac{1}{D}\left[-p_{inc} + p(x,y)\right]{}^a\psi_{m'n'}(x,y)\,\mathrm{d}x\mathrm{d}y, \tag{3.26}$$

and

$$K_{mn}^4 = \alpha_m^4 + \alpha_n^4. \tag{3.27}$$

Substituting the acoustic pressure $p(x,y)$ given by eq.(2.35) to eq. (3.26) leads to the expression of the modal coefficients $\xi_{mn}$ from eq. (3.21) rewritten in the matrix form as follows

$$\left([\mathbb{A}] - [\mathbb{C}] - [\mathbb{H}]\right)(\Xi) = (E), \tag{3.28}$$

where $[\mathbb{A}]$ is the "plate-fluid" coupling square matrix of elements

$$A_{mn,m'n'} = \int_{-a}^{a}\int_{-a}^{a} B_{mn}(x,y)\,{}^a\psi_{m'n'}(x,y)\,\mathrm{d}x\mathrm{d}y, \tag{3.29}$$

where the known functions $B_{mn}(x,y)$ are given by (note that $p(x,y) = \sum_{mn} B_{mn}(x,y)\,\xi_{mn}$)

$$B_{mn}(x,y) = \zeta\int_0^a\int_0^a\left[G(x,x_0;y,y_0) + \frac{I_G(x,y)\left\langle G(x,x_0;y,y_0)\right\rangle}{1 + \left\langle I_G(x,a)\right\rangle}\right]{}^a\psi_{mn}(x_0y_0)\,\mathrm{d}x_0\mathrm{d}y_0. \tag{3.30}$$

Matrix $[\mathbb{C}]$ is the "internal elastic plate coupling" square matrix of elements

$$C_{mn,m'n'} = 2D\sigma_{mm'}\tau_{nn'}, \tag{3.31}$$

and $[\mathbb{H}]$ is the diagonal matrix of elements (which include the effects of the eigenvalues)

$$H_{m'n'} = D\left[K_{m'n'}^4 - k_p^4\right], \tag{3.32}$$

and where $(\Xi)$ and $(E)$ are the column vectors of, respectively, the unknown coefficients $\xi_{m'n'}$ and the elements $E_{m'n'}$, which involve the external source pressure field $p_{inc}$,

$$E_{m'n'} = p_{inc}\int_{-a}^{a}\int_{-a}^{a}{}^a\psi_{m'n'}(x,y)\,\mathrm{d}x\mathrm{d}y. \tag{3.33}$$

Note that two main differences between the method presented here and the method described in [19] are the presence of the term related to the "internal elastic plate coupling"

expressed in matrix $[\mathbb{C}]$ and the use of the integral formulation for the acoustic pressure field in the fluid gap, which prevents us from using the truncated multimodal expression leading to coupling of the Neumann and Dirichlet modes.

A comparison between the analytical results presented here, using the first 4 eigenmodes and the result obtained numerically for the real part of the plate displacement field in metres, is presented in Figure 3.9. Good agreement can be noted. A slightly overestimated amplitude (520 kHz) and a small difference in shape (800 kHz) can be found only at very high frequencies.

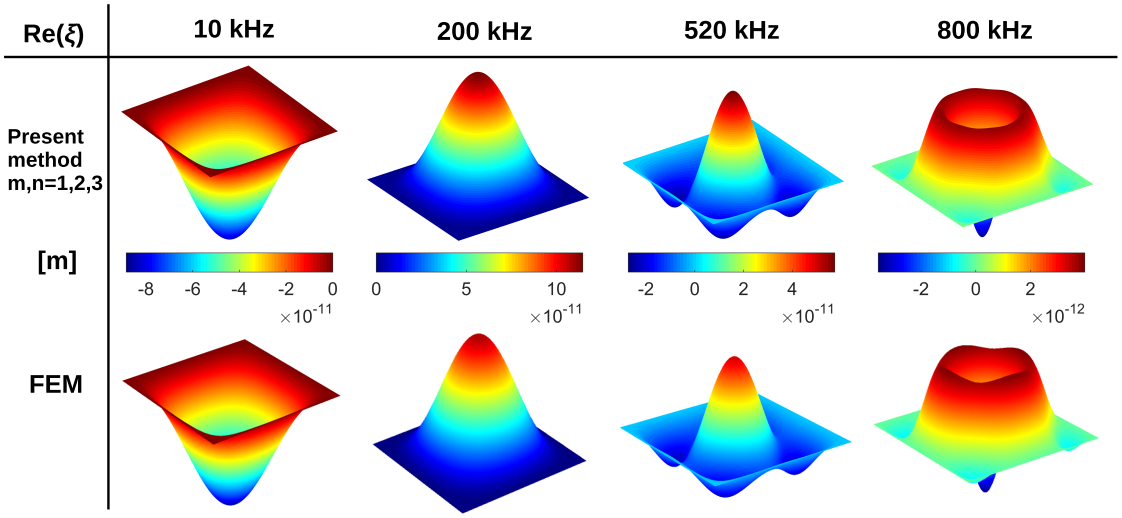


Figure 3.9: The real part of the plate displacement in metres given by the analytical method and by the FEM method at 10kHz, 200kHz, 520kHz and 800kHz.

Figures 3.10 - 3.13 present a comparison between the frequency dependence of the pressure sensitivity obtained from the method proposed here for different numbers of eigenmodes and the numerical result obtained from same numerical FEM model, as was used in the previous chapter (points) of the whole structure (a plate coupled with air-filled acoustic elements). The analytical results are tested against Comsol Multiphysics software in Figures 3.10 - 3.13.

Fig. 3.11 shows that the difference between the analytical result and the numerical results diminishes with increasing numbers of series elements (3.19). Note that this difference does not exceed 0.25 dB in the audio frequency range (20 Hz - 20 kHz) when the first nine terms in the series $(m, n = 1, 2, 3)$ are used. Figures 3.12, 3.13 show the details of the sensitivity near the first resonance (50 kHz - 220 kHz) and in the higher frequency range (300 kHz - 1.3 MHz), respectively, where the solution with four terms in the series $(m, n = 1, 2)$ is no longer able to provide correct results above approximately 1 MHz, while the solution with nine terms $(m, n = 1, 2, 3)$ still remains very close to the reference numerical solution.

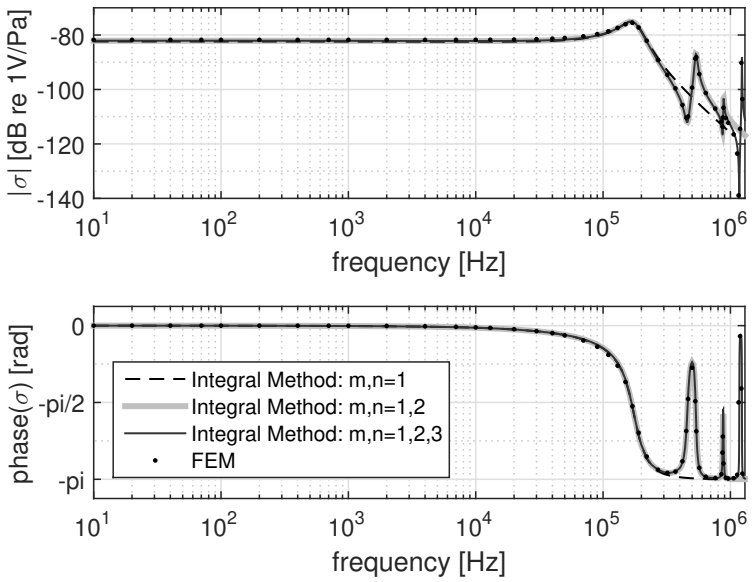


Figure 3.10: A comparison between the acoustic pressure sensitivity obtained using the present method (full and dashed lines) and the value obtained from FEM simulations (black points).

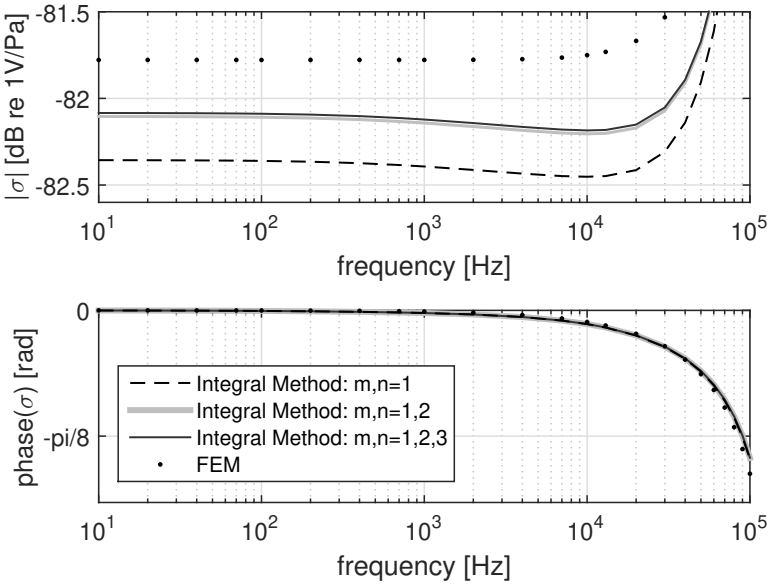


Figure 3.11: Module and phase of the sensitivity in the flat part of the frequency response.

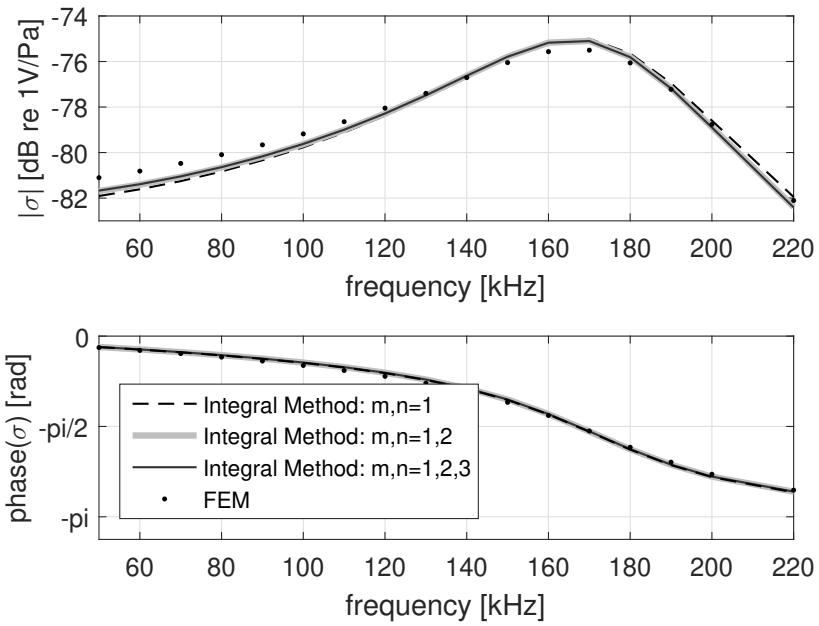


Figure 3.12: Detailed view of the sensitivity module and the phase near the first resonance.

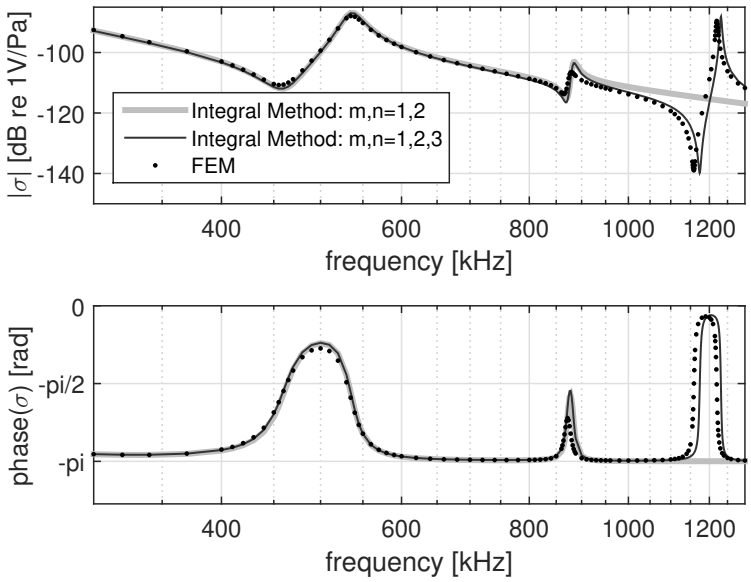


Figure 3.13: Detailed view of the sensitivity module and the phase in the higher frequency range.

## 3.2 A perforated plate as a moving electrode of the MEMS transducer

Modelling perforated plates could be a challenging task, due to the complexity of their shape and due to the fact that a perforated plate contains many tiny cutouts. The simplest and most common shapes of holes of MEMS are square holes in a straight row. For simplicity, we will approximate the perforation cell as a circle in this study, and we will introduce an analytical model which is accurate in a specific range of dimensions such as the perforation ratio $R$, which reflects how much of the plate surface is occupied by holes, the plate thickness (or the length of the perforation) $h_p$, and hole number $N$. The geometry that was used is shown in Fig. 3.14.

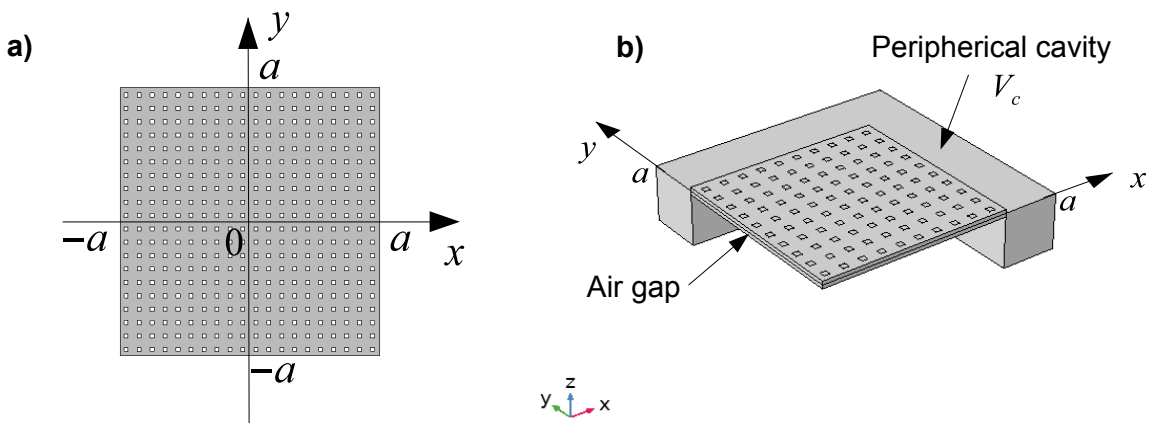


Figure 3.14: Geometry of the transducer: a) the dimensions of the perforated plate, b) a 3D cut view of the transducer in the 1st quadrant.

The coupling effect seems to be relatively simple, but it becomes increasingly complex when plate perforation occurs. In order to find out what happens to an airgap - perforated plate coupled system, it is necessary to address fundamental concepts and principles of physics. This chapter will investigate the vibration behaviour of a clamped perforated plate in an effort to reveal the science behind the coupling problem.

### 3.2.1 Acoustic pressure in the gap

Let us consider an infinitesimal volume element of the gap as represented in Figure 3.16, while a sketch of the whole system is shown in Fig. 3.15.

To construct the governing equation of motion, it is necessary to assemble the mass flow rate entering the gap element as the dynamic response. This task involves a twofold effort: firstly,assembling the mass flow rate along the x- and the y- axis in a given control volume of the air gap:

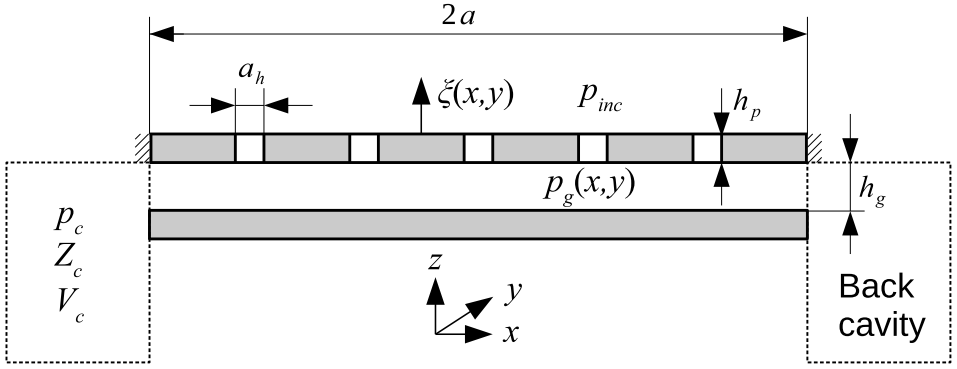


Figure 3.15: Sketch of the whole system.

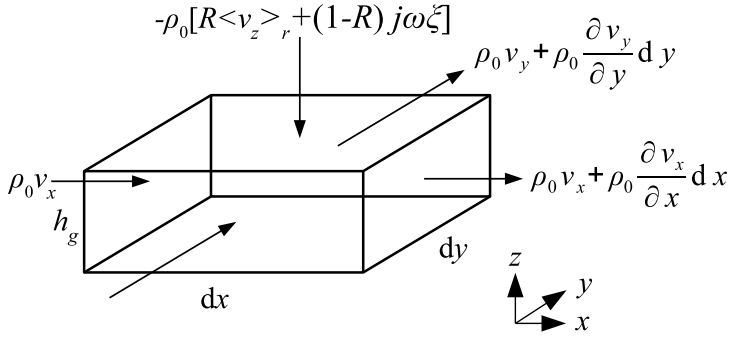


Figure 3.16: Element of the fluid gap.

$$\begin{aligned}\rho_0 v_x h_g\,dy-\left\{\rho_0 v_x+\frac{\partial v_x}{\partial x}\,dx\rho_0\right\}\,dyh_g&=-\rho_0\frac{\partial v_x}{\partial x}h_g\,dx\,dy\\ \rho_0 v_y h_g\,dx-\left\{\rho_0 v_y+\frac{\partial v_y}{\partial y}\,dy\rho_0\right\}\,dxh_g&=-\rho_0\frac{\partial v_y}{\partial y}h_g\,dx\,dy\end{aligned}\tag{3.34}$$

Secondly, while the force (incident pressure) is acting in the system, the fluid (air) is entering along the vertical axis, resulting in mass movement, which refers to a term consisting of two components: one that expresses the motion of the plate itself through the mass flow rate, which is similar to the case of a non-perforated plate or eq. (2.24), except for the surface occupied by the perforation

$$-j\omega\xi(x,y)\rho_0(1-R)\,dx\,dy,\tag{3.35}$$

where $R=\frac{\sum^N S_d}{4a^2}$ is the perforation ratio. The second term, which occurs in this case as an indicator of the impact of the perforation on the total mass flow rate, with $F_{v_d}=1-\frac{2J_1(k_v R_h)}{k_v R_h J_0(k_v R_h)}$ being the mean value of the normalized profile function of the particle velocity in the perforation, $R_h=\sqrt{a_h^2/\pi}$ being the equivalent radius of the circular perforation

$$-\rho_0 \langle v_z \rangle_r R\, dx\, dy = \frac{-F_{v_d}}{j\omega} \frac{p_{inc} - p(x,y)}{h_p}\, dx\, dy. \tag{3.36}$$

Utilizing the law of conservation of mass on the equations (3.34), (3.35), (3.36) we got

$$\begin{aligned} -\rho_0 \frac{\partial v_x}{\partial x} h_g\, dx\, dy - \rho_0 \frac{\partial v_y}{\partial y} h_g\, dx\, dy - \rho_0 \langle v_z \rangle_r R\, dx\, dy \\ + (1-R)\left(-j\omega\xi(x,y)\right)\, dx\, dy \rho_0 = j\omega\rho h_g\, dx\, dy. \end{aligned} \tag{3.37}$$

Applying the Navier-Stokes equation and Fourier's law of heat conduction as well as the equation of state, as in section 2.4.3 ("General governing equations"), we then obtain

$$\begin{aligned} h_g F_{vg} \left( \frac{\partial^2 p(x,y)}{\partial x^2} + \frac{\partial^2 p(x,y)}{\partial y^2} \right) + \frac{R p_{inc} F_{v_d}}{h_p} + (1-R)\,\omega^2 \rho_0 \xi(x,y) \\ = -\frac{\omega^2}{c_0^2} \left[ 1 + (\gamma - 1)(1 - F_{hg}) \right] p(x,y) + \frac{R F_{v_d}}{h_p} p(x,y). \end{aligned} \tag{3.38}$$

The wave equation governing the propagation of the acoustic pressure in the air gap is the second order partial differential equation given by

$$\left(\partial_{xx}^2 + \partial_{yy}^2 + \chi^2\right) p(x,y) = -U(x,y), \tag{3.39}$$

where the complex wavenumber accounting for the effect of the thermoviscous losses in the air gap and the 2nd term here represents the effect of the volume velocity coming though the perforation

$$\chi^2 = \frac{\omega^2}{c_0^2} \left[ \frac{1 + (\gamma - 1)(1 - F_{hg})}{F_{vg}} \right] - \frac{R F_{v_d}}{h_p h_g F_{vg}}. \tag{3.40}$$

The presence of perforation can be identified in a source term on the right-hand side of the equation (3.39), namely

$$U(x,y) = (1-R)\,\zeta\xi(x,y) + \frac{R p_{inc} F_{v_d}}{h_p h_g F_{vg}}, \tag{3.41}$$

where, for the sake of simplicity, we use $\zeta = \frac{\rho_0 \omega^2}{h_g F_v}$. Then the integral method can be used to obtain the solution of the equation (3.39)

$$p(x,y) = \int_{-a}^{a} \int_{-a}^{a} G(x, x_0; y, y_0)\, U(x_0, y_0)\, \mathrm{d}x_0 \mathrm{d}y_0 - p_c I_G(x,y), \tag{3.42}$$

where $G(x, x_0; y, y_0)$ denotes Green's function calculated in the 1st quadrant, eq.(2.39) and $I_G$ calculated as eq. (2.36). The pressure in the peripheral cavity is assumed to be equal to the mean value of the pressure at periphery of the air gap $p_c = \langle p(x,a) \rangle_x$, thus

$$p_c = \int_0^a p_g(x,a)\mathrm{d}x = \frac{1}{1 + \langle I_G(x,a) \rangle_x} \int_0^a \int_0^a \langle G(x, x_0; a, y_0) \rangle_x\, U(x_0, y_0) \mathrm{d}x_0 \mathrm{d}y_0, \tag{3.43}$$

where the symbol $\langle\rangle_x$ denotes the mean value over the x-coordinate.

### 3.2.2 Approximation of modal coefficients [A.4]

The analytical expression of eigenfunctions $\psi_{mn}$ presented here is based on an approximation of their numerical (FEM) solution, as in sec. 3.1.1.3. It employs the symmetric eigenfunctions of the 1D beam known from Chapter 3.1.1.2 ("Eigenfunctions of a 1D beam") as the basis of the series in the following manner

$$\psi_{mn}(x,y) = \sum_{q=1}^{N}\sum_{r=1}^{N} c_{(qr),(mn)}\phi_q(x)\,\phi_r(y)\,, \tag{3.44}$$

$\phi_q(x)$ and $\phi_r(x)$ are in the same form given by 3.15.

The coefficient $c_{(qr),(mn)}$ has been calculated from the numerically calculated eigenfunctions of the perforated plate ${}^n\psi_{mn}$, as follows

$$c_{(qr),(mn)} = \frac{1}{2a^2}\int_{-a}^{a}\int_{-a}^{a} {}^n\psi_{mn}\phi_q(x)\,\phi_r(x,y)\mathrm{d}x\mathrm{d}y. \tag{3.45}$$

A comparison between the analytical approximation of the eigenfunction and its numerically (FEM) calculated solution (both presented in Fig. 3.17 for the 1st mode) reveals the accuracy of the proposed method.

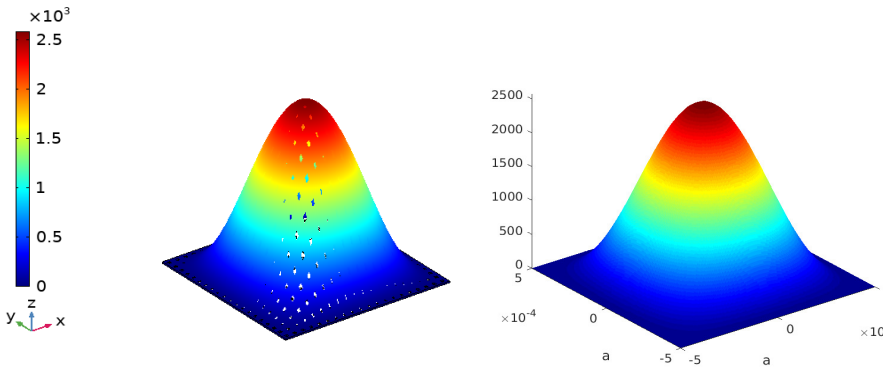


Figure 3.17: Eigenfunction $\psi_{11}(x,y)$ of the perforated plate given a) by a numerical solution and b) by an analytical approximation.

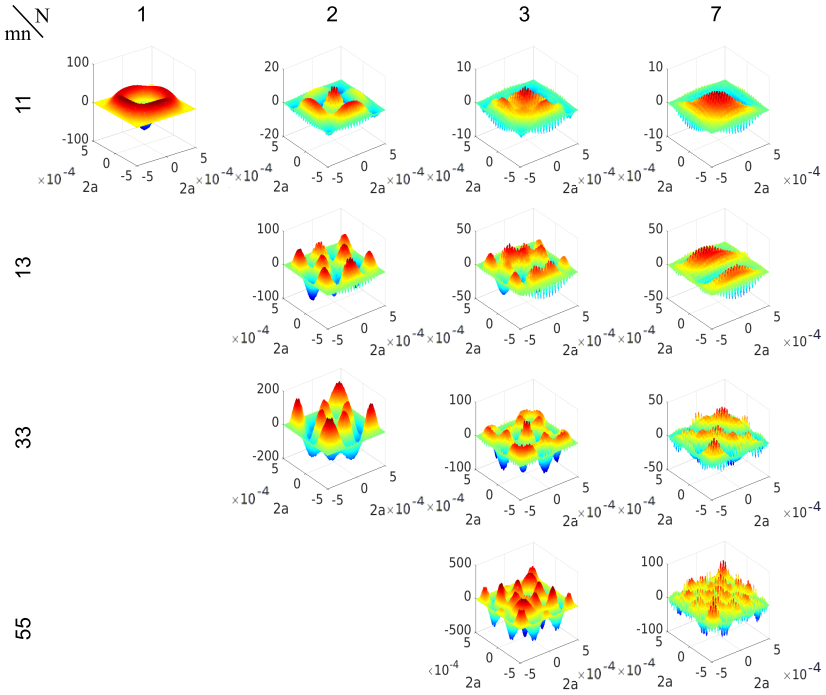


Figure 3.18: Differences between the eigenfunctions given by the numerical solution and by the present analytical approximation for given $m, n$ and $N$.

The differences between the eigenfunctions ${}^{n}\psi_{mn}(x, y)$ given by the numerical solution and the values given by the present analytical approximation $\psi_{mn}(x, y)$ for modes 11, 13, 33 and 55 for the number $N^2$ of coefficients in the series (3.44) ($N$ being the summation limit) is shown in Fig. 3.18.

In order to analyze the differences between the reference numerical solution and the approximate solution, the mean error is calculated using eq.(3.13). Fig. 3.19 shows the decreasing mean error as the number of terms increases to a certain level.

### 3.2.3 Coupling between the perforated plate displacement and the acoustic pressure in the thin fluid layer

In order to express modal coefficients $\xi_{mn}$, the solution for the acoustic pressure (3.42) has to be substituting into (3.6), taking into account (3.41), where the approximate eigenfunctions from section 3.2.2 ("Approximation of modal coefficients") have to be used. Note the different indexing $q, r$ in the sum contained in the solution of the acoustic pressure (3.42) which does not mix up with $m, n$ indexing of the modal coefficients. The integral in (3.6) then splits into two integrals, the first of them being expressed as follows

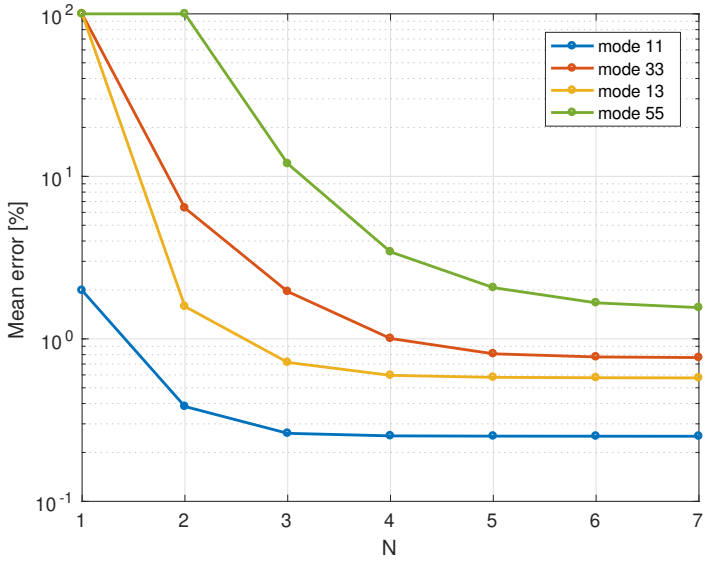


Figure 3.19: Mean error of the approximation of $\psi_{mn}(x,y)$.

$$
\begin{aligned}
&\int_{-a}^{a}\int_{-a}^{a}\psi_{mn}\left(x,y\right)p_g(x,y)\mathrm{d}x\mathrm{d}y=\\
&\sum_q\sum_r\left(1-R\right)\zeta\xi_{qr}\int_{-a}^{a}\int_{-a}^{a}\psi_{mn}\left(x,y\right)\left\{\int_0^a\int_0^a G(x,x_0;y,y_0)\psi_{qr}\left(x_0,y_0\right)\mathrm{d}x_0\mathrm{d}y_0-\right.\\
&\left.\frac{I_G(x,y)}{1+\langle I_G\rangle_x}\int_0^a\int_0^a\langle G(x,x_0;a,y_0)\rangle_x\,\psi_{qr}\left(x_0,y_0\right)\mathrm{d}x_0\mathrm{d}y_0\right\}\mathrm{d}x\mathrm{d}y+\\
&\frac{Rp_{inc}F_{v_d}}{h_ph_gF_v}\int_{-a}^{a}\int_{-a}^{a}\psi_{mn}\left(x,y\right)\left\{\int_0^a\int_0^a G(x,x_0;y,y_0)\mathrm{d}x_0\mathrm{d}y_0-\right.\\
&\left.\frac{I_G(x,y)}{1+\langle I_G\rangle_x}\int_0^a\int_0^a\langle G(x,x_0;a,y_0)\rangle_x\,\mathrm{d}x_0\mathrm{d}y_0\right\}\mathrm{d}x\mathrm{d}y
\end{aligned}
\tag{3.46}
$$

The whole integral in (3.6) can be written in the following form

$$
\int_{-a}^{a}\int_{-a}^{a}\psi_{mn}\left(x,y\right)\left[p_g(x,y)-p_{inc}\right]\mathrm{d}x\mathrm{d}y=\sum_q\sum_r\xi_{qr}a_{mnqr}+c_{mn},
\tag{3.47}
$$

where

$$
\begin{aligned}
a_{mnqr}=&\left(1-R\right)\zeta\int_{-a}^{a}\int_{-a}^{a}\psi_{mn}\left(x,y\right)\left\{\int_0^a\int_0^a G(x,x_0;y,y_0)\psi_{qr}(x_0,y_0)\mathrm{d}x_0\mathrm{d}y_0\right.\\
&\left.-\frac{I_G(x,y)}{1+\langle I_G(x,a)\rangle_x}\int_0^a\int_0^a\langle G(x,x_0;a,y_0)\rangle_x\,\psi_{qr}\left(x_0,y_0\right)\mathrm{d}x_0\mathrm{d}y_0\right\}\mathrm{d}x\mathrm{d}y,
\end{aligned}
\tag{3.48}
$$

and

$$\begin{aligned} c_{mn} = &- p_{inc} \int_{-a}^{a} \int_{-a}^{a} \psi_{mn}(x,y) \mathrm{d}x \mathrm{d}y + \\ &\frac{R p_{inc} F_{v_d}}{h_p h_g F_v} \int_{-a}^{a} \int_{-a}^{a} \psi_{mn}(x,y) \left\{ \int_0^a \int_0^a G(x,x_0;y;y_0)\, \mathrm{d}x_0 \mathrm{d}y_0 \right. \\ &\left. - \frac{I_G(x,y)}{1 + \langle I_G(x,a) \rangle_x} \int_0^a \int_0^a \langle G(x,x_0;a,y_0) \rangle_x \, \mathrm{d}x_0 \mathrm{d}y_0 \right\} \mathrm{d}x \mathrm{d}y. \end{aligned} \tag{3.49}$$

The expression for the modal coefficients (3.6) then becomes

$$D\left[(k_{xm}^2 + k_{yn}^2)^2 - k_p^2\right] \xi_{mn} = \sum_q \sum_r \xi_{qr} a_{mnqr} + c_{mn}, \tag{3.50}$$

which can be written in matrix form

$$\left[-\mathbb{A} + \mathbb{B}\right](\Xi) = (C), \tag{3.51}$$

where $\mathbb{A}$ is the square matrix of elements $a_{mnqr}$, $\mathbb{B}$ is a diagonal matrix of elements $D\left[\left(k_{xm}^2 + k_{yn}^2\right)^2 - k_p^4\right]$, $k_{xm}, k_{yn}$ are given by the numerically calculated eigenfrequencies, eqs. (3.9), $(\Xi)$ and $(C)$ are respectively the column vectors of elements $\xi_{mn}$ and $c_{mn}$.

Figures 3.20-3.23 show the frequency dependence of the sensitivity of the transducer calculated using the present approach and compared to the numerical (FEM) result. Good agreement between these two results can be observed in the frequency range of interest, except at the very low frequencies, where the discrepancy is likely due to the lack of precision of the numerical integration when calculating the elements of the matrix $\mathbb{A}$ (the pressure differences on both sides of the plate being very low at low frequencies, the accuracy of the numerical integration becomes more important).

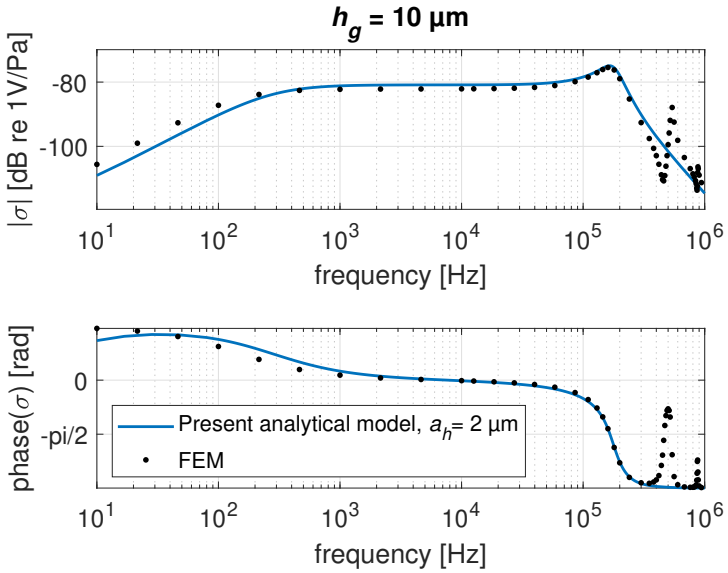


Figure 3.20: A comparison between the sensitivity of a MEMS transducer with a perforated plate: the present model (full line), the module and the phase of the sensitivity with a perforated cell 2 $\mu m$ regarding the selected gap thicknesses.

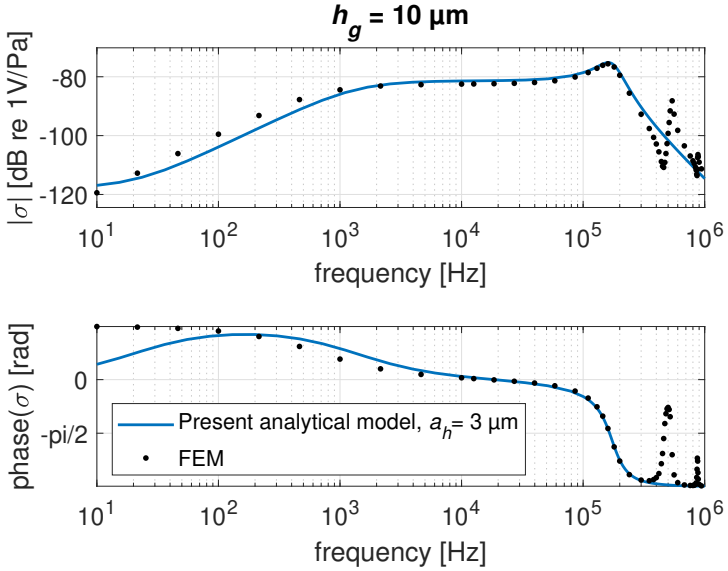


Figure 3.21: A comparison between the sensitivity of a MEMS transducer with a perforated plate: the present model (full line), the module and the phase of the sensitivity with a perforated cell 3 $\mu m$ regarding the selected gap thicknesses.

Moreover, observing Fig. 3.24, which depicts the difference in the acoustic pressure on both sides of the plate in relation to the different cutout sizes (from 2 $\mu$ m to 7 $\mu$ m), it is clear that there is a direct correlation between the size of the holes and the numerical

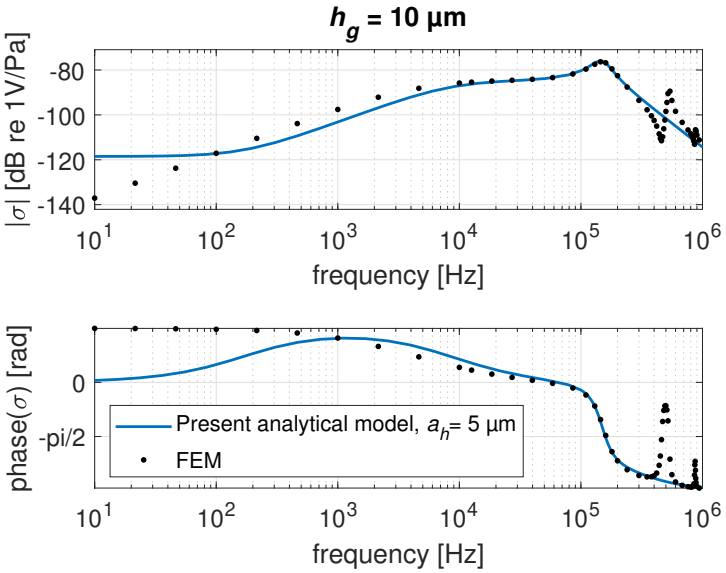


Figure 3.22: A comparison between the sensitivity of a MEMS transducer with a perforated plate: the present model (full line), the module and the phase of the sensitivity with a perforated cell 5 $\mu m$ regarding the selected gap thicknesses.

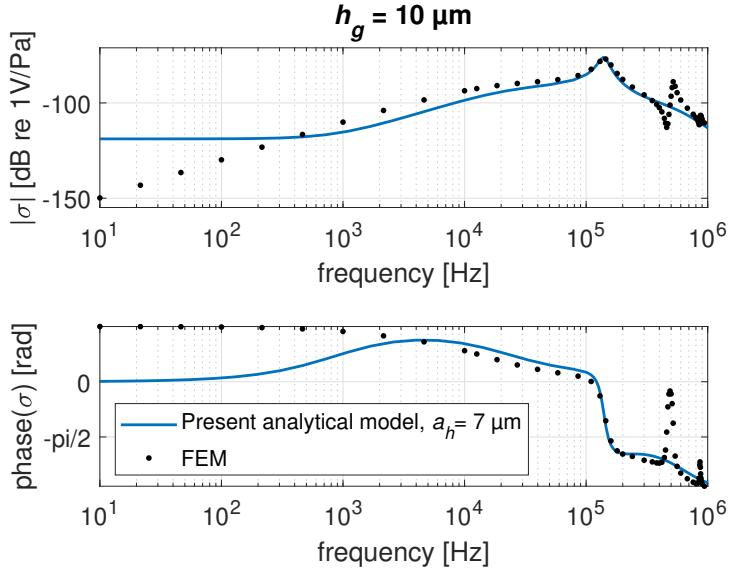


Figure 3.23: A comparison between the sensitivity of a MEMS transducer with a perforated plate: the present model (full line), the module and the phase of the sensitivity with a perforated cell 7 $\mu m$ regarding the selected gap thicknesses.

noise originating in the integrals as the microphone becomes more short-circuited with bigger perforation at low frequencies. An examination of Fig. 3.20-3.23, which depicts the discrepancies in relation to the size of the cutouts, further confirms this assumption.

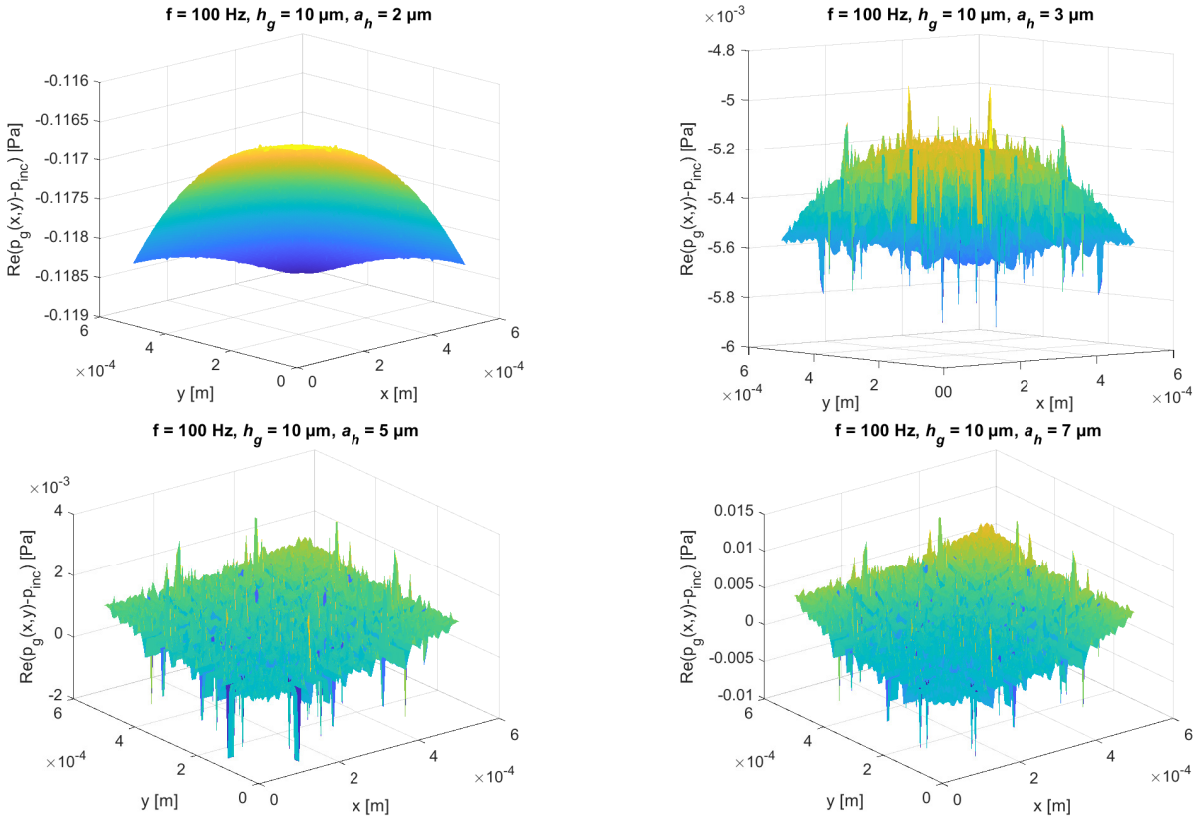


Figure 3.24: The real part of the difference of the acoustic pressure on both sides of the plate in the $1^{st}$ quadrant $(x, y \in (0; a\rangle)$ for a perforated cell a) 2 $\mu m$, b) 3 $\mu m$, c) 5 $\mu m$ and d) 7 $\mu m$, respectively.

As regards the thickness of the fluid gap between the moving electrode and the backplate in relation to perforation cell size, the following findings can be noted: The plate with 1 $\mu m$ cell size exhibits a well-known change in sensitivity, i.e. gap thickness doubling results in a 6 dB decrease in sensitivity (Fig. 3.25). As the cutouts become bigger, this effect is less and less prominent (Fig.3.26-3.28), forcing the sensitivity curve to demonstrate more linear-like behaviour at low frequencies.

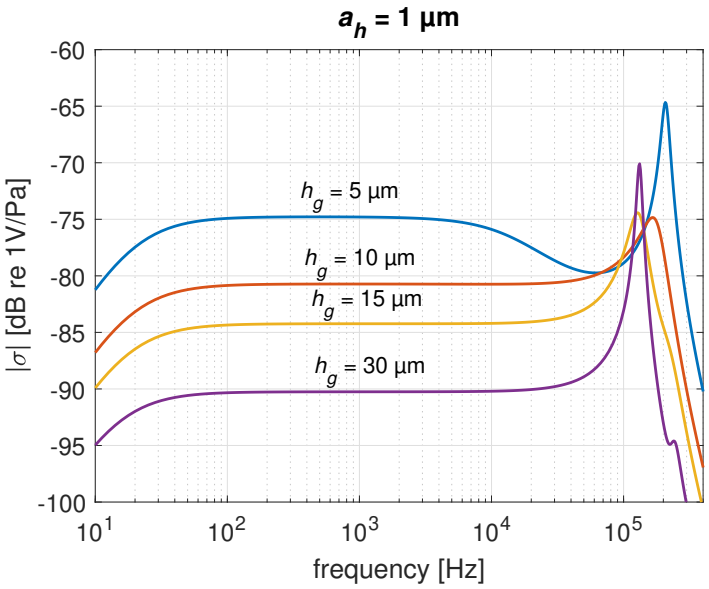


Figure 3.25: A comparison between the sensitivity of the MEMS transducer with a perforated plate: the module of the sensitivity, the perforated cell being 1 $\mu m$ with different thicknesses of the gap $h_g$.

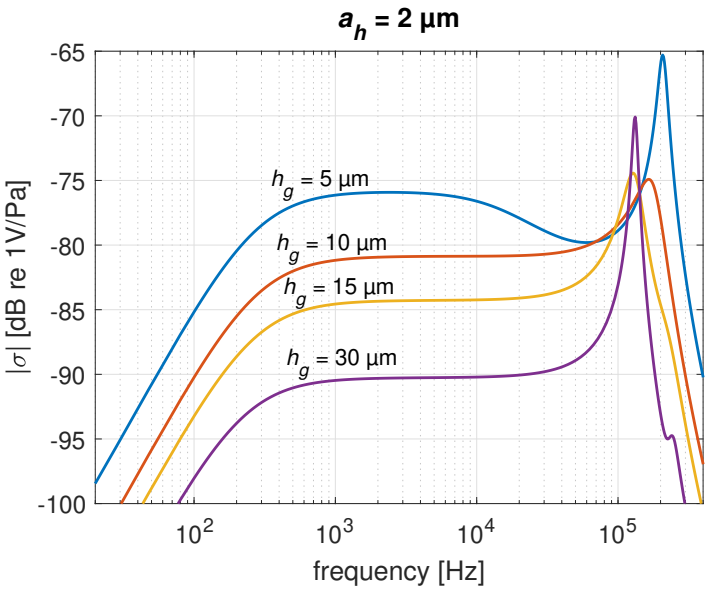


Figure 3.26: A comparison between the sensitivity of the MEMS transducer with a perforated plate: the module of the sensitivity, the perforated cell being 2 $\mu m$ with different thicknesses of the gap $h_g$.

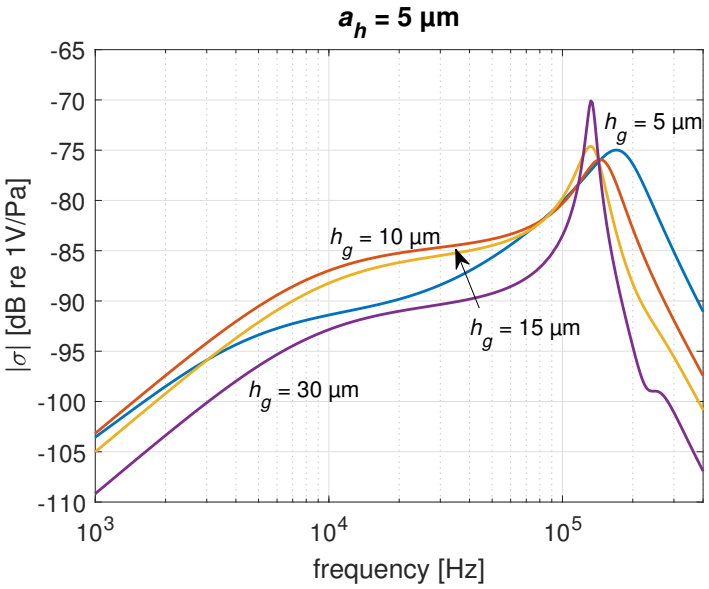


Figure 3.27: A comparison between the sensitivity of the MEMS transducer with a perforated plate: the module of the sensitivity, the perforated cell being 5 $\mu m$ with different thicknesses of the gap $h_g$.

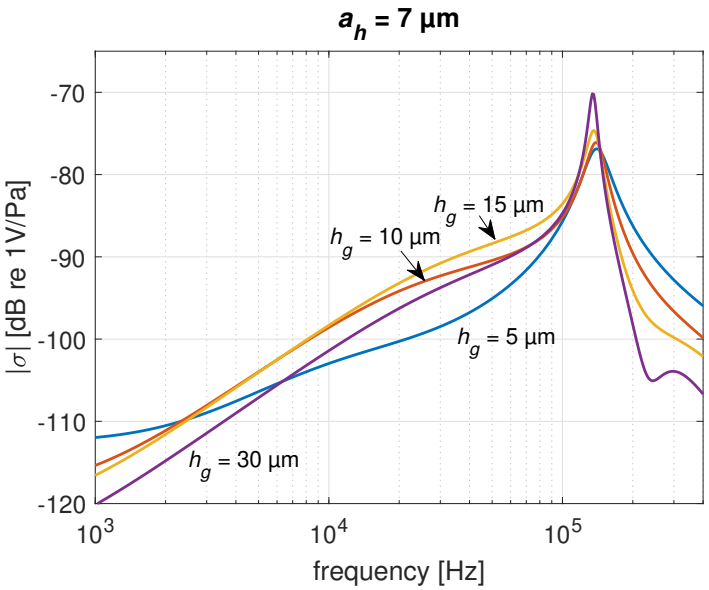


Figure 3.28: A comparison between the sensitivity of the MEMS transducer with a perforated plate: the module of the sensitivity, the perforated cell being 7 $\mu m$ with different thicknesses of the gap $h_g$.

# Chapter 4

# The measurements and an analysis on the noise sensor prototypes

This chapter deals with the experimental studies performed on two noise sensor prototypes developed by the Laboratory of Special Projects UBTI FD CTU in Prague. The work on electronic circuits design, the programming of the microcontrollers and the overall mechanical concept was carried out by the staff of the Laboratory of Special Projects UBTI FD CTU in Prague and is not the subject of this thesis. The electric schematics of both prototypes can be found in Appendix B and C. All the measurements and analysis presented here have been performed in order to improve the design process, and to confirm that the versions of the noise sensor perform appropriately.

## 4.1 The spectrum of traffic noise

Measurements of mean traffic noise with four hours averaging at a measurement site located near a roundabout (measurement GPS position 50.085607, 14.594737) within single working day (approx. from 8 AM till 12 AM) were carried out using 1/2″ microphone B&K 4189 and dynamic signal analyzer B&K Photon+. The 1/3 octave analysis of the recorded noise is shown in Fig. 4.1, presenting an approximately flat spectrum up to 1kHz and a -40 dB/dec slope above 1kHz. The Figure 4.2 shows the spectrum of the same traffic noise suffering from relatively low frequency resolution at low frequencies, but confirming the -40 dB/dec slope above 1kHz. The signal that was used for the experimental measurements was configured to mimick this spectrum at the measurement site (Fig.4.1), meaning that the spectrum of the signal (low-pass filtered white noise) is and should be almost flat from 10 Hz to 1 kHz with the fluctuation being almost ± 5dB, from 1 kHz to 20 kHz the signal drops by -40 dB/dec (-12 dB/oct).

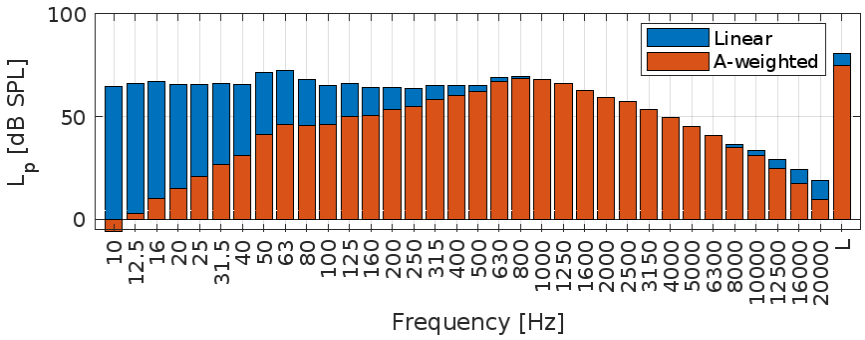


Figure 4.1: The traffic noise 1/3 octave analysis measured at the measurement site.

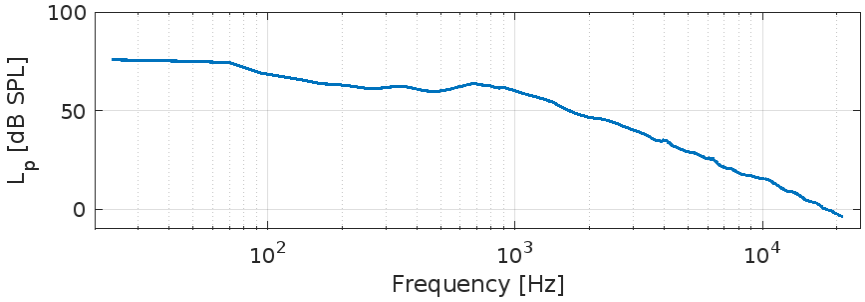


Figure 4.2: The traffic noise spectrum.

## 4.2 Earlier noise sensor prototype

Aiming to provide high bandwidth information about the urban sound environment and to explore forways to extract useful information and knowledge from the measurements, which can be labelled as big data, the Laboratory for Special Projects UBTI FD CTU in Prague developed a low-cost prototype sound sensor capable of making continuous measurements of noise levels.

This sound sensor consists of a measurement microphone, an analog path (containing a preamplifier, an A-filter and an antialiasing filter) and a processor (Fig. 4.3). The overall noise sensor scheme is given in Appendix B. In connection with electro-acoustic systems, which sensors essentially are, we touch on the quality of the electro-acoustic devices, which is closely related to the quality of their individual parts, especially the quality of the weakest element in the electroacoustic chain: i.e. the microphone.

### 4.2.1 Description of an electret microphone

The sound sensor prototype has an MCE 2500 electret microphone (Fig. 4.4) because of the requirement for a high number of sensor nodes. This raises the need to implement low-cost solutions, small dimensions, a relatively large frequency response and reasonable sensitivity. Moreover, there is no need for external polarization voltage in this type of microphone, which is a practical advantage compared to the classical condenser microphones. This

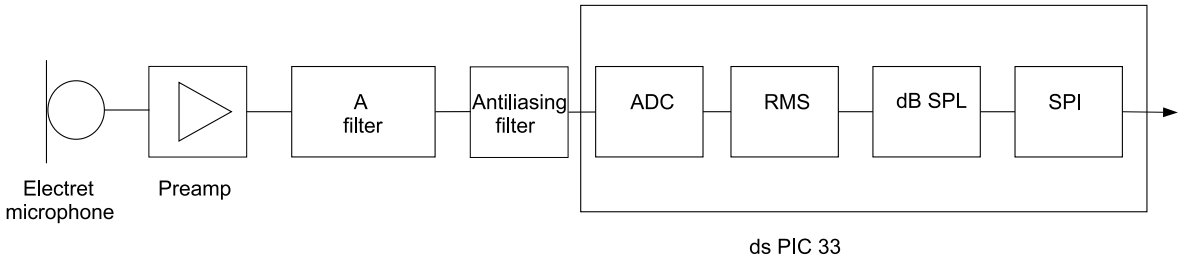


Figure 4.3: Noise sensor block diagram.

microphone consists of a circular membrane of radius $R_m$, a circular backplate separated from the membrane by a thin air gap of thickness $h_g$, and contains three holes of radius $R_h$ regularly azimuthally distributed at distance of $h$ from the border of the electrode, which are opened into a back cavity of volume $V$. The aluminium housing of the microphone contains a small opening of radius $R_{in}$ for acoustic access to a diaphragm. These parameters are summarized in Table 4.1.

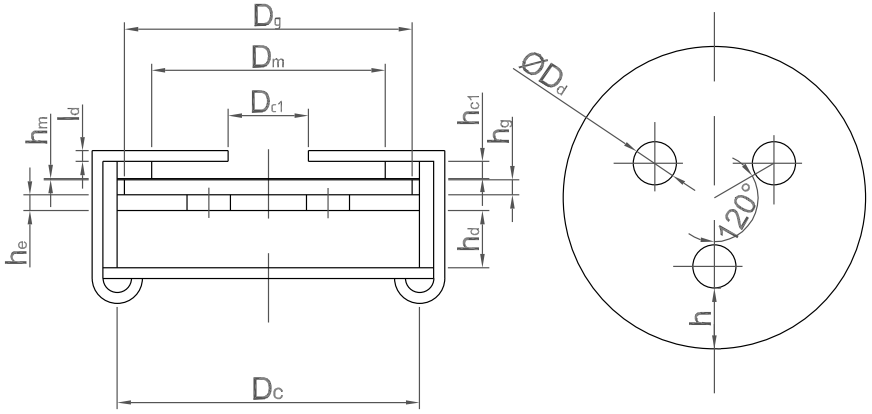


Figure 4.4: A cross-section view of the electret microphone and a top view of the backplate with holes.

The usual value of the density of the membrane material (mylar) of $\rho_m = 1380$ kg/m$^3$ is used in the calculations hereafter, because of the high uncertainty of the measurements of the mass and volume of such small samples.

### 4.2.2 Measurements on the noise sensor

The frequency response of several microphone samples was measured using the experimental setup shown in Fig. 4.5. From the results shown in Figure 4.6, it appears, that the pressure sensitivity values of the measured microphone samples differ in a relatively wide range (from 3.8 mV/Pa to 16.4 mV/Pa, which represents at range of 12.7 dB). However, the position of the first resonance of the whole system, which determines bandwidth of the

Table 4.1: Dimensional parameters of the microphone.

| Parameter | Symbol | Value |
|---|---|---|
| Diaphragm radius | $R_m = D_m/2$ | $1.975 \cdot 10^{-3}\ m$ |
| Diaphragm thickness | $h_m$ | $18 \cdot 10^{-6}\ m$ |
| Air gap thickness | $h_g$ | $29.75 \cdot 10^{-6}\ m$ |
| Air gap radius | $R_g = D_g/2$ | $1.975 \cdot 10^{-3}\ m$ |
| Radius of the hole in the backplate | $R_d = D_d/2$ | $0.395 \cdot 10^{-3}\ m$ |
| Cavity radius | $R_c = D_c/2$ | $2.14 \cdot 10^{-3}\ m$ |
| Opening radius | $R_{c_1} = D_{c_1}/2$ | $0.735 \cdot 10^{-3}\ m$ |
| Edge distances to hole | $h$ | $1.12 \cdot 10^{-3}\ m$ |
| Electrode thickness | $h_e$ | $0.29 \cdot 10^{-3}\ m$ |
| Opening length | $l_d$ | $0.20 \cdot 10^{-3}\ m$ |
| Input cavity thickness | $h_{c_1}$ | $313 \cdot 10^{-6}\ m$ |
| Back cavity thickness | $h_d$ | $1.2 \cdot 10^{-3}\ m$ |
| Cavity volume | $V_c$ | $1.856 \cdot 10^{-8}\ m^3$ |

microphone, seems to be similar for all measured samples of the microphone (around 10 kHz).

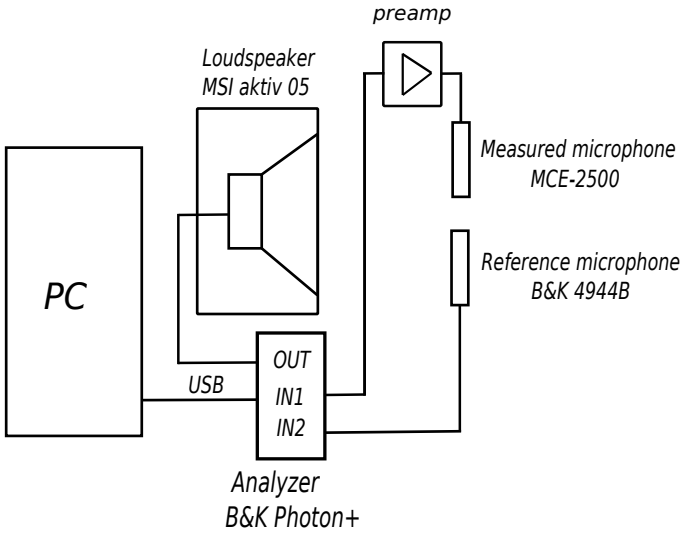


Figure 4.5: Experimental setup for measurements of the sensitivity of the microphone.

The acoustic pressure sensitivities at 1kHz in dB and in mV/Pa are summarized in Table 4.2. The last column of this table presents the height of the sensitivity peak, calculated as the difference between the sensitivity at 1 kHz and at the peak of the sensitivity curve in dB, giving an idea about the damping in the system.

In order to explore the behaviour of the whole electroacoustic chain in the noise sensors, the normalized transfer functions of the electroacoustic path from the microphone input to the output of the antialiasing filter were measured on several noise sensor samples. Figure

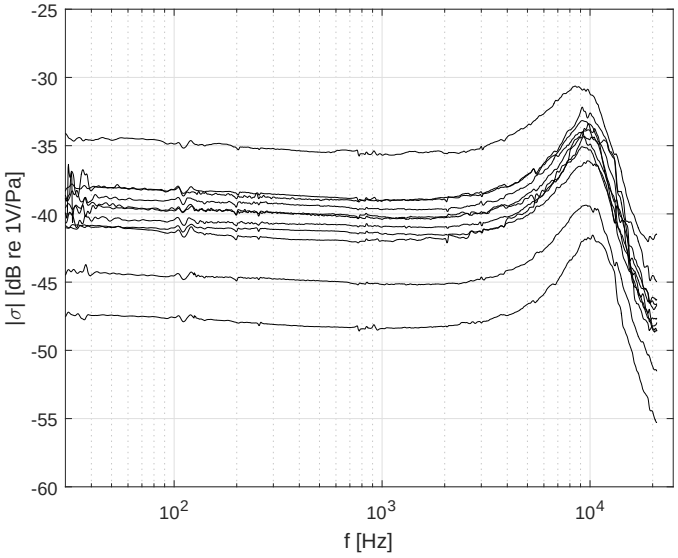


Figure 4.6: The measured pressure sensitivities of MCE 2500 microphones.

Table 4.2: The measured pressure sensitivities and the heights of the resonance peaks.

| $No.$ | $\sigma_{1kHz}[dB]$ | $mV/Pa$ | $\Delta\ dB$ |
|---|---|---|---|
| 1 | $-35.6$ | 16.4 | 5.0 |
| 2 | $-39.0$ | 11.1 | 6.8 |
| 3 | $-40.9$ | 8.9 | 5.8 |
| 4 | $-41.4$ | 8.4 | 5.3 |
| 5 | $-40.3$ | 9.5 | 6.4 |
| 6 | $-41.9$ | 7.9 | 8.5 |
| 7 | $-39.0$ | 11.2 | 5.8 |
| 8 | $-40.2$ | 9.7 | 5.8 |
| 9 | $-45.1$ | 5.5 | 5.8 |
| 10 | $-48.3$ | 3.8 | 6.8 |
| 11 | $-39.6$ | 10.3 | 5.8 |

4.7 depicts an example of such a transfer function for one sample (red curve) in comparison with the transfer function of the A-filter given by the norm [41] (blue curve). For better clarity, the Figure 4.8 shows the differences of the measured transfer functions of selected samples from the transfer function of the A-filter given by the norm.

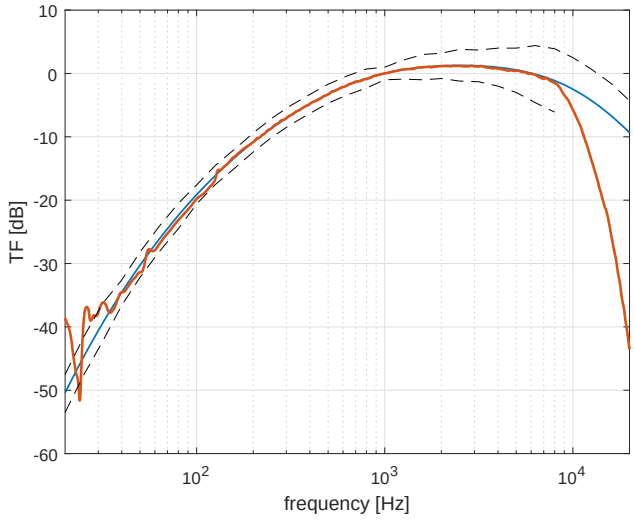


Figure 4.7: Transfer function of the electroacoustic path of the sensor (red curve) in comparison with the transfer function of the A-filter given by the norm [41] (blue curve).

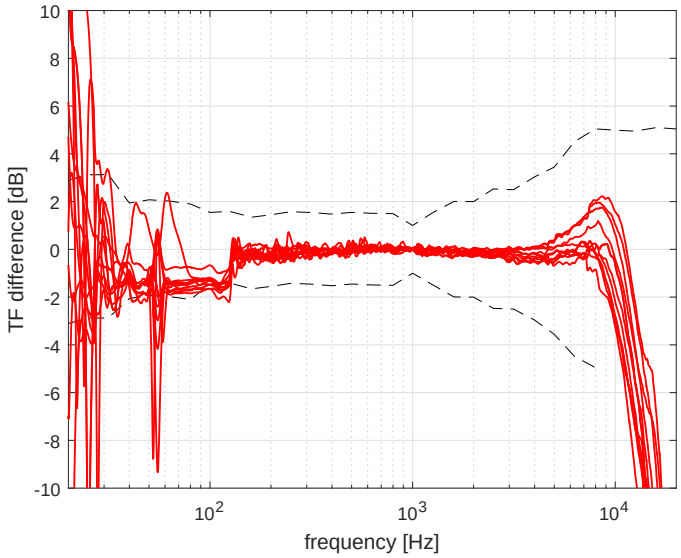


Figure 4.8: Difference between the measured transfer functions from the A-filter (continuous lines) and the class II tolerance limits (dashed lines).

It seems that the analog path of the measured noise sensor samples results in a category II rating (limits given by black dashed lines in Fig. 4.8, 4.7) in the major part of the frequency range of interest. At very low frequencies (below 60 Hz), the precision of the measurement is affected by a low signal-to-noise ratio, which leads to invalid measurement results.

In the following sections, the lumped element model of the microphone will be presented and a set of measurements of its parameters will be described in order to explain the differences in microphone sensitivities.

### 4.2.3 The lumped element model

The classical lumped-element model [37, 40, 29] of the microphone (with some particularities described in this section) is considered in this section. The equivalent circuit shown in Figure 4.9 consists of acoustic, mechanical and electric parts.

The link between the acoustic and mechanical domain is modelled by the mechano-acoustic transformer with a ratio of $1 : S_m$ at the input of the model, $S_m = \pi R_m^2$ representing the diaphragm area, and $p_{inc}$ is the incident acoustic pressure. The second transformer represents the coupling between the electric and mechanical domain with a ratio of $1 : k_b$, where $k_b = \frac{C_0 U_0}{h_g}$ is the transducer factor, $C_0 = \frac{\varepsilon_0 S_m}{h_g}$ being the static capacitance of the microphone (the effect of the holes in the back electrode on the microphone static capacitance is neglected because of their small dimensions, along with the edge effect of the electrostatic field near the holes). Since the transducer is assumed to operate with constant charge, the negative compliance $-c_n = -C_0/k_b^2$ (which should theoretically be present in the equivalent circuit) can be neglected [37]. The mechanical domain between the two transformers mentioned above consists of the components representing the membrane and the air-filled acoustic elements behind the membrane (transformed to the mechanical domain).

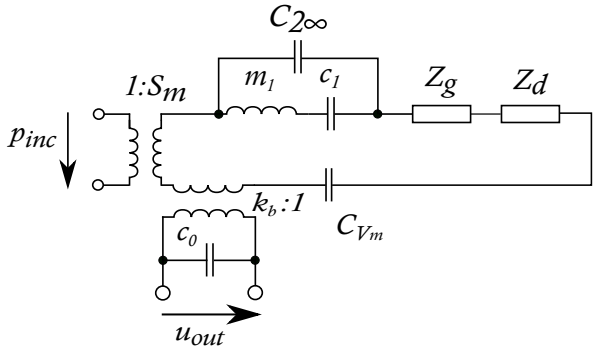


Figure 4.9: Complete equivalent circuit of the microphone.

The mechanical impedance of the air gap between the membrane and the backplate with holes of radius $R_d$ can be calculated as follows [37]

$$Z_g = N\left(\frac{6\mu\pi X_0^4\beta}{h_g^3} + j\omega\frac{\rho_0\pi X_0^4\beta}{2h_g}\right), \tag{4.1}$$

$N$ is the number of holes in the backplate, in this case $N = 3$, $X_0 = \sqrt{S_m/(N\pi)}$ is an equivalent circular region collecting the air flow from each hole and $\beta = \ln\frac{X_0}{R_d} - \frac{3}{4} + \frac{R_d^2}{X_0} - \frac{1}{2}\frac{R_d^4}{X_0^4}$.

The holes are modelled by the mechanical impedance

$$\begin{aligned} Z_d = &\frac{S_m^2}{N}\left[\frac{8h_e\mu}{\pi R_d^4} + j\omega\frac{4\rho_0 h_e}{3\pi R_d^2} + \right. \\ &\left. +2j\omega\frac{\rho_0}{X_0}\left(0.26164 - 0.353\alpha + 0.0809\alpha^3\right)\right], \end{aligned} \tag{4.2}$$

where the first two terms in the bracket represent the resistance and the mass of the holes [37] and the third term with $\alpha = R_d/X_0$ ($R_d$ is the radius of the holes) is the added mass modelling the influence of the sharp edges of the holes [42].

The membrane behavior is described by the components [37]

$$\begin{aligned} c_1 &= \frac{4}{j_1^4\pi T}, \\ m_1 &= \frac{j_1^2}{4} m_s S_m, \\ C_{2\infty} &= C_\infty - c_1, \end{aligned} \tag{4.3}$$

where the mechanical compliance $c_1$ and the mass $m_1$ determine the first membrane eigenfrequency, $C_\infty = \frac{1}{8\pi T}$ is the quasistatic compliance of the membrane, and $C_{2\infty}$ provides a correction of the low-frequency behavior.

The comparison between the results obtained from the equivalent circuit and from the numerical (FEM) model is shown in Figure 4.10, the parameters of the air being given in Table 4.3 and the dimensions of the microphone being given in Table 4.1, $T = 100$ N/m and $U_0 = 100$ V. Good agreement can be observed between the theoretical results obtained from the lumped element model with the estimated parameters and the FEM results.

Table 4.3: Parameters of the air.

| Parameter | Symbol | Value | Unit |
|---|---|---|---|
| Adiabatic sound speed | $c$ | 345.9 | $[m \cdot s^{-1}]$ |
| Air density | $\rho_0$ | 1.18 | $[kg \cdot m^{-3}]$ |
| Shear dynamic viscosity | $\mu$ | $1.83 \cdot 10^{-5}$ | $[Pa \cdot s]$ |
| Permittivity | $\varepsilon_0$ | $8.8542 \cdot 10^{-12}$ | $[F \cdot m^{-1}]$ |
| Thermal conductivity | $\lambda_h$ | $24.4 \cdot 10^{-3}$ | $[W/(m \cdot K)]$ |
| Specific heat coefficient at constant pressure per unit of mass | $C_p$ | 1010 | $[J/(kg \cdot K)]$ |
| Ratio of specific heats | $\gamma$ | 1.4 | $[-]$ |
| Static pressure | $P_0$ | 101.325 | $[Pa]$ |
| Static temperature | $T_0$ | 293.15 | $[K]$ |

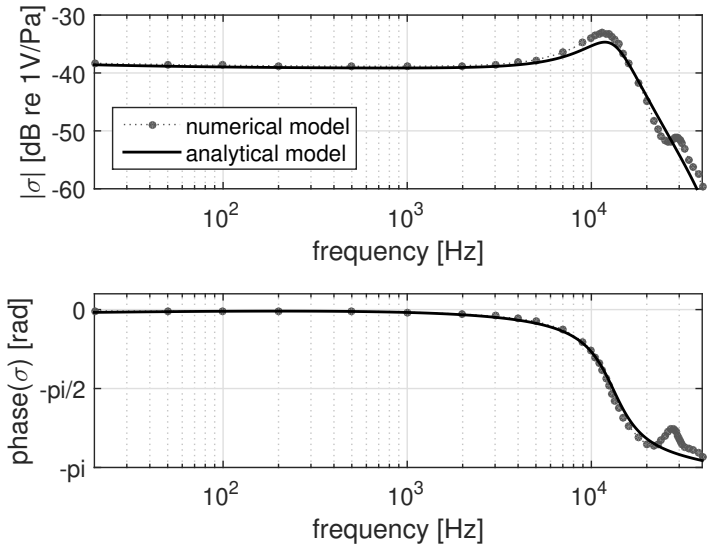


Figure 4.10: The magnitude and the phase of the pressure sensitivity of the transducer calculated using the lumped element model and the reference numerical (FEM) solution.

### 4.2.4 Measurements on low-cost electret microphones [A.3]

Most of the parameters of such a model can usually be determined from directly measured dimensions of the system and from the material parameters. The accuracy of the model can then be verified by measurements such as laser vibrometry [16, 43] and electrostatic excitation [16, 45, 46, 47] of the membrane movement. However, two parameters, the tension of the membrane and the equivalent polarization voltage produced by the electret layer, cannot be measured directly.

The influence of the membrane tension, the equivalent polarization voltage and the air gap thickness on the changes in sensitivity between the measured samples was observed.

The mechanical tension of the membrane was measured using the electrostatic method [45] in vacuum (measurement setup in Figure 4.11). The tension of the membrane can be calculated from the measured frequency of the first mode of the membrane. In order to eliminate the impact of all acoustical elements except the membrane, the measurement of the resonance frequency has to be performed in a vacuum chamber. The well-known method using the electrostatic grid to excite the motion of the membrane is applied in the present study.

Unlike classical condenser microphones, the electret microphone considered here has no direct access to the membrane. The classical electrostatic grid [16, 45] therefore cannot be used. For this reason, a special electrostatic grid was fabricated.

Since the eigenfrequencies $f_n$ ($n = 1, 2, \dots$) of the membrane modes *in vacuo* are given by the equation $J_0(2\pi f_n/\sqrt{T/m_s}) = 0$ [37, 29], $m_s = \rho_m h_m$ being the surface density of the membrane, $J_0(x)$ being the 0-th order Bessel function of the first kind, the tension $T$

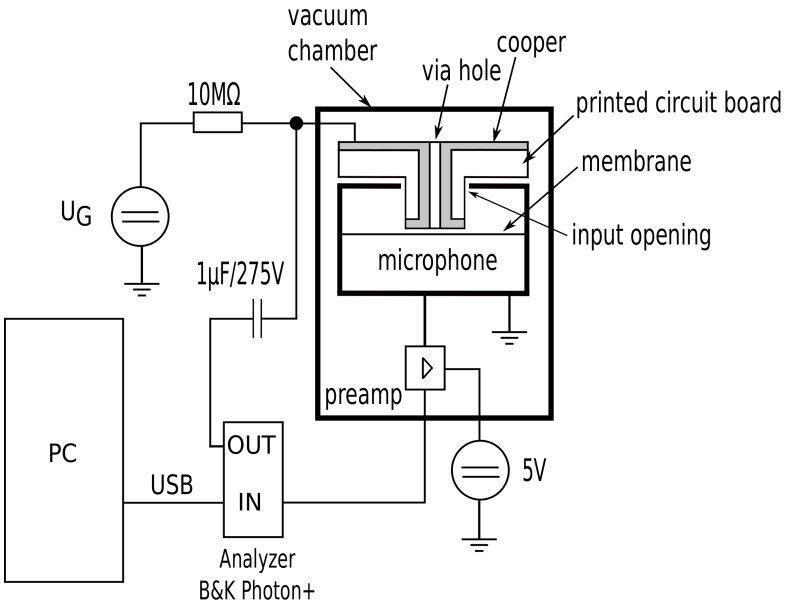


Figure 4.11: Measurement setup for the measurement in the vacuum.

of the membrane can be calculated from the measured first eigenfrequency $f_{res} = f_1$, as follows

$$T = m_s \left( \frac{2\pi f_{res} R_m}{j_1} \right)^2, \tag{4.4}$$

where $j_1 \approx 2.4048$ is the first solution of the equation $J_0(j_n) = 0$.

The measured membrane tensions $T$ (Table 4.4) present certain variations among the measured microphone samples, resulting in the variation of the pressure sensitivities of the microphones, namely the measured eigenfrequencies of the membranes range from 11.595 kHz to 12.364 kHz, which leads to the tensions of the membranes ranging from 88.9 N/m to 101.1 N/m.

The adimensional sensitivities [19] calculated using the lumped-element model with the measured membrane tensions used as model inputs are calculated here, the other parameters of the model being fixed. Table 4.5 presents the adimensional sensitivities at 1 kHz for the maximal and minimal membrane tension, showing that the variation of the measured tensions (from 88.9 N/m to 101.1 N/m) cannot cause such a huge variation of acoustic pressure sensitivities measured in Table 4.2 (12.7 dB). The modelled sensitivities here are in the range of 1.3 dB.

As for the air gap thickness $h_g$, the change of $h_g$ from 30 $\mu m$ to 35 $\mu m$ (the membrane tension being $T = 100$ N/m) causes the change in the height of the sensitivity peak, which is similar to the range of the measured variation, while the adimensional sensitivity at 1 kHz decreases only by 1.3 dB (Table 4.6). This shows that the measured variation of the acoustic pressure sensitivity of 12.7 dB, while the measured height of the sensitivity ranges from 5 dB to 8.5 dB, cannot be caused by a variation in the thickness of the airgap.

Table 4.4: The measured resonance frequencies and tensions.

| $No.$ | $P_0$ $[Pa]$ | $f_{res}$ $[kHz]$ | $T$ $[N/m]$ |
|---|---|---|---|
| 1 | 0.62 | 11.946 | 94.4 |
| 2 | 0.59 | 12.364 | 101.1 |
| 3 | 0.60 | 11.879 | 93.3 |
| 4 | 0.64 | 11.681 | 90.2 |
| 5 | 0.46 | 11.813 | 92.3 |
| 6 | 0.60 | 11.665 | 90.0 |
| 7 | 0.28 | 11.662 | 89.9 |
| 8 | 0.47 | 12.154 | 97.7 |
| 9 | 0.62 | 11.737 | 91.1 |
| 10 | 0.59 | 11.595 | 88.9 |
| 11 | 0.60 | 12.222 | 98.7 |

Table 4.5: Dependence of the adimensional sensitivity on the membrane tension calculated from the microphone model.

| $T$ $[N/m]$ | $\sigma_{adim}(1kHz)$ $[dB]$ |
|---|---|
| 101.1 | $-79.2$ |
| 88.9 | $-78.5$ |

Table 4.6: Dependence of the adimensional sensitivity and the height of the sensitivity peak on the gap thickness calculated from the microphone model.

| $h_g$ $[m]$ | $\Delta dB$ $[dB]$ | $\sigma_{adim}(1kHz)$ $[dB]$ |
|---|---|---|
| $30 \cdot 10^{-6}$ | 4.6 | $-79.2$ |
| $35 \cdot 10^{-6}$ | 8.2 | $-80.5$ |

The only model parameter, that remains and that needs to be examined is the equivalent polarization voltage $U_0$. This parameter was estimated from the measured pressure sensitivities, using a significantly simplified equivalent circuit (Fig.4.13). The impedance of the airgap and the holes in the backplate is much lower in terms of absolute value than the impedance of the membrane and the back cavity at low frequencies (more than 100 times at 100 Hz, Fig. 4.12), and can be neglected in order to form a low-frequency equivalent circuit. Furthermore, when omitting the mass of the membrane, the change in the value of the impedance at low frequencies is negligible. Note, that the effects of the thermal losses in the backing cavity cannot be neglected at very low frequencies. The complex equivalent volume (4.5) [29] should therefore be used here.

$$V_{cplx} = V_c \left( 1 + (1-j)(\gamma - 1) S_c \frac{\sqrt{c\frac{l_h}{\omega}}}{V_c \sqrt{2}} \right), \tag{4.5}$$

where $S_c = 2\pi R_m \cdot (R_m + h_d)$ is the surface of the cavity, $l_h = \lambda_h / (\rho_0 c C_p)$ is the characteristic

thermal length, and the other parameters of the fluid are given in Table 4.3.

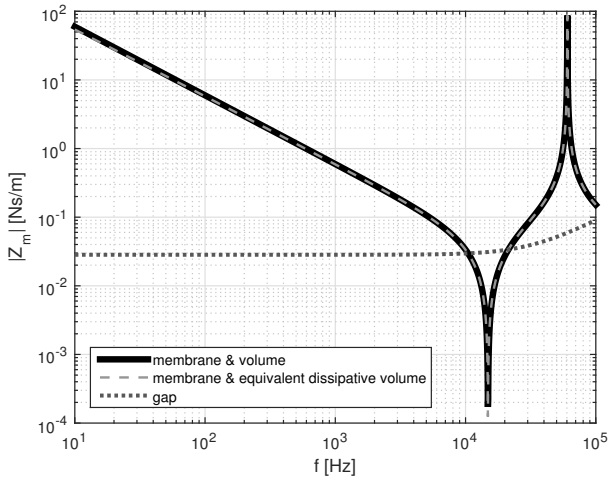


Figure 4.12: Mechanical impedances of parts of the complete equivalent circuit.

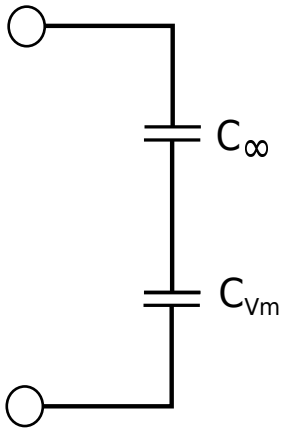


Figure 4.13: The low-frequency equivalent circuit.

Since the input impedance at low frequencies is given by the equivalent circuit from Figure 4.13 as $Z_m$, a rough estimate of the equivalent polarization voltage can be calculated from the value of the measured acoustic pressure sensitivity $\sigma_{meas}$ at low frequency (here 100 Hz) as follows

$$U_0 = \left| \frac{h_g \sigma_{meas}(100Hz)}{S_m(C_\infty + C_{Vm})} \right|. \tag{4.6}$$

The calculated estimates of the equivalent polarization voltages of all measured samples of the electret microphone are shown in Table 4.7.

Figure 4.14 shows comparison between the measured and the calculated acoustic pressure sensitivity of three microphone samples, one for the lowest sensitivity, one for the

Table 4.7: The estimated equivalent polarization voltages.

| No. | $U_0$ $[V]$ |
|---|---|
| 1 | 147.7 |
| 2 | 100.9 |
| 3 | 78.1 |
| 4 | 72.9 |
| 5 | 85.2 |
| 6 | 70.0 |
| 7 | 100.3 |
| 8 | 84.1 |
| 9 | 48.7 |
| 10 | 34.2 |
| 11 | 92.5 |

highest sensitivity, and one for the middle level. Good agreement can be observed between the theoretical results obtained from the full equivalent circuit (Figure 4.9), the estimated parameters and the measured sensitivity curves. The slight shift in the resonance frequency can be caused by the fact that the density of the membrane was not measured (the usual value was used). The damping of the system (according to the height of the resonance peak) seems to be predicted correctly for sample No. 1 and slightly overestimated for the other two samples shown in Figure 4.14, as in the case of the comparison between the lumped element model and the FEM results (see the previous subsection). Ultimately, the only key factor that affects the differences between sensitivities of the microphone samples is the equivalent polarization voltage $U_0$.

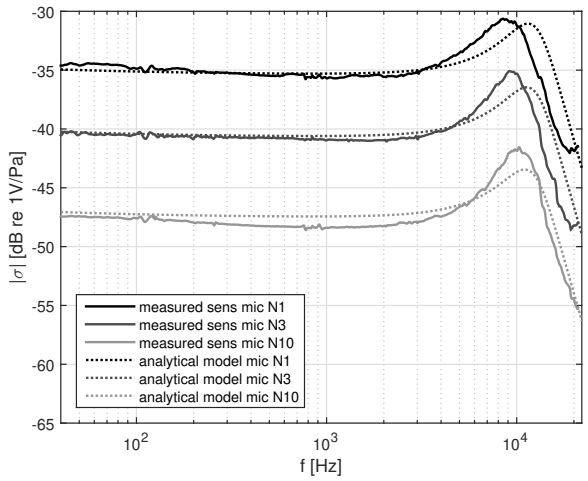


Figure 4.14: The measured and calculated acoustic pressure sensitivity of three microphone samples.

## 4.3 The present version of the noise sensor

The main issues with the previous sensor design(section 4.2 "Earlier noise sensor prototype") were some problems with the technology and with rational functioning (e.g. the sensitivity spread). This implies that the new prototype (introduced here) has superior hardware and software, such as fully digital communication between the MEMS microphone and the microcontroller and also the avoidance of the use of the electret microphone, which reduces the sensitivity spread in the components of the noise sensor. The present version of the noise sensor consists of the MEMS microphone ICS-43432 and microcontroller PIC 32 with 24.576 MHz input clocking (Figure 4.15). The whole detailed noise sensor scheme is given in Appendix C.

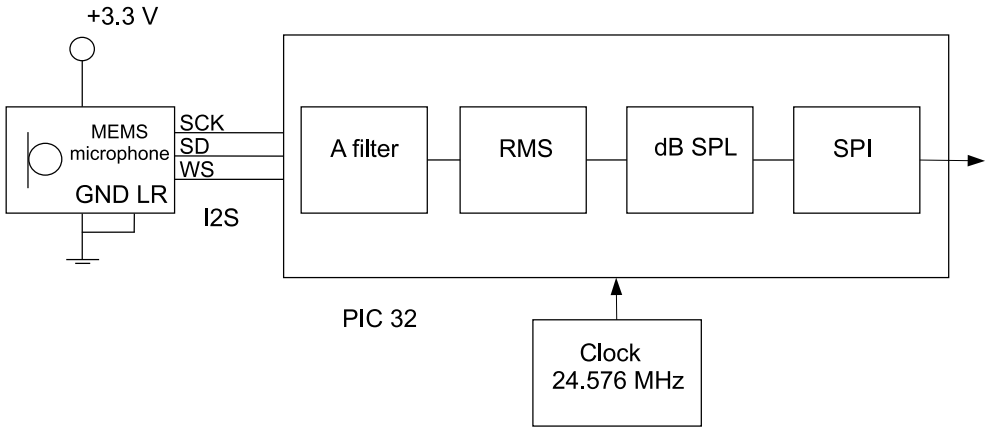


Figure 4.15: Noise sensor block diagram.

### 4.3.1 A description of the MEMS microphone

The ICS-43432 microphone that is used in the new version of the noise sensor, is a digital low-noise microphone with a I2S interface that allows the microphone to connect directly to the digital processors [44]. Some specifications found in the MEMS microphone data sheets [44], explaining the specifications and terms for the microphone to be appropriately integrated into a system, are as follows: a) the sensitivity uncertainty is ± 1 dB, which gives us a solid understanding of perhaps the most important microphone specification, b) the Equivalent Input Noise is 29 dB(A) SPL, c) the level of distortion on the output signal for a given pure tone input signal Total Harmonic Distortion is 0.3 % for 105 dB SPL. This information can help us to choose an appropriate type of microphone for specific applications, d) Acoustic Overload Point 116 dB SPL is the sound pressure level at which the THD of the output of the microphone equals 10%, and e) the supply current is 1.1-1.5 mA for 3.3V of supply voltage.

According to the datasheet mentioned above, microphones of this type also offer high linearity and a flat magnitude response from about 100 Hz to 10 kHz (Fig. 4.16).

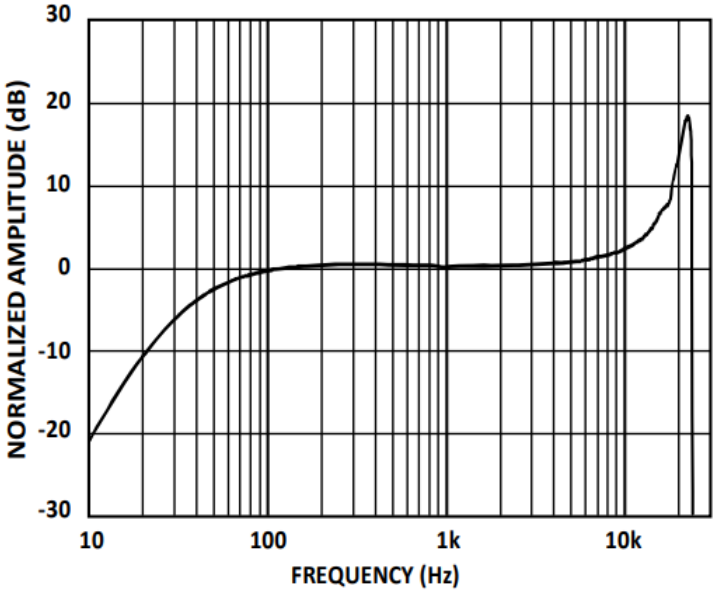


Figure 4.16: Typical frequency response. [44]

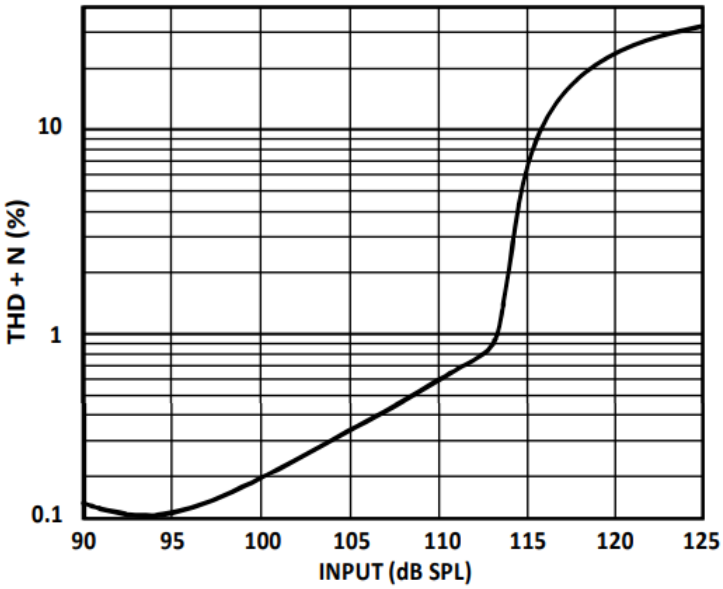


Figure 4.17: Total Harmonic Distortion + Noise (THD+N) vs. Input SPL. [44]

The THD increases rapidly starting at about 113 dB, and reaching a whopping 10% at 116 dB (Fig. 4.17).

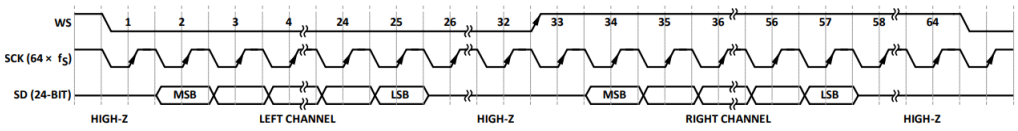


Figure 4.18: Time diagram output I2S. [44]

Fig. 4.18 shows the timing of the data driven by the microphone with respect to the clock and the word select signal generated by the master. The Block Diagram Fig. 4.19 shows the interconnection of the various pieces of equipment in a microphone system and the flow of the signal through the system. Note, that only the left side of both the stereo input and the system block diagram applies here, the system master being PIC 32. Since the sampling rate of the system is influenced by the I2S clock signal generated by the master, the stability of the sampling rate depends on the generator of the 24.576 MHz clock for the microcontroller (Fig. 4.15).

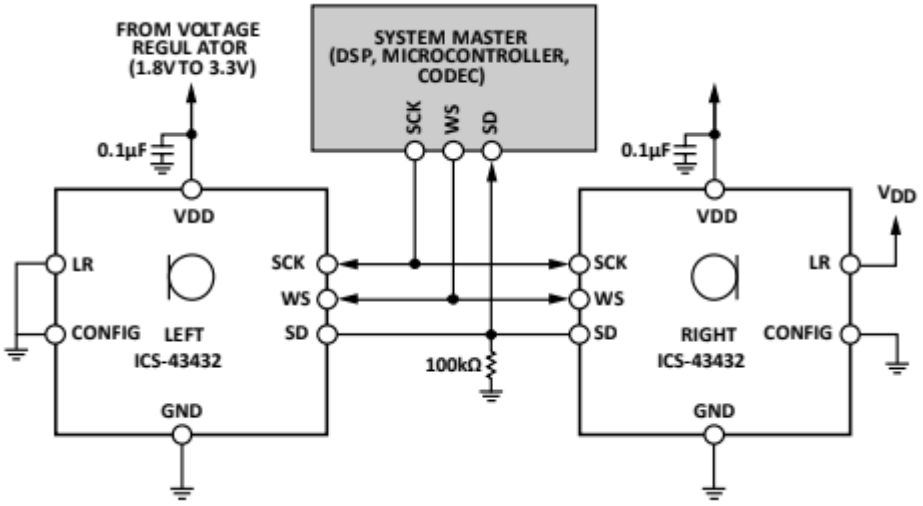


Figure 4.19: System block diagram. [44]

### 4.3.2 Measurements on the MEMS microphones

A set of measurement tests of the noise sensor components needs to be conducted to check if the whole sensor is properly configured and performs appropriately. The task follows the MEMS microphones measurements as it must be examined.

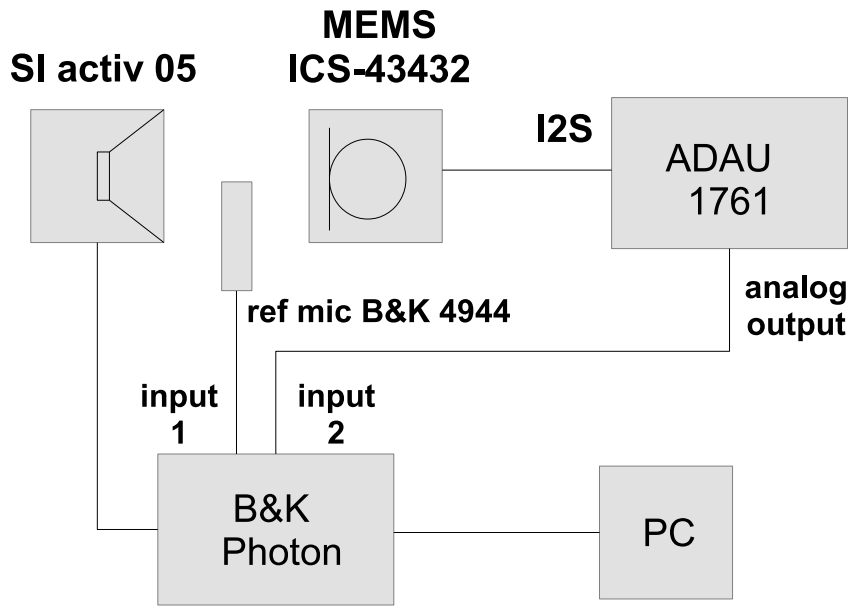


Figure 4.20: The measurement scheme.

The measurement setup (Fig.4.20) includes the B& K Photon+ dynamic signal analyzer, which drives the SI activ 05 loudspeaker with the reference 1/4" microphone B& K 4944 at the input. The measured ICS-43432 microphone is connected to the input of the analyzer through the ADAU 1761 audio codec to translate the digital signal to an analog signal. The measurement was carried out at about 94 dB(A), and the swept sine signal generated by the analyzer was used as the measurement signal.

It is also necessary to define the ranges that may be targeted. Since the sampling rate of the sensor is 32 kHz, and since the traffic noise is negligible at very high frequencies (section 4.1 "The spectrum of traffic noise"), the frequency range of interest in the measurement should be narrowed down to 16 kHz. This leads to fewer computational issues in processing than when more frequently-used sample rate of 48 kHz is used.

Fig. 4.21 depicts the different frequency responses (the magnitude of the transfer function) among all measured microphones (20 samples), where thick black curve of the sensitivity waveform represents the mean of all samples, with the exception of a single outlier.

Fig.4.22 shows the differences of the measured frequency responses from their mean. This seems to indicate that the sensitivity rating of most of the measured microphones is $\pm 1$ dB up to approximately 10 kHz (the one outlier may have been caused by some issues during the measurement). The discrepancies at the highest frequencies cause only negligible error in SPL measurements because of the frequency spectrum of transportation noise (section 4.1 "The spectrum of traffic noise").

Fig. 4.23 compares the normalized mean frequency responses measured at sample rates of 32 kHz (red curve) and 48 kHz (blue curve), showing the effects of the antialiasing filter cutoff frequency along the sensitivity peak of the microphone.

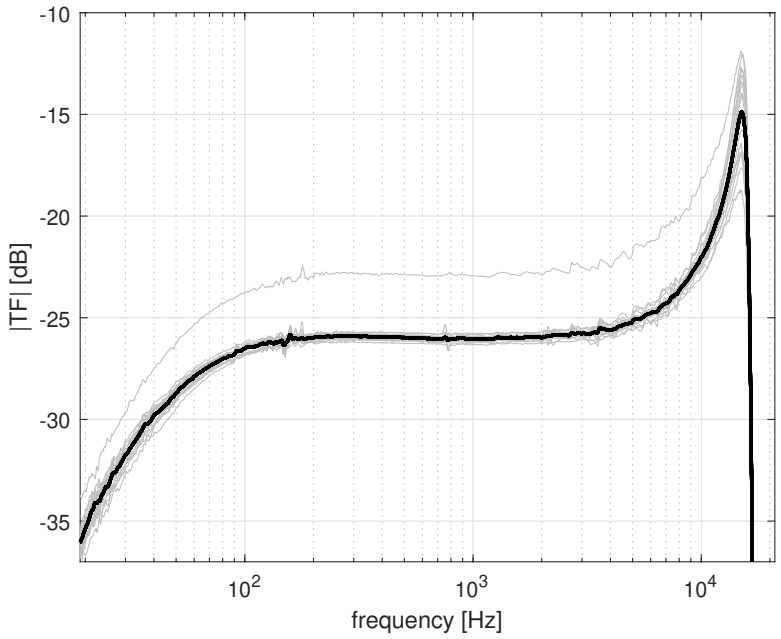


Figure 4.21: The measured frequency responses of the microphones (grey lines) and their mean (thick black curve).

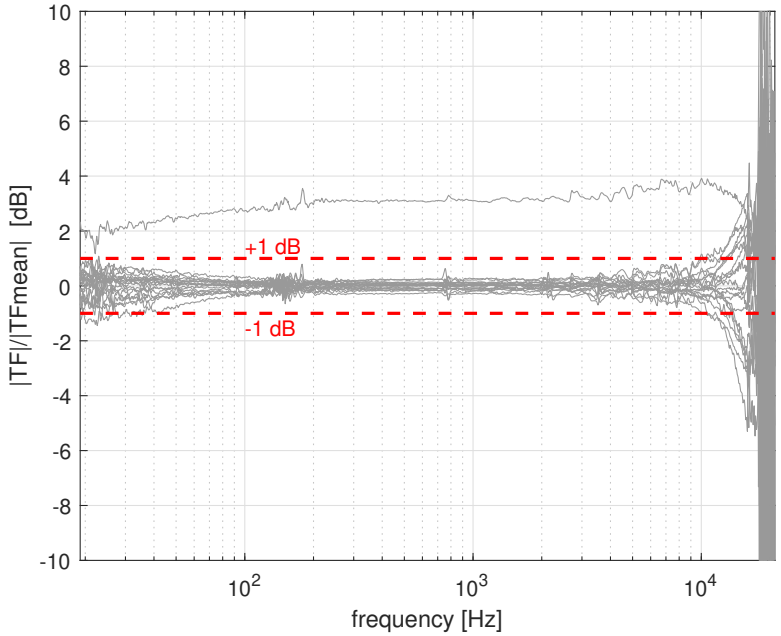


Figure 4.22: Differences of the measured frequency responses from the mean (detailed view).

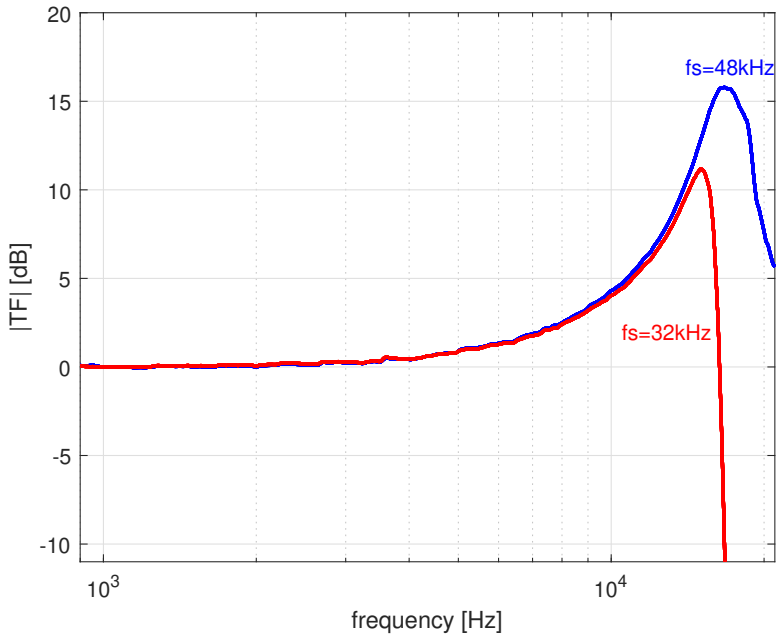


Figure 4.23: The normalized mean frequency responses of the microphones measured using sampling frequencies of 32kHz and 48kHz.

### 4.3.3 Measurements on the MEMS microphone + A-filter system

The A-filter is composed of three stages of filtering: two low-pass filters and one high-pass filter.

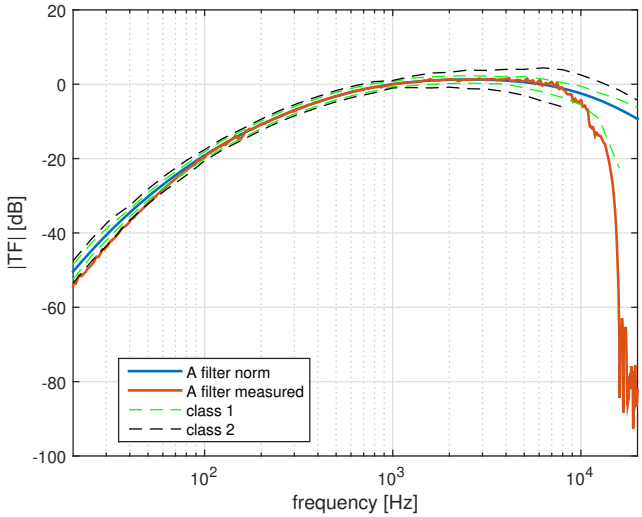


Figure 4.24: The transfer function of the MEMS microphone + A-filter containing two biquads (one biquad is removed, all coefficients of 2 others remained unchanged).

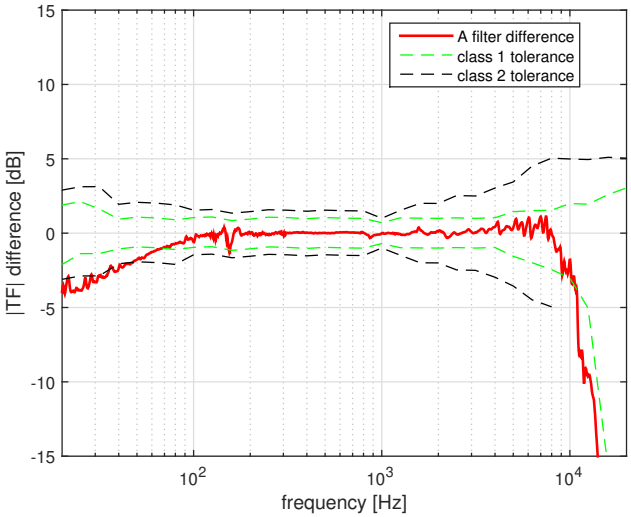


Figure 4.25: Difference between the measured transfer function and the transfer function given by the norm for the A-filter (one biquad is removed, all coefficients of 2 others remained unchanged).

One of the two high-pass filters (the filter with the lower cutoff frequency) was removed here, since the microphone itself acts as a high-pass filter; i.e. it allows high frequencies to pass while cutting out low frequencies, Fig. 4.21. First, the measurement was performed with all coefficients of the two remaining biquads (digitally implemented second order IIR filters) remaining, as they were designed using Matlab software (Fig. 4.24). The red curve in Fig. 4.24 shows the frequency response of the MEMS microphone + digital A-filter system compared to the norm [41] (blue curve) and the limits for class I (green dashed curve) and class II (black dashed curve). Discrepancies at low frequencies (below approximately 100 Hz) can be observed here. Hovewer, they are more visible in Fig. 4.24, which shows the difference between the measured frequency response and the norm.

| **Biquad coefficients** | **No.1** | **No.2** | **No.3** |
|---|---|---|---|
| $b_0$ | 1.0 | 1.0 | 1.0 |
| $b_1$ | 2.0 | −2.0 | −2.0 |
| $b_2$ | 1.0 | 1.0 | 1.0 |
| $a_1$ | 0.179471731469 | −1.843990656105 | −1.991927118597 |
| $a_2$ | 0.008052525599 | 0.846816324065 | 0.991943411450 |

Table 4.8: The original coefficients for second order IIR biquads forming the A-filter according to the norm. [41]

Since discrepancies at low frequencies are much more important than discrepancies at higher frequencies in measurements of transportation noise (because of the shape of the spectrum), the remaining low-pass filter of the A-filter was then modified. The coeffi-

cient $a_2$ (all the original coefficients in Table 4.8) of the second high-pass filter was set to 0.846138871005, so that the whole microphone + HPbiquad + LPbiquad system would as much as possible satisfy the A-filter norm (Fig. 4.25).

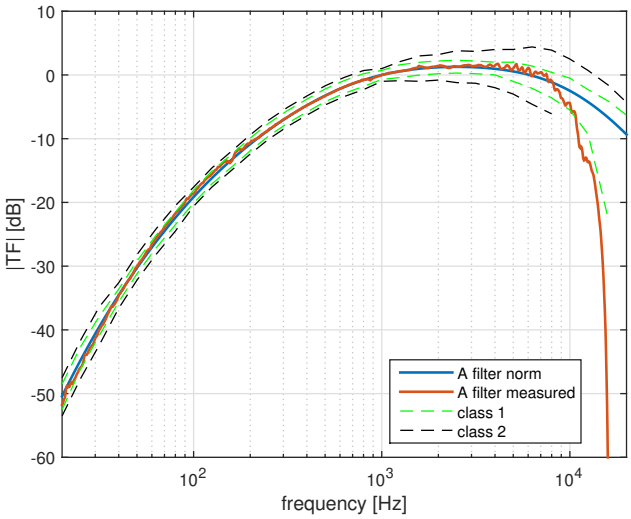


Figure 4.26: The transfer function of the MEMS microphne + A-filter containing two biquads (coefficient $a_2$ is modified).

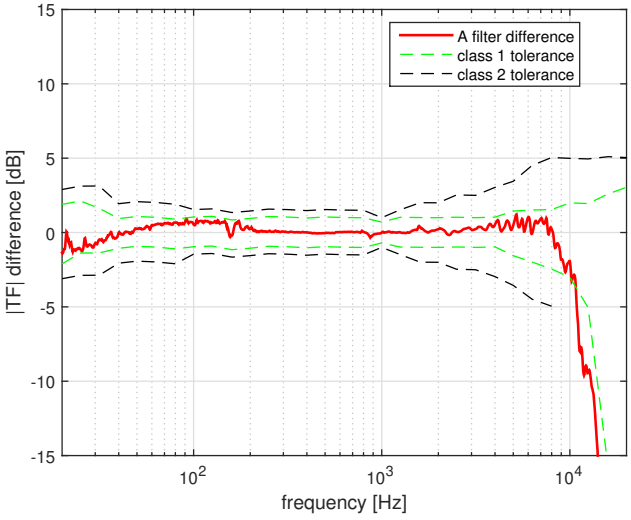


Figure 4.27: Difference between the measured transfer function and the transfer function given by the norm for the A-filter (containing two biquads, coefficient $a_2$ is modified).

The results (Fig. 4.26 and Fig. 4.27) provide evidence that the measured MEMS microphone system along with the modified A-filter complies with the norm for class I and

II tolerance in a wider frequency range (up to approximately 10 kHz) and offers better fitting.

### 4.3.4 Measurements of the dynamic range of the noise sensor

This section focuses on measurements of the dynamic range of the sensor, which gives an idea of the ratio of the largest signal that the sensor can handle (linearly) to the noise level. The measurements were performed using the reference prepolarized Free-field B &K 4189 1/2" microphone and the B&K Photon+ dynamic analyzer operating the SI activ 05 loudspeaker. The set of 21 prototypes of the noise sensor (each contained the microphone and PIC 32 processor, and each was connected through SPI to a small Raspberry Pi single board computer). The prototypes were measured one after another (the setup in Fig. 4.28), where the calibration constants were observed throughout the measurements.

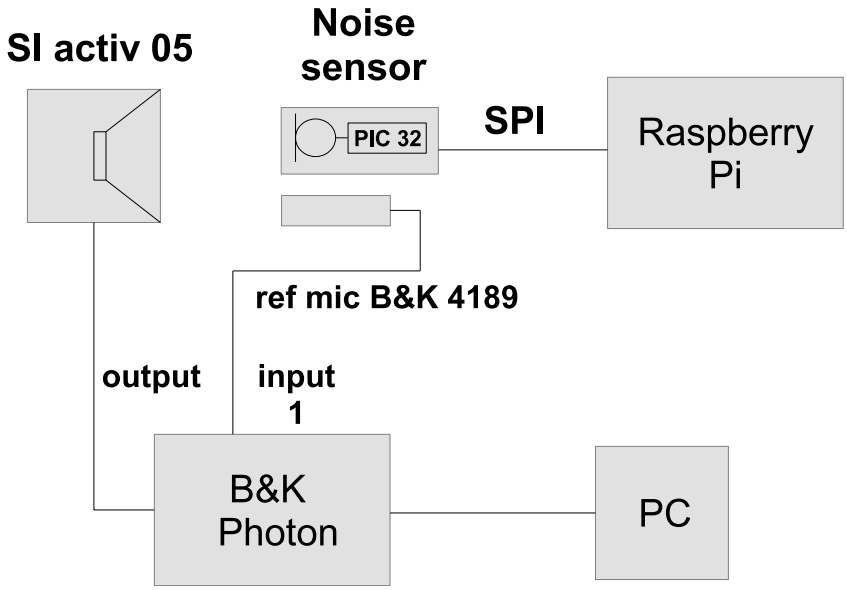


Figure 4.28: The setup scheme for the noise sensor dynamic range measurement.

The measured calibration constant of all measured sensor samples are shown in Table 4.3.4, where the maximum value is in bold.

It is clear that all the differences between the constants of all sensors are below 0.5 dB, so that an average value (115268.4101565 [1/Pa]) can be used, instead of using each calibration constant for a particular sensor.

The dynamic range of the sensor was measured using the measurement setup shown in Fig. 4.28. Fig. 4.29 shows the measured dynamic range of the sensor (red curve) compared to the ideal linear curve (black dashed line). The discrepancies at low levels are caused by selfnoise of the microphone, and the discrepancies at high levels are likely related to the nonlinear behaviour of the microphone at high incident acoustic pressure [38]. Fig. 4.30 shows the differences between the sensor output and the reference SPL.

| No. | **Calibration constant** $[1/Pa]$ | **Difference from average** $[1/Pa]$ | **Difference in** $[dB]$ |
|---|---|---|---|
| 203 | 169277.093750 | 54008.6835935 | 0.236 |
| 204 | **173857.625000** | **58589.2148435** | **0.238** |
| 209 | 105882.937500 | −9385.4726565 | 0.198 |
| 210 | 105574.554688 | −9693.8554685 | 0.199 |
| 212 | 107470.039063 | −7798.3710935 | 0.194 |
| 214 | 106491.250000 | −8777.1601565 | 0.197 |
| 215 | 103572.445313 | −11695.9648435 | 0.203 |
| 216 | 107357.296875 | −7911.1132815 | 0.194 |
| 217 | 105020.085938 | −10248.3242185 | 0.200 |
| 218 | 108871.820313 | −6396.5898435 | 0.190 |
| 219 | 109492.015625 | −5776.3945315 | 0.188 |
| 220 | 107598.445313 | −7669.9648435 | 0.194 |
| 221 | 109241.742188 | −6026.6679685 | 0.189 |
| 222 | 108974.492188 | −6293.9179685 | 0.189 |
| 223 | 109640.078125 | −5628.3320315 | 0.187 |
| 225 | 105972.640625 | −9295.7695315 | 0.198 |
| 226 | 106593.828125 | −8674.5820315 | 0.196 |
| 227 | 103535.039063 | −11733.3710935 | 0.203 |
| 228 | 108960.710938 | −6307.6992185 | 0.189 |
| 229 | 107988.062500 | −7280.3476565 | 0.193 |
| 230 | 108588.304688 | −6680.1054685 | 0.191 |

Table 4.9: Calibration constants of the sensor.

The results presented in Fig. 4.30 show that for tolerance ± 1 dB the upper limit is approximately 109 dB(A) SPL and the lower limit is 35 dB(A) SPL.

### 4.3.5 Temperature dependence of the noise sensor

In this part of the thesis, the temperature dependence of the MEMS microphone as a part of the noise sensor is analyzed and measured mimicking the areas of application of the devices. The main objective of this investigation was to determine whether the sensitivity of the microphone sensor drifts significantly with respect to the sensitivity of the reference microphone. The results are intended to provide insight into the thermal stability of the device.

First, it is necessary to mention the operating temperature ranges of components of the sensors, which may reduce the reliability and the performance of the device. These components are i) the ICS-43432 MEMS microphone, the temperature range of which, according to [44], is -40 to +85 ° C, ii) the PIC32MX170F256BIML processor with a temperature range from -40 to +105 ° C, and iii) the oscillator's DSC6083CI2A-032K768 range from -40 to +85° C.

The B&K 4189 reference microphone 1/2" has its own operating temperature range, which is -30 to +150 ° C. The temperature coefficient is -0.006 dB/K when measured at

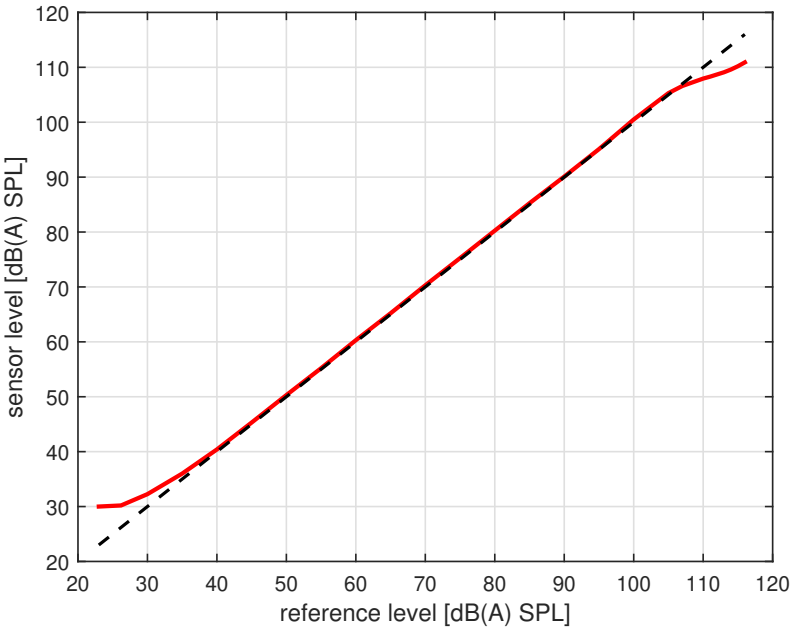


Figure 4.29: The measured dynamic range versus the reference.

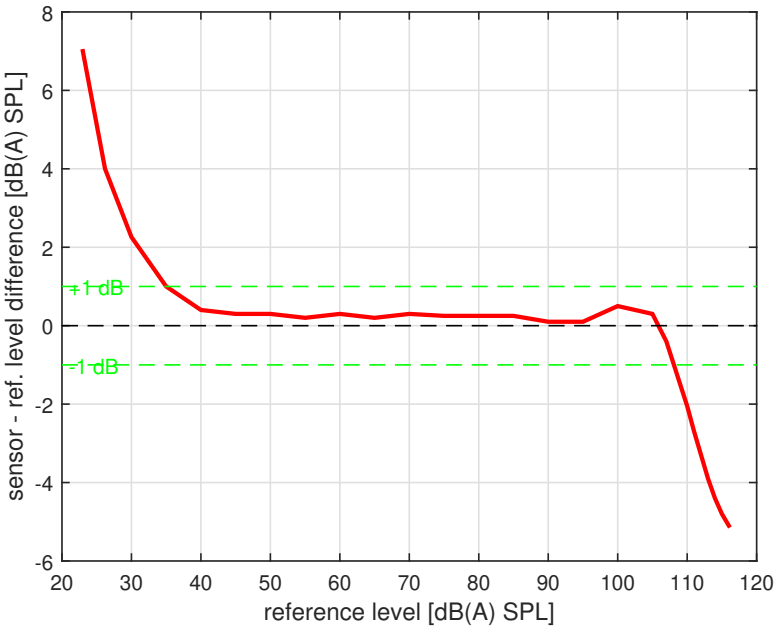


Figure 4.30: Differences between the measured dynamic range and the reference (detailed view).

250 Hz.

A test board assembly shown in Fig. 4.31 along with the reference microphone was placed in the Shjianheng SDJ6005 temperature chamber and was subjected to the range of harsh environmental condition from 60° C to -20° C, with a humidity level of up to 60 %. White noise was played as the test sound, and a level of 94 dB was maintained. The tracked values are shown in Table 4.3.5.

Figure 4.31: The measurement setup: the measured MEMS microphone ICS-43432 placed in the Shjianheng SDJ6005 temperature chamber.

Overall, the results indicated the following finding (Fig. 4.32): up to 1 percent changes in microphone sensitivity per degree Celsius change in temperature, which is a sufficiently low level. It can therefore be stated, that the temperature coefficient of the whole noise

| Sensor SPL[$dB$] | **Differences** [$dB$] | **Temperature** [$C°$] |
|---|---|---|
| 94.3 | 0.3 | $-20$ |
| 94.3 | 0.3 | $-10$ |
| 94.2 | 0.2 | $-5$ |
| 94.1 | 0.1 | 0 |
| 94.2 | 0.2 | 12 |
| 94.1 | 0.1 | 20 |
| 94.0 | 0 | 30 |
| 94.1 | 0.1 | 40 |
| 94.1 | 0.1 | 50 |
| 94.1 | 0.1 | 60 |

Table 4.10: Differences between the maintained referential dB level and the output of the tested noise sensor.

sensor is comparable with the coefficient of the measured microphone. The tested microphone demonstrated weak dependence on temperature, which is the main result obtained from the experiment.

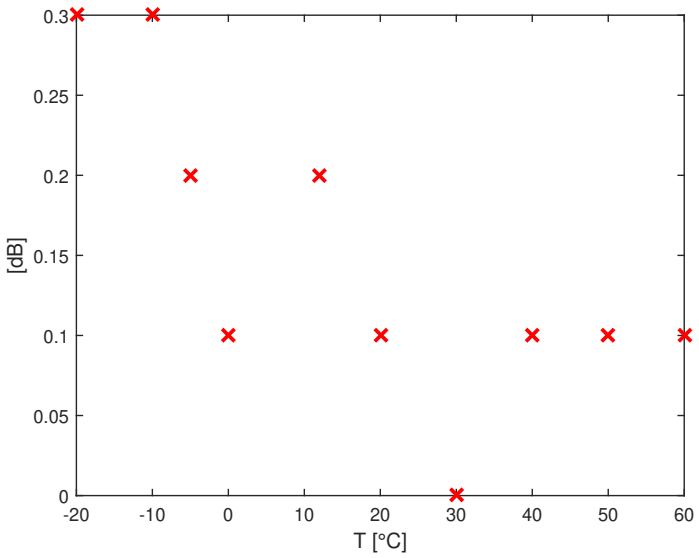


Figure 4.32: Differences between the maintained referential dB level and the output of the tested microphone.

### 4.3.6 Sound scattering on the Airtracker master unit

The Airtracker master unit (the dimensions are shown in Table 4.3.6) consists of the noise sensor, the VLC box and the main box. The scattered sound field is simulated numerically

(using Comsol Multiphysics software) inside a spherical domain from which the Airtracker master geometry is subtracted Fig. 4.34.

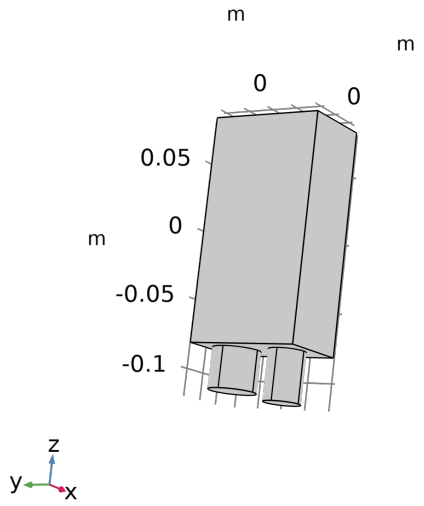


Figure 4.33: The Airtracker master unit.

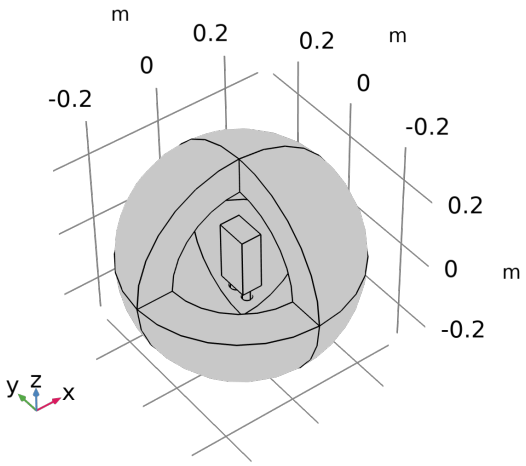


Figure 4.34: The scattering field on the Airtracker master unit.

| | Dimensions [mm] |
|---|---|
| Airtracker box | 165 x 85 x 55 |
| VOC sensor | ⌀35 x 30 |
| Noise sensor | ⌀27 x 37 |

Table 4.11: Dimensions of the Airtracker master unit.

The resulting acoustic pressure field (the addition of the incident and scattered field) is shown in Fig. 4.35 for different frequencies.

The frequency dependence of the difference of the sound pressure level caused by the scattering (with and without the box) in the position of the microphone is shown in Fig. 4.36. The Figure shows that the master unit box causes a difference in measurement of up to approximately 2 dB SPL in the higher frequency range (above 2kHz).

The difference remains small (below ± 0.5 dB) in the lower frequency range (up to 1 kHz), where most traffic noise energy occurs (Fig. 4.1). Note, that the dimensions of the Airtracker master unit seem to be smaller than the dimensions of the units found in other realizations [1, 3].

### 4.3.7 Results of noise monitoring using a wireless sensor network

The sound pressure level in a particular location generally varies due to fluctuations in the noise levels from the various noise sources in the area. Here we show examples of sensor network measurements in real conditions.

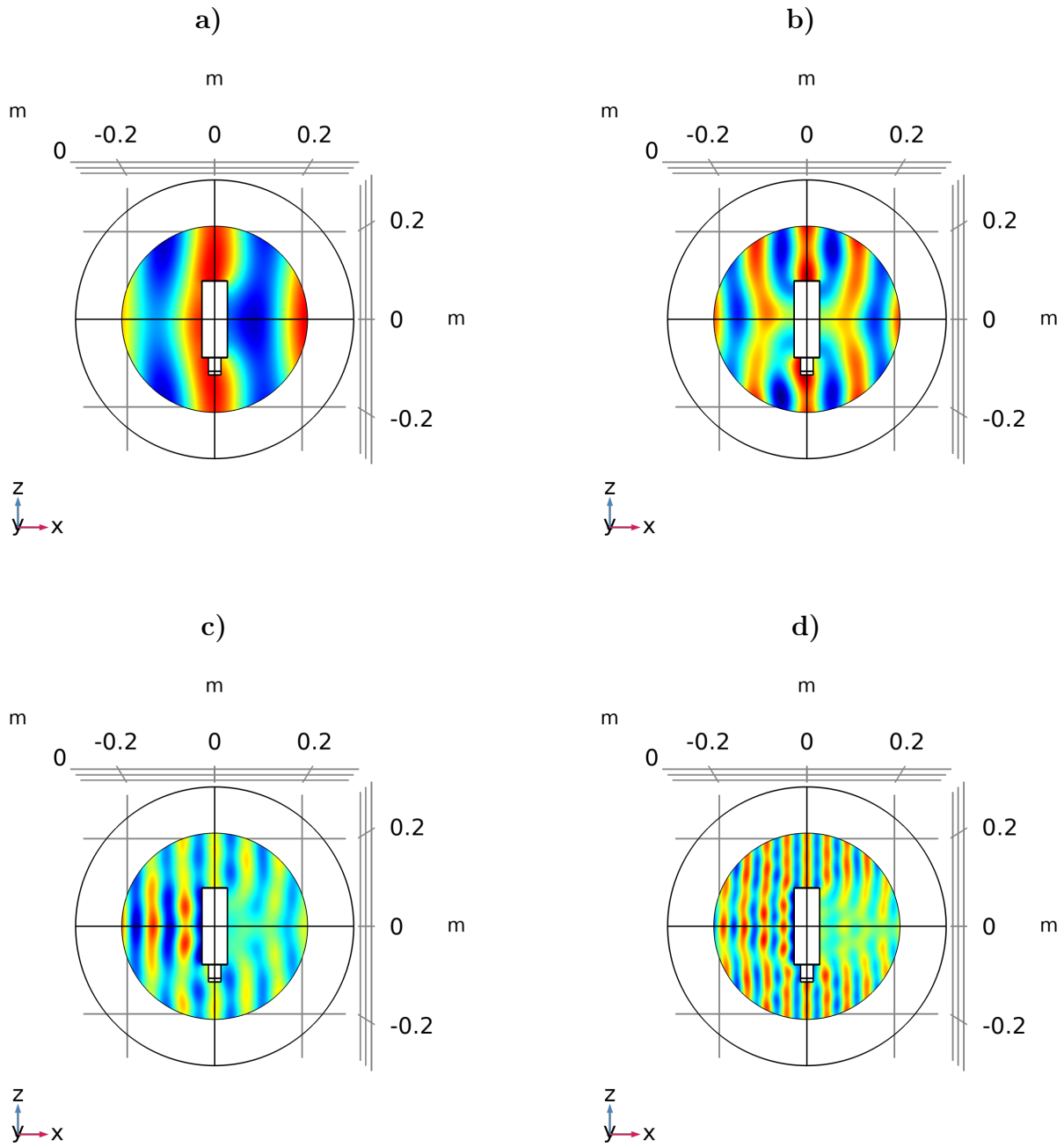


Figure 4.35: The effect of sound scattering on the acoustic pressure field, examples at a) 1.6kHz, b) 3.15 kHz, c) 5kHz, d) 8 kHz.

The contribution of various sources can be used to characterize the noise in the location. More detailed statistical distributions could potentially help to identify and distinguish between the sound from a specific activity and from traffic noise. This statement be

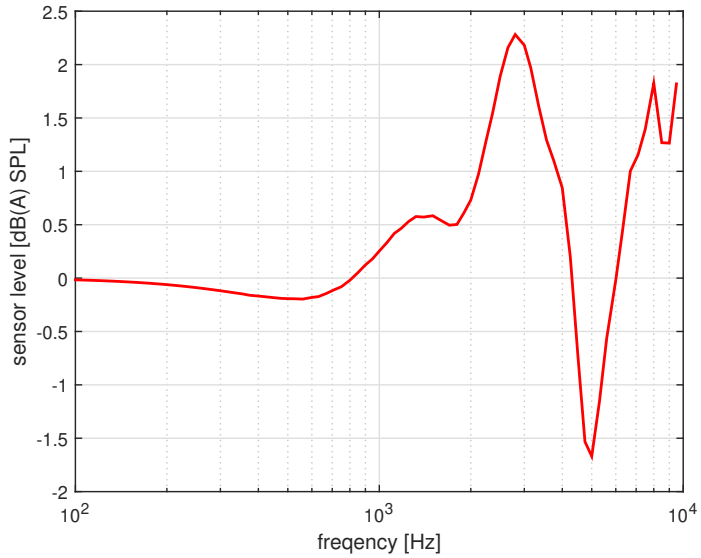


Figure 4.36: The frequency dependence of difference in sound pressure level caused by scattering.

illustrated by the sensor network deployed in the town of Lovosice, data from which are shown in this section. The data were transmitted every 15 minutes for a period of 12 months. Each record contains the average value and the maximum value of the sound pressure levels with an RMS integration time of 1s in dB(A) over the most recent 15 minutes.

Figure 4.37 shows the raw measured data from master unit No.343, representing the average and maximum values of the sound pressure level over a period of 12 months. It is clear that this type of a graphical representation of the data is not very useful.

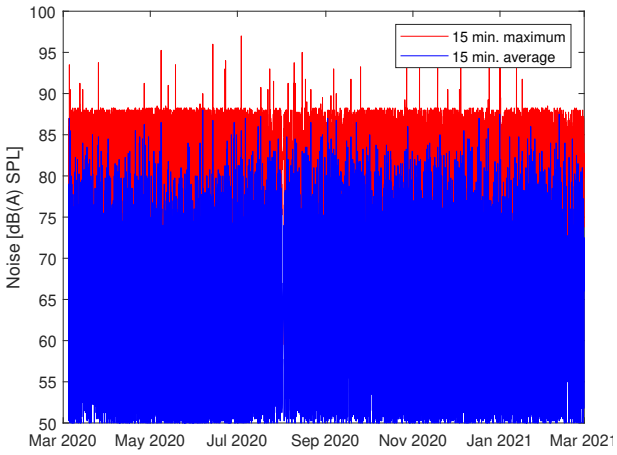


Figure 4.37: Measured data from master unit No.343.

Figure Fig. 4.38 presents more a relevant analysis. The histogram of the sound pressure levels shows the most frequent average and maximum values for the same period. The most frequent average SPL at this unit was around 70 dB(A)SPL, which is quite high. However, the maximum SPL does not exceed 90 dB(A)SPL, which can also be useful information.

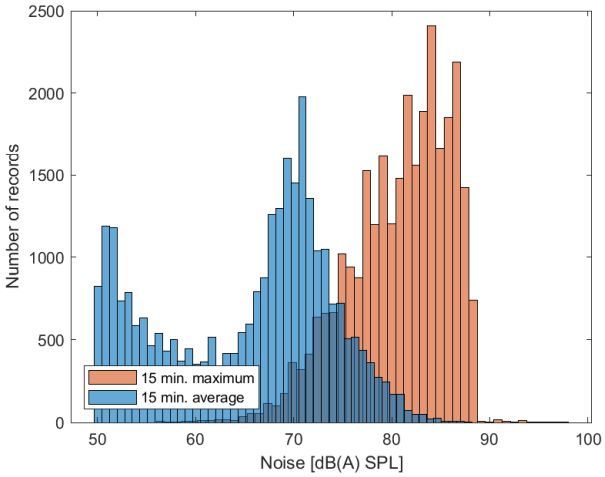


Figure 4.38: Histogram of sound pressure levels over a year (sensor node No.343).

The interpolated levels averaged over one hour during one day (y-axis) represented using the colormap in dB(A)SPL are shown in Figure Fig. 4.39 for the same period of 12 months (x-axis). The analysis shows the evaluation of the noise during each day of the 12-month period. Note that the white spots represent periods when no records were obtained from the sensor unit due to communication issues.

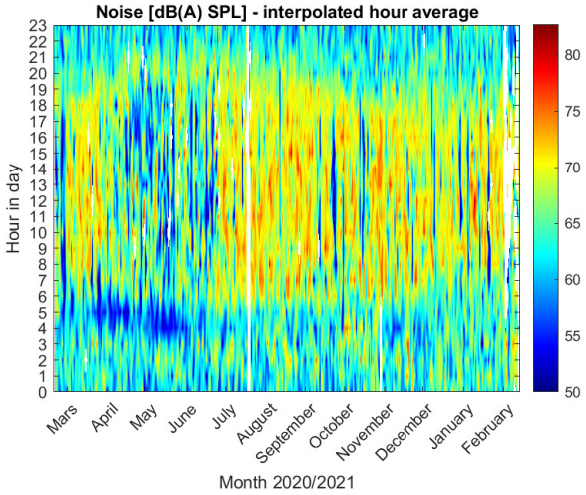


Figure 4.39: Interpolated sound pressure levels (sensor node No.343).

Fig. 4.40 shows an evaluation of the noise during the hours of the days of the week

averaged over the whole one-year period. The analysis shows clear differences between the night and day hours, but there are almost no differences between working days and weekends.

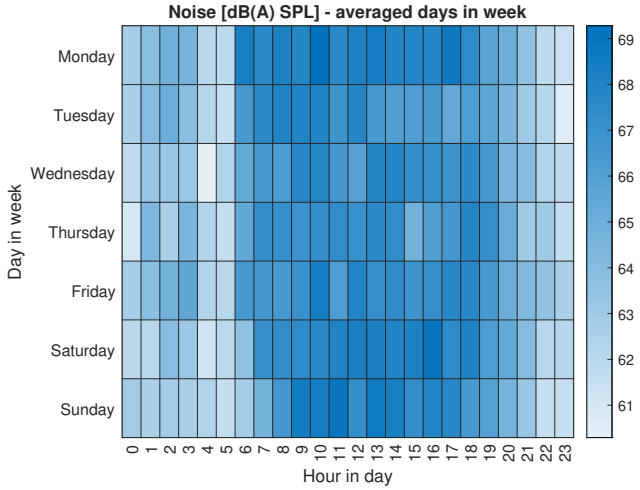


Figure 4.40: Averaged sound pressure levels over a week (sensor node No.343).

An evaluation of the traffic noise during each day of the 12-month period is shown in Fig. 4.41. The dark spots represent periods when no records were obtained from the sensor unit. There is no obvious pattern in the noise fluctuation, or rather the sound pressure levels are quite homogeneous over the course of a year in the measured area.

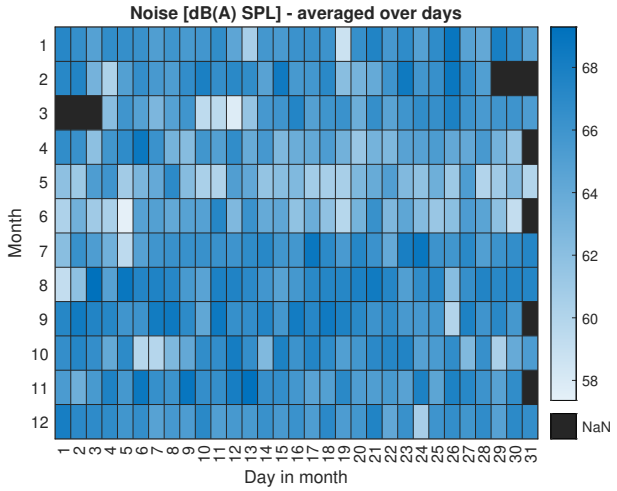


Figure 4.41: Day averaged sound pressure levels over a year (sensor node No.343).

# Chapter 5

# Conclusions and perspectives

## 5.1 Conclusions

This thesis aims to model an electroacoustic MEMS transducer with a moving square shaped clamped plate loaded by a thin fluid gap and a peripheral cavity. Several approaches are presented that involve an integral method for describing the acoustic pressure in the fluid gap and that require an analytical expression of the eigenfunctions of the square shaped clamped plate.

The first proposed approach aims to find an approximate form of the eigenfunctions of the moving electrode, which are searched for in the form of two-dimensional cosine series. The coefficients of the series are derived from a simple numerical solution for the moving electrode displacement without the loading acoustic elements.

The second approach presented in this study proposes an improved version of the approximated eigenfunctions of the rectangular clamped plate. It starts from the product of the orthonormal eigenfunctions $\phi(x)$ and $\phi(y)$ for elastic beams in $x$ and $y$ directions, which satisfy the boundary conditions of the clamped plate. The relevant point here is that, with this construction of the solution, satisfaction of the boundary conditions follows automatically from the fact that each of the eigenfunctions satisfies these boundary conditions. The use of the cosh functions leads to faster convergence. The second approach expressing the eigenfunctions is used in modelling the micromachined transducer with a perforated plate as a moving electrode. Perforation of the moving electrode is advantageous from the point of view of the MEMS fabrication process. The integral formulation for the acoustic pressure in the fluid gap needed to be adapted in order to take into account the coupling between this pressure and the incident acoustic pressure through the holes.

The third approach introduced in the thesis employs the same functions as in the second approach. Nevertheless, the proposed method is fully analytical and does not require any approximation from the numerical calculations. The "internal elastic plate coupling" also needs to be considered here. The method proposed here provides analytical results with precision in the frequency range of interest that is comparable with the precision of the numerically calculated results, but with much lower computational costs. In addition, this

approach can be useful not only in the domain of miniaturized transducers, but also in a wide range of other devices.

The measurements on the elements of the first version of the noise sensor prototype developed at the Department of Security Technologies and Engineering (the microphone alone and the full electroacoustic analog path) have shown that the sensor complies with the requirements for class II sound level meters in almost the whole frequency range of interest except at very low frequencies, where the validity of the measurement is questionable. The pressure sensitivities of the microphones used in the sensors show major dispersion (12.7 dB). Subsequent measurements proved that the variation in sensitivity depends strongly upon the variation of the equivalent polarization voltage originating in the electret layer, while the effect of the air gap thickness and the tension of the diaphragm is found to be much smaller. From the practical point of view, this means that applying a calibration constant (measured for each microphone) in the microcontroller is sufficient to compensate for the differences between the microphone samples. No major, variations in the shape of the frequency response are expected. In addition, good agreement was observed between the measured frequency responses of the measured microphones and the theoretical sensitivity curves calculated using the equivalent circuit with the estimated parameters.

A set of measurements was also carried out on a new version of the noise sensor prototype that has been developed recently at the Department of Security Technologies and Engineering. This noise sensor contains a low-cost MEMS microphone with digital output and a microcontroller (PIC32), where all of the remaining operations (A-filter, RMS calculation, conversion to dB SPL, output on SPI interface) are performed. The measurements investigated whether increased precision and reduced variation between the individual samples have been achieved. The results of the experiments confirm that the new version of the prototype produces superior results.

## 5.2 Perspectives

Further research will include a detailed examination of another MEMS microphone (ICS-43432 could potentially be replaced in the noise sensor by MEMS microphone SPH0645LM4H-1 designed by Knowles), which has a flatter frequency response.

Possible future research within a theoretical framework could proceed from the basis that only the first mode of the flexible perforated plate vibration has been taken into account here in using the analytically expressed approximation of its first eigenfunction calculated numerically. This is sufficient in the audio frequency range, but further research should focus on improved expression of the eigenfunctions to provide better results at frequencies above the first resonance, where higher modes of perforated plate vibration occur.

Another path of future research might be in modelling MEMS microphones with more complex shapes of the plates (the residual stress should be taken into account), and also in modelling some other forms of MEMS microphones (microbeams, elastically supported plates, etc.).

# Bibliography


[1] P. W. Wessels, T. G. H. Basten: *Design aspects of acoustic sensor networks for environmental noise monitoring*, Applied Acoustics 110, 227-34, (2016).

[2] P. Brynda, J. Kopřiva, and M. Horák. Trafficsensnet Sensor Network for Measuring Emissions from Transportation. In: Procedia Engineering Special Issue Eurosensors 2015. Eurosensors 2015, Freiburg, 2015-09-06/2015-09-09. Oxford: Elsevier Ltd, 2015. pp. 902-907. ISSN 1877-7058.

[3] C. Mydlarz, J. Salamon, J.P. Bello. *The implementation of low-cost urban acoustic monitoring devices*, Applied Acoustics 117, 207-218, 2017.

[4] Environmental Noise Directive (2002); at `https://www.environment.ec.europa.eu/topics/noise/environmental-noise-directive_en` [cit. 2023-05-01].

[5] World Health Organization (2010); Burden of Disease from Environmental Noise: Quantification of Healthy Life Years Lost in Europe, The World Health Organization; at `https://www.euro.who.int/__data/assets/pdf_file/0008/136466/e94888.pdf` [cit. 2023-05-02].

[6] European Environment Agency; Report No 21/2019; at `https://www.eea.europa.eu/publications/environmental-noise-in-europe` [cit. 2022-05-01].

[7] Nařízení vlády č. 272/2011 Sb., 2011.

[8] Joint position paper - EU legislation on road traffic noise; (2022) at `www.acea.auto/publication/position-paper-eu-legislation-on-road-traffic-noise` [cit. 2023-05-01].

[9] P. Scheeper, A. V. D. Donk, W. Olthuis, and P. Bergveld *A review of silicon microphones*, Sens. Actuators A 44, 1–11, 1994.

[10] G. M. Sessler *Silicon Microphones*, Journal of Audio Engineering Society 44 , 16-22, 1996.

[11] Zawawi S.A., Hamzah A.A., Majlis B.Y., Mohd-Yasin F. *A Review of MEMS Capacitive Microphones*, J. Microelectromechanical Syst. 11, 484, 2020.

[12] N. N. Peña-García, L. A. Aguilera-Cortés, M. A. Gonzáles-Palacios, J.-P. Raskin, A. L. Herrera-May *Design and Modeling of a MEMS Dual-Backplate Capacitive Microphone with Spring-Supported Diaphragm for Mobile Device Applications*, Sensors 18, 3545, 2018.

[13] Z. Škvor *On the Acoustical Resistance Due to Viscous Losses in the Air Gap of Electrostatic Transducers*, Acustic, 19, 295-299, 1967.

[14] J. Estèves, L. Rufer, D. Ekeom, S. Basrour, *Lumped-parameters equivalent circuit for condenser microphones modeling.* J. Acoust. Soc. Am., 142, 2121–2132, 2017.

[15] P. Honzík, M. Bruneau *Acoustic fields in thin fluid layers between vibrating walls and rigid boundaries: integral method*, Acta Acust. U. Acust. 101(4), 859-862, 2015.

[16] P. Honzík, A.Podkovskiy, S. Durand, N. Joly *Experimental investigation on the electrostatic receiver with small-sized backing electrode*, Forum Acusticum 2014 At: Krakow, September 2014.

[17] P. Honzík, C. Guianvarc'h, M. Bruneau *Modeling of capacitive MEMS microphone with square membrane or plate using integral method.* Procedia Engineering 120, 418 - 421, 2015.

[18] A. Novak, P. Honzík, M. Bruneau *Dynamic behaviour of a planar micro-beam loaded by a fluid-gap: analytical and numerical approach in a high frequency range, benchmark solutions*, J. Sound Vib., 2017. DOI information: 10.1016/j.jsv.2017.04.026.

[19] Th. Le Van Suu, S. Durand, M. Bruneau *On the modelling of a clamped plate loaded by a squeeze fluid film: application to miniaturized sensors*, Acta Acust. U. Acust. 96 (5), 923-935, 2010.

[20] T. Lavergne, S. Durand, M. Bruneau, and N. Joly *Dynamic Behavior of Circular Membrane and An Electrostatic Microphone: Effect of Holes In The Backing Electrode*, J. Acoust. Soc. Am. 128, 3459-3477, 2010.

[21] T. Lavergne, S. Durand, M. Bruneau, and N. Joly *Analytical Modeling of Electrostatic Transducers in Gases: Behavior of Their Membrane and Sensitivity*, Acta Acust. U. Acust. 100, 440-447, 2014.

[22] Zuckerwar A. J. *Theoretical response of condenser microphones*, J. Acoust. Soc. Am. 64(5), 1278-1285 1978.

[23] P. Malcovati, A. Baschirotto *The Evolution of Integrated Interfaces for MEMS Microphones*, Micromachines 9, 323, 2018.

[24] E.C. Wente *A condenser microphone as a uniformly sensitive instrument for the absolute measurement of sound intensity.* Physical Review 10(1), 39–63, 1917.

[25] W. R. Ali, M, Prasad *Piezoelectric MEMS based acoustic sensors: A review*, Sens. Actuator A Phys 301, 111756, 2020.

[26] L. L. Beranek, T. J. Mellow: *Acoustics, Sound Fields and Transducers*, Elsevier, Oxford, (2012).

[27] M. Bruneau, A.-M. Bruneau, Z. Škvor, and P. Lotton *An equivalent network modelling the strong coupling between a vibrating membrane and a fluid film*, Acta Acust. U. Acust. 2, 223–232, 1994.

[28] M. Bruneau, A.-M. Bruneau, and P. Dupire *A Model for Rectangular Miniaturized Microphones*, Acta Acust. U. Acust. 3, 275-282, 1995.

[29] Bruneau M., Scelo T. (translator and contributor), Fundamentals of Acoustics, ISTE, London, (2006).

[30] N. Joly, M. Bruneau, R. Bossart *Coupled Equations for Particle Velocity and Temperature Variation as the Fundamental Formulation of Linear Acoustics in Thermo-Viscous Fluids at Rest*, Acta Acust. U. Acust. 92, 202-209, 2006.

[31] N. Joly *Finite Element Modeling of Thermoviscous Acoustics on Adapted Anisotropic Meshes: Implementation of the Particle Velocity and Temperature Variation*, Acta Acust. U. Acust.96(1), 102-114, 2010.

[32] P. Honzík, A. Podkovskiy, S. Durand, N. Joly, M. Bruneau *Analytical and numerical modeling of an axisymmetrical electrostatic transducer with interior geometrical discontinuity*, J. Acoust. Soc. Am. 134, 3573-3579, 2013.

[33] W. R. Kampinga, Y. H. Wijnant, A. de Boer*An Efficient Finite Element Model for Viscothermal Acoustics*, Acta Acust. U. Acust.97, 618-631, 2011.

[34] M. J. Herring Jensen, E. Sandermann Olsen *Virtual prototyping of condenser microphone using the finite element method for detailed electric, mechanic, and acoustic characterisation*, Proceeding of Meetings on Acoustics 19, 030039, 2013.

[35] Acoustics Module User's Guide, COMSOL (2015).

[36] Structural Mechanics Module User's Guide, COMSOL (2015).

[37] Škvor, Z.: *Vibrating Systems and their Equivalent Circuits*, Elsevier, Amsterdam, (1991).

[38] A. Novak, P. Honzík *Measurement of nonlinear distortion of MEMS microphones*, Applied Acoustics 175 107802, 2021.

[39] A.W. Leissa: *Vibration of plates, Scientific and Technical Information Division*, Natl. Aeronaut. Space Adm., (1969).

[40] Beranek, L. L., Mellow, V. T.: *Acoustics: Sound Fields and Transducers*, Elsevier, UK, USA, (2012).

[41] ČSN EN 61672-17 ed.2. Česká technická norma: Elektroakustika - Zvukoměry - Část 1: Technické požadavky. Praha, 2014.

[42] Kergomard J., Garcia A. *Simple discontinuities in acoustic waveguides at low frequencies: critical analysis and formulae*, J. Sound Vib. 114(3), 465-479, 1987.

[43] Barrera-Figueroa S., Rasmussen K., Jacobsen F. *Hybrid method for determining the parameters of condenser microphones from measured membrane velocities and numerical calculations*, J. Acoust. Soc. Am. 126, 1788-1795, 2009.

[44] TDK. ICS-43432 Low-Noise Microphone with I2 S Digital Output; at `https://product.tdk.com/system/files/dam/doc/product/sw_piezo/mic/mems-mic/data_sheet/ics-43432-data-sheetv1.3.pdf`. [cit. 2022-05-02].

[45] International Electrotechnical Commission IEC 61094- 6, Measurement microphones, part 6 : Electrostatic actuators for determination of frequency response, (2004).

[46] Guianvarch C., Gavioso R. M., Benedetto G., Pitre L., Bruneau M. *Characterization of condenser microphones under different environmental conditions for accurate speed of sound measurements with acoustic resonators*, Rev. Sci. Instrum. 80, 074901, (2009).

[47] Jarvis D.R. *The accuracy of the electrostatic actuator method of determining the frequency response of condenser microphones*, J. Sound Vib. 123, 63-70, 1988.

[48] Rufer, L., De Pasquale, G., Esteves, J., Randazzo, F., Basrour, S., Soma, A. *Micro-acoustic source for hearing applications fabricated with 0.35$\mu$m CMOS-MEMS proces*, Procedia Engineering 120, 944 - 947, 2015.

[49] Ganji, B. A., Sedaghat, S. B., Roncaglia, A., Belsito, L. *Design and fabrication of very small MEMS microphone with silicon diaphragm supported by Z-shape arms using SOI wafer*, Solid State Electronics 148, 27-34, 2018.

# Reviewed Publications of the Author Relevant to the Thesis


[A.1] K. Šimonova, P. Honzík *Modelling of MEMS transducers with perforated moving electrodes*, Micromachines, 2023, 14, 921.

[A.2] K. Abramova, P. Honzík, M. Bruneau, P. Gatignol *Modelling approach for MEMS transducers with rectangular clamped plate loaded by a thin fluid layer.* Journal of Sound and Vibration. 473. 2020

[A.3] K. Abramova, P. Honzík *Experimental Estimation of Unknown Parameters of Equivalent Circuits of Low-cost Electret Microphones*, Akustické listy, 23(1–4), December 2017.

# Remaining Publications of the Author Relevant to the Thesis

[A.4] K. Šimonova, P. Honzík, N. Joly, S.Durand, M. Bruneau *Modelling of a MEMS Transducer with a moving electrode in form of perforated square plate*, Conference: e-Forum Acusticum At: Lyon, France, December 2020.

[A.5] K. Abramova, P. Honzík, N. Joly, S. Durand, M. Bruneau, *Modelling of a MEMS transducer using approximate eigenfunctions of a square clamped plate*, Conference: 23rd International Congress on Acoustics, integrating 4th EAA Euroregio 2019 At: Aachen, Germany, September 2019.

[A.6] K. Abramova, P. Honzík, N. Joly, S. Durand, M. Bruneau, *Modelling of a MEMS transducer with a square plate loaded by a thin fluid layer*, Euronoise 2018. Heraklion, Crete, 27.05.2018 - 31.05.2018. Madrid: European Acoustics Association. 2018, s. 337-340. ISSN 2226-5147.

# Citations of the Author's Publications Relevant to the Thesis

[A.7] K. Karthikeyan, L. Sujatha, R. Sundar. *A Low-Cost Fabrication and Numerical Simulation of a MEMS Acoustic Transducer Using Polyimide Membrane on FR4 Substrate*, Journal of Electronic Materials, vol. 50, no. 11, pp. 6489 - 6503, 2021. ISSN 0361-5235.

[A.8] V. Sharma, S. Kumar. *A comprehensive analysis of horizontally polarized shear waves in a thin microstructural plate*, Structural Engineering And Mechanics, vol. 85, no. 4, pp. 501 - 510, 2023. ISSN 1225-4568.

Both referencing [A.2].

# Appendix A

# Calculated Fourier coefficients for 4 eigenmodes

## A.1 Non perforated plate

| *No.* | $s_1$ | $s_2$ | *No.* | $s_1$ | $s_2$ |
|---|---|---|---|---|---|
| $c_{11,11}$ | 0.488190745771422 | $7.21754150443867e-7$ | $c_{77,11}$ | $6.58044736640952e-5$ | $-1.69085332954968e-8$ |
| $c_{31,11}$ | $-0.0737463299597355$ | $2.22534579917150e-6$ | $c_{79,11}$ | $3.18410648116090e-5$ | $-8.62130755264389e-9$ |
| $c_{51,11}$ | $-0.0171173798396425$ | $6.07182707413524e-7$ | $c_{7\,11,11}$ | $1.92482769507957e-5$ | $-5.15587565494236e-9$ |
| $c_{71,11}$ | $-0.00644092129888515$ | $2.41794961950658e-7$ | $c_{7\,13,11}$ | $1.29313329223793e-5$ | $-3.40668629845524e-9$ |
| $c_{91,11}$ | $-0.00307494871380977$ | $1.18161536696161e-7$ | $c_{91,11}$ | $-0.00307495046344632$ | $1.18161495734019e-7$ |
| $c_{11\,1,11}$ | $-0.00169711723790527$ | $6.59485320057648e-8$ | $c_{93,11}$ | 0.000547146267945613 | $-6.47519538780576e-8$ |
| $c_{13\,1,11}$ | $-0.00103278098231332$ | $4.03756342326086e-8$ | $c_{95,11}$ | 0.000109026060402378 | $-2.16992411094820e-8$ |
| $c_{31,11}$ | $-0.0737463280700063$ | $2.22534685208489e-6$ | $c_{97,11}$ | $3.18420619243436e-5$ | $-8.62118873402473e-9$ |
| $c_{33,11}$ | 0.00936706525881666 | $-1.06703190864108e-6$ | $c_{99,11}$ | $1.29048897489829e-5$ | $-4.05326521224082e-9$ |
| $c_{35,11}$ | 0.00245237204276270 | $-3.05958119225808e-7$ | $c_{9\,11,11}$ | $6.95931111603567e-6$ | $-2.26860325258746e-9$ |
| $c_{37,11}$ | 0.00105423349210170 | $-1.27417949228831e-7$ | $c_{9\,13,11}$ | $4.49420158222402e-6$ | $-1.45697222042485e-9$ |
| $c_{39,11}$ | 0.000547147168682302 | $-6.47518517328576e-8$ | $c_{111,11}$ | $-0.00169711713217699$ | $6.59483578304569e-8$ |
| $c_{3\,11,11}$ | 0.000317693033198022 | $-3.72316151754252e-8$ | $c_{113,11}$ | 0.000317692494238966 | $-3.72314862180483e-8$ |
| $c_{3\,13,11}$ | 0.000199617307025568 | $-2.32962396165433e-8$ | $c_{115,11}$ | $6.67887937641841e-5$ | $-1.30099079897188e-8$ |
| $c_{51,11}$ | $-0.0171173785937966$ | $6.07182240649809e-7$ | $c_{117,11}$ | $1.92481264772312e-5$ | $-5.15588728791365e-9$ |
| $c_{53,11}$ | 0.00245237374318393 | $-9.53731853933569e-8$ | $c_{119,11}$ | $6.95985380240264e-6$ | $-2.26853463250392e-9$ |
| $c_{55,11}$ | 0.000504432021800605 | $-9.53731853933569e-8$ | $c_{11\,11,11}$ | $3.18237568446832e-6$ | $-1.15357735914955e-9$ |
| $c_{57,11}$ | 0.000202055483703816 | $-4.10322340978887e-8$ | $c_{11\,13,11}$ | $1.83442979303910e-6$ | $-6.81895687826475e-10$ |
| $c_{59,11}$ | 0.000109026261566279 | $-2.16992345318963e-8$ | $c_{131,11}$ | $-0.00103278041942973$ | $4.03758858173053e-8$ |
| $c_{5\,11,11}$ | $6.67880241559604e-5$ | $-1.30098728762035e-8$ | $c_{133,11}$ | 0.000199618902747248 | $-2.32963059504384e-8$ |
| $c_{5\,13,11}$ | $4.38957723646164e-5$ | $-8.43960442924219e-9$ | $c_{135,11}$ | $4.38954208741069e-5$ | $-8.43957327062881e-9$ |
| $c_{71,11}$ | $-0.00644092167331908$ | $2.41795085264055e-7$ | $c_{137,11}$ | $1.29311950549552e-5$ | $-3.40669627015491e-9$ |
| $c_{73,11}$ | 0.00105423245041900 | $-1.27418157073933e-7$ | $c_{139,11}$ | $4.49399519412351e-06$ | $-1.45698922163830e-09$ |
| $c_{75,11}$ | 0.000202056136518160 | $-4.10320728243872e-8$ | $c_{1311,11}$ | $1.83500882240605e-06$ | $-6.81870930991587e-10$ |
| | | | $c_{1313,11}$ | $8.95910792298620e-07$ | $-3.62678479126576e-10$ |

Table A.1: The example of the fit of the Fourier coefficients for mn=11.

Coefficients for modes 13 and 31 was found to be same for any plate dimentions. Therefore there was no need in fitting them.

| $No.$ | $c$ |
|---|---|
| $c_{11,13}$ | $-6.67737042523633e-05$ |
| $c_{31,13}$ | $-4.785039725658190e-04$ |
| $c_{51,13}$ | $1.112825047752510e-04$ |
| $c_{71,13}$ | $3.385005727043630e-05$ |
| $c_{91,13}$ | $1.547472333264460e-05$ |
| $c_{11\ 1,13}$ | $8.424210311062590e-06$ |
| $c_{13\ 1,13}$ | $5.098644735906600e-06$ |
| $c_{31,13}$ | $7.289941033761830e-06$ |
| $c_{33,13}$ | $4.63610843367581e-05$ |
| $c_{35,13}$ | $-9.69194541077473e-06$ |
| $c_{37,13}$ | $-3.13344223105061e-06$ |
| $c_{39,13}$ | $-1.51507149725621e-06$ |
| $c_{3\ 11,13}$ | $-8.57377032777803e-07$ |
| $c_{3\ 13,13}$ | $-5.33060641827742e-07$ |
| $c_{51,13}$ | $2.90259372723181e-06$ |
| $c_{53,13}$ | $1.63885421277902e-05$ |
| $c_{55,13}$ | $-3.33871340731213e-06$ |
| $c_{57,13}$ | $-1.01050839312636e-06$ |
| $c_{59,13}$ | $-4.96599912246719e-07$ |
| $c_{5\ 11,13}$ | $-2.91816985150812e-07$ |
| $c_{5\ 13,13}$ | $-1.87597442735206e-07$ |
| $c_{71,13}$ | $1.03237795384463e-06$ |
| $c_{73,13}$ | $7.49385173136028e-06$ |
| $c_{75,13}$ | $-1.59405375305903e-06$ |
| $c_{77,13}$ | $-4.38962219543678e-07$ |

| $No.$ | $c$ |
|---|---|
| $c_{79,13}$ | $-2.00890637521799e-07$ |
| $c_{7\ 11,13}$ | $-1.16661293775300e-07$ |
| $c_{7\ 13,13}$ | $-7.62005396092702e-08$ |
| $c_{91,13}$ | $4.96009500028628e-07$ |
| $c_{93,13}$ | $3.94592369256562e-06$ |
| $c_{95,13}$ | $-8.95370810082374e-07$ |
| $c_{97,13}$ | $-2.38426650077578e-07$ |
| $c_{99,13}$ | $-1.00304276166359e-07$ |
| $c_{9\ 11,13}$ | $-5.42367497260328e-08$ |
| $c_{9\ 13,13}$ | $-3.47116827018831e-08$ |
| $c_{111,13}$ | $2.75120695568125e-07$ |
| $c_{113,13}$ | $2.30011325327934e-06$ |
| $c_{115,13}$ | $-5.51746067548069e-07$ |
| $c_{117,13}$ | $-1.48088905029414e-07$ |
| $c_{119,13}$ | $-5.93105872978073e-08$ |
| $c_{11\ 11,13}$ | $-2.98722435621562e-08$ |
| $c_{11\ 13,13}$ | $-1.76823742505975e-08$ |
| $c_{131,13}$ | $1.67872349650443e-07$ |
| $c_{133,13}$ | $1.44680525550709e-06$ |
| $c_{135,13}$ | $-3.62013395612060e-07$ |
| $c_{137,13}$ | $-9.97047402138945e-08$ |
| $c_{139,13}$ | $-3.91545874916337e-08$ |
| $c_{1311,13}$ | $-1.87825583398677e-08$ |
| $c_{1313,13}$ | $-1.05052972571717e-08$ |

Table A.2: Calculated Fourier coefficients for mn=13.

| *No.* | $s_1$ | $s_2$ |
|---|---|---|
| $c_{11,33}$ | −0.00398090971332984 | $2.87183254824234e-08$ |
| $c_{31,33}$ | −0.0420252206223733 | $1.76254302310435e-07$ |
| $c_{51,33}$ | 0.00999918685432539 | $-4.16001822847450e-08$ |
| $c_{71,33}$ | 0.00281649522310030 | $-3.40832009532651e-08$ |
| $c_{91,33}$ | 0.00131617894906873 | $-1.94755452060153e-08$ |
| $c_{11\ 1,33}$ | 0.000725312591171632 | $-1.14761641104847e-08$ |
| $c_{13\ 1,33}$ | 0.000441645179998452 | $-7.47217013386350e-09$ |
| $c_{31,33}$ | −0.0420252171920166 | $1.76254607094884e-07$ |
| $c_{33,33}$ | −0.476156895841691 | $-4.65383027908614e-07$ |
| $c_{35,33}$ | 0.0901868918808722 | $-9.14619606782036e-07$ |
| $c_{37,33}$ | 0.0323034605226375 | $-3.48961012006396e-07$ |
| $c_{39,33}$ | 0.0160345589962290 | $-1.86520671760075e-07$ |
| $c_{3\ 11,33}$ | 0.00916066162103240 | $-1.12150674758224e-07$ |
| $c_{3\ 13,33}$ | 0.00571497123710600 | $-7.22117077917541e-08$ |
| $c_{51,33}$ | 0.00999921413770601 | $-4.15457996831938e-08$ |
| $c_{53,33}$ | 0.0901868929124563 | $-9.14598494866312e-07$ |
| $c_{55,33}$ | −0.0156217992966271 | $4.42962243820755e-07$ |
| $c_{57,33}$ | −0.00564490877700571 | $1.75557178667705e-07$ |
| $c_{59,33}$ | −0.00292696819438076 | $9.25811873618122e-08$ |
| $c_{5\ 11,33}$ | −0.00174553515452202 | $5.47435160072980e-08$ |
| $c_{5\ 13,33}$ | −0.00112763515513656 | $3.49550112244560e-08$ |
| $c_{71,33}$ | 0.00281647462817071 | $-3.41153959045479e-08$ |
| $c_{73,33}$ | 0.0323034591419585 | $-3.48955436035397e-07$ |
| $c_{75,33}$ | −0.00564491125796605 | $1.75567566020794e-07$ |

| *No.* | $s_1$ | $s_2$ |
|---|---|---|
| $c_{77,33}$ | −0.00190705728715948 | $7.69696609741327e-08$ |
| $c_{79,33}$ | −0.000959486575507188 | $4.29311735104329e-08$ |
| $c_{7\ 11,33}$ | −0.000574888412155458 | $2.63401672351434e-08$ |
| $c_{7\ 13,33}$ | −0.000378521242779634 | $1.71077070131027e-08$ |
| $c_{91,33}$ | 0.00131618686717522 | $-1.94691557542368e-08$ |
| $c_{93,33}$ | 0.0160345523022928 | $-1.86539613449221e-07$ |
| $c_{95,33}$ | −0.00292697365111587 | $9.25858943731007e-08$ |
| $c_{97,33}$ | −0.000959494141418017 | $4.29352024921190e-08$ |
| $c_{99,33}$ | −0.000456683182729847 | $2.52617726575361e-08$ |
| $c_{9\ 11,33}$ | −0.000263671160839958 | $1.59429176117693e-08$ |
| $c_{9\ 13,33}$ | −0.000171691278974817 | $1.06600395406921e-08$ |
| $c_{111,33}$ | 0.000725307604138401 | $-1.14855365571149e-08$ |
| $c_{113,33}$ | 0.00916066193056145 | $-1.12147391554004e-07$ |
| $c_{115,33}$ | −0.00174554339236310 | $5.47331694553856e-08$ |
| $c_{117,33}$ | −0.000574891734905042 | $2.63402708161837e-08$ |
| $c_{119,33}$ | −0.000263677628030128 | $1.59445750958518e-08$ |
| $c_{11\ 11,33}$ | −0.000144886381791387 | $1.04027079942212e-08$ |
| $c_{11\ 13,33}$ | $-9.08698186057590e-05$ | $6.98852093834848e-09$ |
| $c_{131,33}$ | 0.000441639749150563 | $-7.46861213467608e-09$ |
| $c_{133,33}$ | 0.00571496188090708 | $-7.22173575881849e-08$ |
| $c_{135,33}$ | −0.00112763035590078 | $3.49538943160926e-08$ |
| $c_{137,33}$ | −0.000378521996313767 | $1.71028364909655e-08$ |
| $c_{139,33}$ | −0.000171693074158633 | $1.06621216469665e-08$ |
| $c_{1311,33}$ | $-9.08789916396711e-05$ | $6.98725566533366e-09$ |
| $c_{1313,33}$ | $-5.44095286615958e-05$ | $4.84608732579676e-09$ |

Table A.3: The example of the fit of the Fourier coefficients for mn=33.

## A.2 Perforated plate

| $No.$ | $c$ |
|---|---|
| $c_{11,11}$ | 1.04807751064599 |
| $c_{31,11}$ | 0.0142971369156299 |
| $c_{51,11}$ | 0.00180972134580043 |
| $c_{71,11}$ | 0.000339039037047805 |
| $c_{91,11}$ | $5.11886167190213e-05$ |
| $c_{11\,1,11}$ | $-1.91142395231611e-05$ |
| $c_{13\,1,11}$ | $-3.41869137986796e-05$ |
| $c_{31,11}$ | 0.0142524202590173 |
| $c_{33,11}$ | −0.00332162565461653 |
| $c_{35,11}$ | −0.00102566474952723 |
| $c_{37,11}$ | −0.000332752278644111 |
| $c_{39,11}$ | −0.000125141152834547 |
| $c_{3\,11,11}$ | $-5.45844813321501e-05$ |
| $c_{3\,13,11}$ | $-2.61262165799268e-05$ |
| $c_{51,11}$ | 0.00178027429191334 |
| $c_{53,11}$ | −0.00102572522523699 |
| $c_{55,11}$ | −0.000474601238265698 |
| $c_{57,11}$ | −0.000198380502067025 |
| $c_{59,11}$ | $-8.69412595996356e-05$ |
| $c_{5\,11,11}$ | $-4.11460501403820e-05$ |
| $c_{5\,13,11}$ | $-2.10405673922715e-05$ |
| $c_{71,11}$ | 0.000347056510440440 |
| $c_{73,11}$ | −0.000336023966506700 |
| $c_{75,11}$ | −0.000199501984906411 |
| $c_{77,11}$ | $-9.96565997735157e-05$ |

| $No.$ | $c$ |
|---|---|
| $c_{79,11}$ | $-4.95233875228989e-05$ |
| $c_{7\,11,11}$ | $-2.65700295662084e-05$ |
| $c_{7\,13,11}$ | $-1.34416879561769e-05$ |
| $c_{91,11}$ | $3.98577276907604e-05$ |
| $c_{93,11}$ | −0.000125745706451521 |
| $c_{95,11}$ | $-8.53849552823899e-05$ |
| $c_{97,11}$ | $-4.95585386805969e-05$ |
| $c_{99,11}$ | $-2.78835952720372e-05$ |
| $c_{9\,11,11}$ | −0.000102347362568194 |
| $c_{9\,13,11}$ | $-5.59242414752907e-05$ |
| $c_{111,11}$ | $-2.21846599307364e-05$ |
| $c_{113,11}$ | $-5.51135461535711e-05$ |
| $c_{115,11}$ | $-4.05511338192234e-05$ |
| $c_{117,11}$ | $-2.63030839462802e-05$ |
| $c_{119,11}$ | $-1.54999571081649e-05$ |
| $c_{11\,11,11}$ | $-9.59673588217139e-06$ |
| $c_{11\,13,11}$ | $-5.68383880011744e-06$ |
| $c_{131,11}$ | $-3.25998854904130e-05$ |
| $c_{133,11}$ | $-2.63188772048206e-05$ |
| $c_{135,11}$ | $-2.03137992661928e-05$ |
| $c_{137,11}$ | $-1.41628079014941e-05$ |
| $c_{139,11}$ | $1.43100703964290e-06$ |
| $c_{1311,11}$ | $-1.70409878423349e-06$ |
| $c_{1313,11}$ | $4.29244279652475e-07$ |

Table A.4: Calculated Fourier coefficients for mn=11 ($a = 0.5 \cdot 10^{-3} m$)

| $No.$ | $c$ |
|---|---|
| $c_{11,13}$ | $-0.01386009839898147$ |
| $c_{31,13}$ | $1.045962023924494$ |
| $c_{51,13}$ | $0.005640082661587015$ |
| $c_{71,13}$ | $9.324765245784676e-4$ |
| $c_{91,13}$ | $4.0955124617555475e-5$ |
| $c_{11\ 1,13}$ | $-1.616849772356883e-4$ |
| $c_{13\ 1,13}$ | $-1.8575320879015182e-4$ |
| $c_{31,13}$ | $-0.006161614623744604$ |
| $c_{33,13}$ | $0.06604605423884422$ |
| $c_{35,13}$ | $-0.0015478055340508098$ |
| $c_{37,13}$ | $-6.044758324041494e-4$ |
| $c_{39,13}$ | $-2.6184664653500743e-4$ |
| $c_{3\ 11,13}$ | $-1.2191777658351821e-4$ |
| $c_{3\ 13,13}$ | $-6.856562161350114e-5$ |
| $c_{51,13}$ | $-0.001679006478282459$ |
| $c_{53,13}$ | $0.01347448505715955$ |
| $c_{55,13}$ | $-0.00113647598686944$ |
| $c_{57,13}$ | $-5.398034834671719e-4$ |
| $c_{5\ 11,13}$ | $-2.554735144263518e-4$ |
| $c_{5\ 13,13}$ | $-1.3032586387997405e-4$ |
| $c_{71,13}$ | $-7.155024628023731e-5$ |
| $c_{73,13}$ | $-4.612193105135955e-4$ |
| $c_{75,13}$ | $0.0039256330452609785$ |
| $c_{77,13}$ | $0.0039256330452609785$ |

| $No.$ | $c$ |
|---|---|
| $c_{79,13}$ | $-3.4554049965732347e-4$ |
| $c_{7\ 11,13}$ | $-1.8994843188372613e-4$ |
| $c_{7\ 13,13}$ | $-1.0354783220188967e-4$ |
| $c_{91,13}$ | $-5.752332067375438e-5$ |
| $c_{93,13}$ | $-1.5496230872434117e-4$ |
| $c_{95,13}$ | $0.00135621501509748$ |
| $c_{97,13}$ | $-2.7977422600839933e-4$ |
| $c_{99,13}$ | $-1.9460964451622855e-4$ |
| $c_{9\ 11,13}$ | $-1.2021469140615107e-4$ |
| $c_{9\ 13,13}$ | $-4.2121837462063557e-4$ |
| $c_{111,13}$ | $-2.706654091986014e-4$ |
| $c_{113,13}$ | $-6.475155256234491e-5$ |
| $c_{115,13}$ | $5.43734059988866e-4$ |
| $c_{117,13}$ | $-1.48219431347573e-4$ |
| $c_{119,13}$ | $-1.1097977961562195e-4$ |
| $c_{11\ 11,13}$ | $-7.373607757828233e-5$ |
| $c_{11\ 13,13}$ | $-5.114229464518724e-5$ |
| $c_{131,13}$ | $-3.389301175924554e-5$ |
| $c_{133,13}$ | $-3.2807223571326145e-5$ |
| $c_{135,13}$ | $2.361907784687748e-4$ |
| $c_{137,13}$ | $-7.718525273482814e-5$ |
| $c_{139,13}$ | $-6.0573551354565225e-5$ |
| $c_{1311,13}$ | $1.1548699064095416e-5$ |
| $c_{1313,13}$ | $-7.186100692208483e-6$ |
| $c_{1313,13}$ | $1.5418706994935512e-7$ |

Table A.5: Calculated Fourier coefficients for mn=13 ($a = 0.5 \cdot 10^{-3} m$)

| $No.$ | $c$ |
|---|---|
| $c_{11,31}$ | 0.01387809945563094 |
| $c_{31,31}$ | $-0.0018292698768895125$ |
| $c_{51,31}$ | 0.001620696212191238 |
| $c_{71,31}$ | $4.4962047936946624e-4$ |
| $c_{91,31}$ | $1.5955223141127491e-4$ |
| $c_{11\ 1,31}$ | $7.01383828927337e-5$ |
| $c_{13\ 1,31}$ | $3.1777340498011816e-5$ |
| $c_{31,31}$ | $-1.0459427657365976$ |
| $c_{33,31}$ | $-0.06664227798427742$ |
| $c_{35,31}$ | $-0.013532455909353888$ |
| $c_{37,31}$ | $-0.0038867813800467377$ |
| $c_{39,31}$ | $-0.0013688228774160712$ |
| $c_{3\ 11,31}$ | $-5.464382649936792e-4$ |
| $c_{3\ 13,31}$ | $-2.3357829879623381e-4$ |
| $c_{51,31}$ | $-0.005448935914227867$ |
| $c_{53,31}$ | 0.0014652438473695612 |
| $c_{55,31}$ | 0.001132045537597591 |
| $c_{57,31}$ | $5.868603011952376e-4$ |
| $c_{59,31}$ | $2.8324636593608603e-4$ |
| $c_{5\ 11,31}$ | $1.4735936118090648e-4$ |
| $c_{5\ 13,31}$ | $8.029610273034155e-5$ |
| $c_{71,31}$ | $-8.718413818525627e-4$ |
| $c_{73,31}$ | $5.77797668948919e-4$ |
| $c_{75,31}$ | $5.372407346228706e-4$ |
| $c_{77,31}$ | $3.4351934525776636e-4$ |

| $No.$ | $c$ |
|---|---|
| $c_{79,11}$ | $1.9634326599968067e-4$ |
| $c_{7\ 11,31}$ | $1.1151601634043005e-4$ |
| $c_{7\ 13,31}$ | $6.541862753917567e-5$ |
| $c_{91,31}$ | $-2.718947004001723e-5$ |
| $c_{93,31}$ | $2.399361107398117e-4$ |
| $c_{95,31}$ | $2.640804401951214e-4$ |
| $c_{97,31}$ | $1.948437006398449e-4$ |
| $c_{99,31}$ | $1.2192918158470569e-4$ |
| $c_{9\ 11,31}$ | $2.624236030659881e-4$ |
| $c_{9\ 13,31}$ | $1.9902454404194082e-4$ |
| $c_{111,31}$ | $1.8242706615778748e-4$ |
| $c_{113,31}$ | $1.1542298202362265e-4$ |
| $c_{115,31}$ | $1.284686011771757e-4$ |
| $c_{117,31}$ | $1.0558505491976287e-4$ |
| $c_{119,31}$ | $7.076698604727349e-5$ |
| $c_{11\ 11,31}$ | $5.1011041454924356e-5$ |
| $c_{11\ 13,31}$ | $3.445898615473438e-5$ |
| $c_{131,31}$ | $1.921568115055954e-4$ |
| $c_{133,31}$ | $7.130571252279952e-5$ |
| $c_{135,31}$ | $6.579755168273157e-5$ |
| $c_{137,31}$ | $6.0998298687631704e-5$ |
| $c_{139,31}$ | $-1.1422610778644582e-5$ |
| $c_{1311,31}$ | $8.28522710271449e-6$ |
| $c_{1313,31}$ | $-3.9359340331396015e-7$ |

Table A.6: Calculated Fourier coefficients for mn=31 ($a = 0.5 \cdot 10^{-3} m$)

| $No.$ | $c$ |
|---|---|
| $c_{11,33}$ | 0.00523214854931386 |
| $c_{31,33}$ | −0.06656969184006789 |
| $c_{51,33}$ | −0.0067883015453799305 |
| $c_{71,33}$ | −0.0015753928978537802 |
| $c_{91,33}$ | $-5.670381024377198e-4$ |
| $c_{11\ 1,33}$ | $-2.2913313021308683e-4$ |
| $c_{13\ 1,33}$ | $-1.0735118829407634e-4$ |
| $c_{31,33}$ | −0.06666386929818931 |
| $c_{33,33}$ | 1.0418779416448622 |
| $c_{35,33}$ | 0.04467412539282639 |
| $c_{37,33}$ | 0.01237400383746014 |
| $c_{39,33}$ | 0.00439706843847553 |
| $c_{3\ 11,33}$ | 0.0017760226728215 17 |
| $c_{3\ 13,33}$ | $7.68772145437416e-4$ |
| $c_{51,33}$ | −0.0068293437727647 62 |
| $c_{53,33}$ | 0.044544493704352824 |
| $c_{55,33}$ | $-8.827935297078511e-4$ |
| $c_{57,33}$ | $-8.998662670052963e-4$ |
| $c_{59,33}$ | $-5.293558579865438e-4$ |
| $c_{5\ 11,33}$ | $-2.8853943923067303e-4$ |
| $c_{5\ 13,33}$ | $-1.6983358148758615e-4$ |
| $c_{71,33}$ | −0.0015753093063171839 |
| $c_{73,33}$ | 0.012364426768610257 |
| $c_{75,33}$ | $-8.942469858831488e-4$ |
| $c_{77,33}$ | $-7.859554088437906e-4$ |

| $No.$ | $c$ |
|---|---|
| $c_{79,33}$ | $-4.979033469804656e-4$ |
| $c_{7\ 11,33}$ | $-2.999208052662734e-4$ |
| $c_{7\ 13,33}$ | $-1.8167688459170766e-4$ |
| $c_{91,33}$ | $-5.505224438993467e-4$ |
| $c_{93,33}$ | 0.004421205417406707 |
| $c_{95,33}$ | $-5.320013937798329e-4$ |
| $c_{97,33}$ | $-5.114566558906201e-4$ |
| $c_{99,33}$ | $-3.545321223359861e-4$ |
| $c_{9\ 11,33}$ | $-7.312724534400147e-4$ |
| $c_{9\ 13,33}$ | $-6.055877322453647e-4$ |
| $c_{111,33}$ | $-2.2152568070663015e-4$ |
| $c_{113,33}$ | 0.0017589243214572628 |
| $c_{115,33}$ | $-2.8597706916151677e-4$ |
| $c_{117,33}$ | $-2.957463761403997e-4$ |
| $c_{119,33}$ | $-2.3260108224379468e-4$ |
| $c_{11\ 11,33}$ | $-1.6650352968780873e-4$ |
| $c_{11\ 13,33}$ | $-1.1487929538559836e-4$ |
| $c_{131,33}$ | $-1.0678677578335759e-4$ |
| $c_{133,33}$ | $7.623827988986329e-4$ |
| $c_{135,33}$ | $-1.7308038429235395e-4$ |
| $c_{137,33}$ | $-1.7919681349800698e-4$ |
| $c_{139,33}$ | $4.821241935536352e-5$ |
| $c_{1311,33}$ | $-2.6843810238848457e-5$ |
| $c_{1313,33}$ | $-4.931066705055315e-6$ |

Table A.7: Calculated Fourier coefficients for mn=33 ($a = 0.5 \cdot 10^{-3} m$)

# Appendix B

# Prior noise sensor prototype schematics

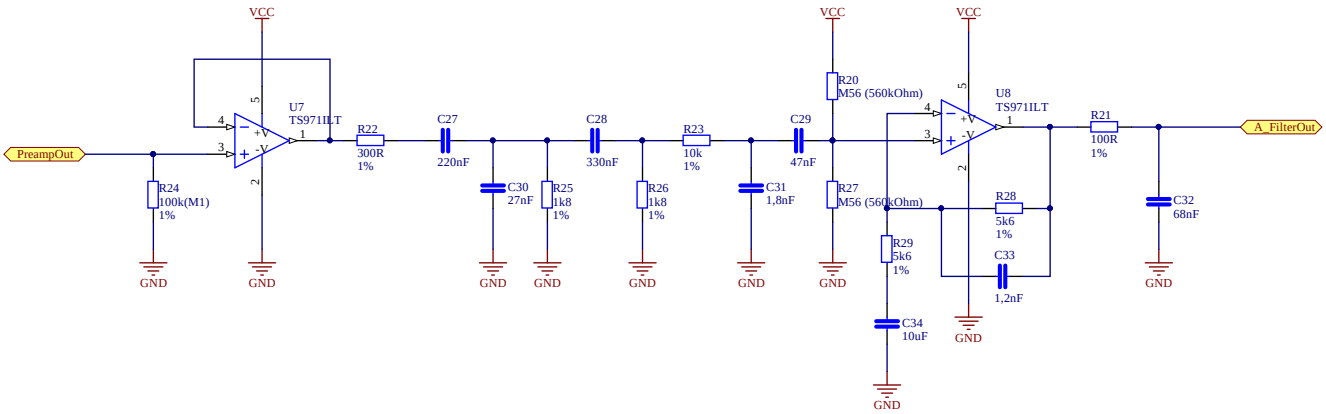


| | | |
|---|---|---|
| Title | | |
| Size: A4 | Number | Revision |
| Date: 28.11.2017 | | Sheet of |
| File: C:\Users\..\Afilter.SchDoc | | Drawn By: |

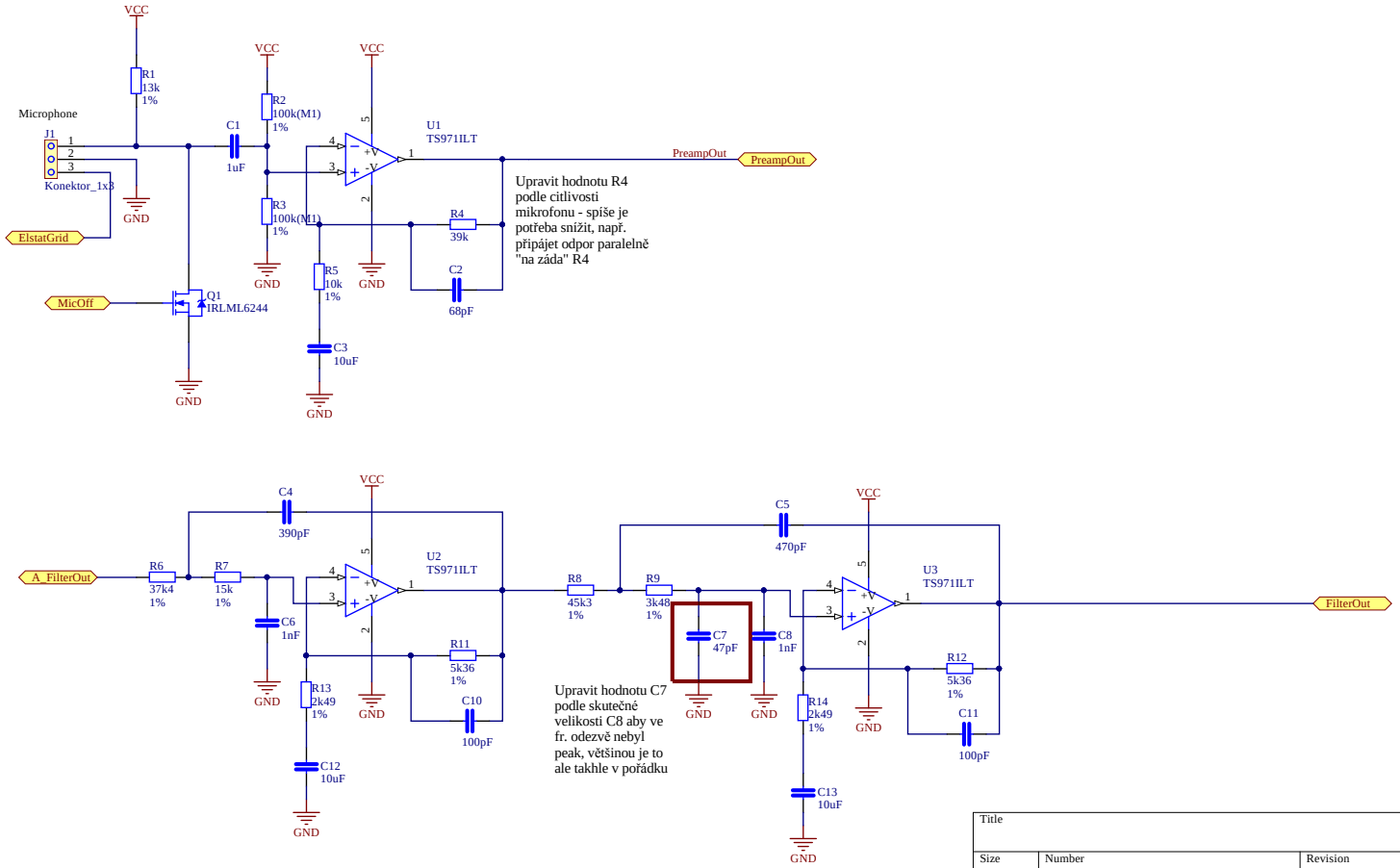


| | | |
|---|---|---|
| Title | | |
| Size: A4 | Number | Revision |
| Date: 28.11.2017 | | Sheet of |
| File: C:\Users\..\Analog_preamp_QFN_final_Drawn.SchDoc | | Drawn By: |

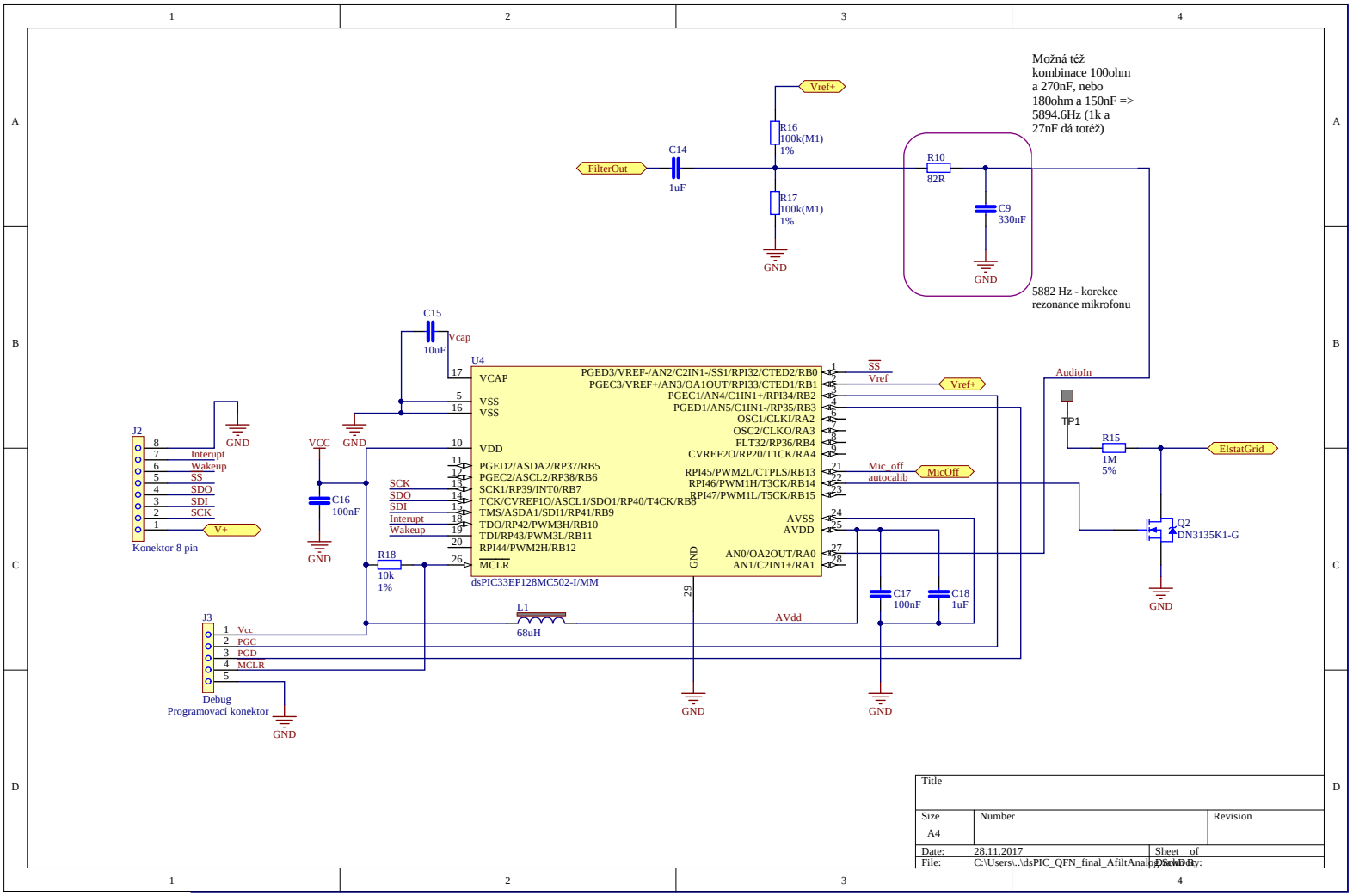


| | | |
|---|---|---|
| Title | | |
| Size: A4 | Number | Revision |
| Date: 28.11.2017 | | Sheet of |
| File: C:\Users\..\dsPIC_QFN_final_AfiltAnalog.SchDoc | | Drawn By: |

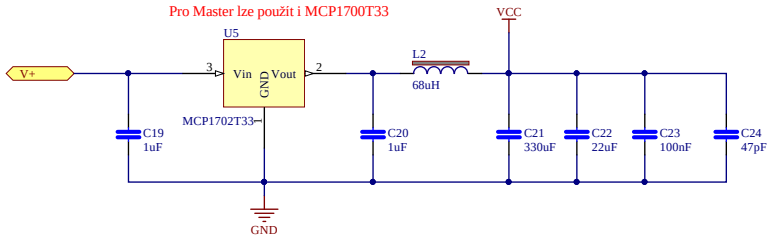


M1 FiducialR 1mm

M2 FiducialR 1mm

M3 FiducialR 1mm

M4 FiducialR 1mm

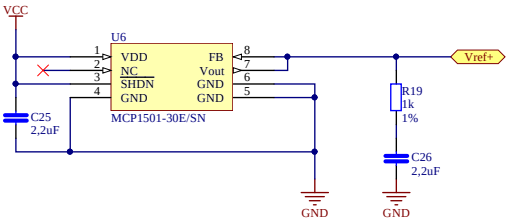


| | | |
|---|---|---|
| Title | | |
| Size: A4 | Number: | Revision: |
| Date: 28.11.2017 | | Sheet of |
| File: C:\Users\..\Power_ref_QFN_final_Afilt.SchDoc | | Drawn By: |

# Appendix C

# Present noise sensor schematics

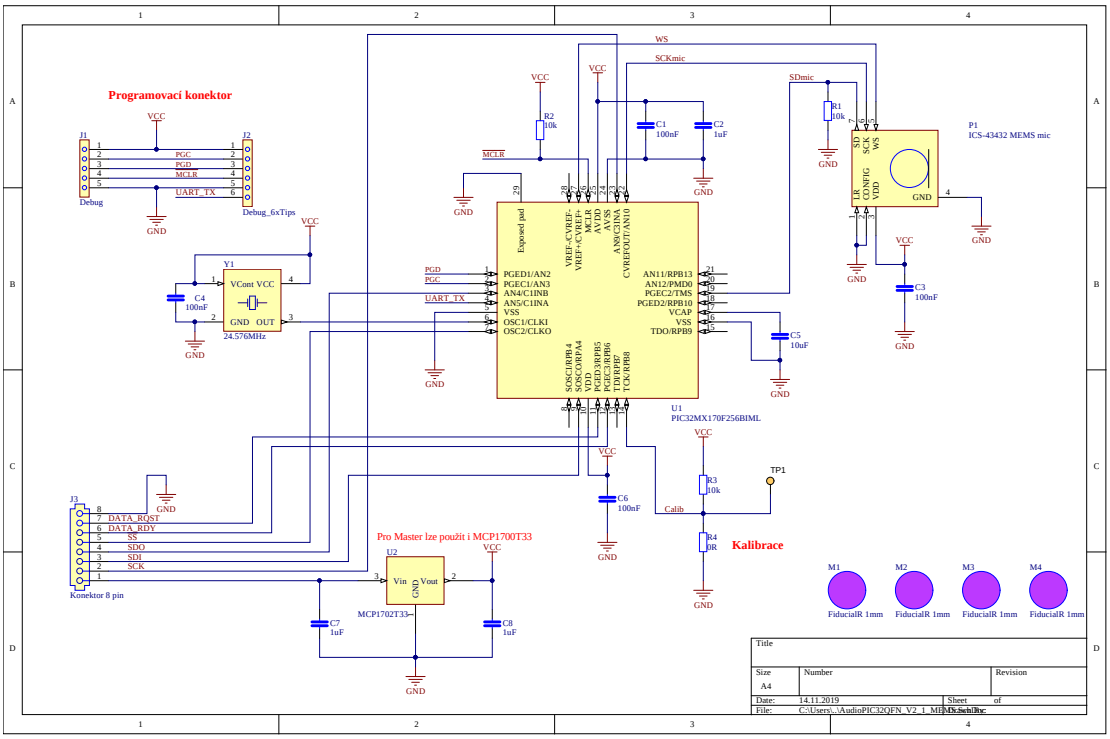


Figure C.1: Present noise sensor schematics